

Karlsruher Institut für Technologie
Fakultät für Chemie und Biowissenschaften

Dissertation

**Microstructure Analysis of (V,Al)(C,N)
Hard Coatings by X-Ray Diffraction
and X-Ray Absorption Fine Structure
Spectroscopy**

von
Mariyam Susana Dewi Darma

April 2012

Microstructure Analysis of the (V,Al)(C,N) Hard Coatings by X-Ray Diffraction and X-Ray Absorption Fine Structure Spectroscopy

Zur Erlangung des akademischen Grades eines

DOKTORS DER NATURWISSENSCHAFTEN

(Dr.rer.nat.)

Fakultät für Chemie und Biowissenschaften

Karlsruher Institut für Technologie - Universitätsbereich

genehmigte

DISSERTATION

von

Mariyam Susana Dewi Darma

aus

Bandung, Indonesien

Dekan : Prof. Dr. Martin Bastmeyer

Referent : Prof. Dr. Annie K. Powell

Korreferent : Prof. Dr. Gerd Tilo Baumbach

Tag der mündlichen Prüfung : 19 April 2012

Abstract

Hard coatings are used for many industrial applications because they increase the life time of machining tools. In this thesis, a new type of hard coatings consisting of V, Al, C and N was studied. The coatings were deposited by reactive radio frequency (rf) magnetron sputtering using a combinatorial approach, i.e. several substrates were placed below the target and coated simultaneously from a segmented target consisting of half a VC target and half an AlN target. Two substrates were used, polycrystalline cemented carbide and Si(001) substrates. On both substrates, the coatings were deposited with similar deposition parameters, but different deposition time. It was found that the chemical composition and the thickness depend on the position below the target.

X-Ray Diffraction (XRD) and X-Ray Absorption Fine Structure Spectroscopy (XAFS) were used to characterize the microstructure of the coating. All coatings have a mixed fcc V-Al-C-N phase. The lattice parameter and the interatomic distance decrease with increasing Al concentration as expected for a mixed crystal. For all coatings, the dominant texture was the laterally compressed (111) texture. The direction of the dominant texture is related to the average flux direction at sample position. Depending on the position below the target, this texture is superimposed with other textures, e.g. the (200) texture, the (220) texture and randomly oriented crystallites. For coatings on cemented carbide, biaxially aligned textures were observed, which was not found for the much thinner coatings on Si.

From the experimental results we found that not only the chemical composition, but also the microstructure vary as a function of position below the segmented target. Therefore, it cannot be distinguished if the hardness variation is due to the chemical composition variation or the microstructure. However, the crystal phase could be related to the composition because no significant influence of the microstructure is expected. The experimentally measured Al concentration is smaller than the expected maximum concentration for the mixed fcc phase. Therefore, the hardness could be further optimized by increasing the Al content.

Abstract

Hartbeschichtungen werden für viele industrielle Anwendungen verwendet, da sie die Lebensdauer z.B. von Zerspanungswerkzeugen verlängern. In dieser Arbeit wurde ein neues Hartbeschichtungsmaterial bestehend aus V, Al, C und N untersucht. Die Schichten wurden durch reaktives Hochfrequenz-Magnetronspütern hergestellt. Ein kombinatorischer Ansatz wurde realisiert, indem mehrere nebeneinander liegende Substrate simultan von einem segmentierten Target beschichtet wurden. Das Target bestand jeweils zur Hälfte aus VC und AlN. Es wurden zwei verschiedene Substrattypen (Polykristallines Hartmetall und Si(001)) unter ähnlichen Bedingungen, allerdings mit unterschiedlichen Depositionsdauer, beschichtet. Es zeigte sich, dass sich sowohl die chemische Zusammensetzung als auch die Schichtdicke mit der Probenposition verändern.

Röntgendiffraktion (XRD) und Röntgenabsorptionsspektroskopie (XAFS) wurden zur Charakterisation der Mikrostruktur der Beschichtungen angewandt. Alle Beschichtungen weisen eine gemischte kubisch-flächenzentrierte (kfz) V-Al-C-N Phase auf. Wie für einen gemischten Kristall erwartet, verringern sich der Gitterparameter und der Atomabstand mit zunehmendem Al Gehalt. Alle Schichten haben eine dominante, lateral gestauchte (111) Textur. Die Orientierung der dominanten Textur scheint mit der mittleren Flussrichtung der deponierten Atome zusammenzuhängen. Abhängig von der Probenposition unter dem Target ist die (111) Textur überlagert mit anderen Texturen, z.B. (200) Textur, (220) Textur und Kristallite ohne Vorzugsrichtung. Bei den auf Hartmetall deponierten Schichten wurden auch Texturen mit biaxialer Orientierung gefunden.

Die experimentellen Resultate zeigen, dass nicht nur die chemische Zusammensetzung, sondern auch die Mikrostruktur von der Probenposition unter dem segmentierten Target abhängt. Deshalb kann nicht unterschieden werden, ob die gemessenen Härtevariation von der chemischen Zusammensetzung oder der Mikrostruktur verursacht wird. Die Abhängigkeit der kristallinen Phase von der Konzentration konnte untersucht werden, da in diesem Fall kein signifikanter Einfluss der Mikrostruktur erwartet wird. Die experimentell gemessene Al Konzentration der gemischten kfz Phase ist geringer als die erwartete maximale Konzentration. Deshalb könnte die Härte des Materials durch einen höheren Al Anteil weiter optimiert werden.

Contents

List of Figures	XII
List of Tables	1
1 Introduction	2
2 Hard Coating Materials	5
2.1 Influence of the Chemical Bond	5
2.2 Gibbs Energy of a Binary System	7
2.3 A New and Promising Hard Coating Material: V-Al-C-N	8
2.4 Influence of the Microstructure	10
2.5 Summary	12
3 Radio Frequency (rf) Magnetron Sputter Deposition	13
3.1 rf Magnetron Sputter System	13
3.2 Sputter Deposition Processes	15
3.2.1 Interactions in the Plasma	15
3.2.2 Interactions between Plasma Species and Target	16
3.2.3 Interactions between Plasma and Substrate	18
3.3 Combinatorial Approach	19
3.3.1 Calculated Flux Distribution	20
4 Microstructure Analysis by X-Ray Scattering	23
4.1 X-Ray Scattering	23
4.1.1 Bragg's Law and Laue condition	23
4.1.2 Structure Factor of a Crystal	25
4.2 Cubic, Rhombohedral and Hexagonal Unit Cells	26
4.3 Allowed Reflections of the Rock Salt and the Wurtzite Structure	28
4.4 Peak Broadening	29
4.4.1 Influence of Size of a Fiber on Peak Broadening	29
4.4.2 Influence of Strain Distribution on Peak Broadening	30
4.4.3 Peak Broadening as a function of the Order of the Reflections	32
4.5 Fiber Texture	32
4.5.1 (111) Fiber Texture	34
4.5.2 (200) Fiber Texture	36

4.5.3	(220) Fiber Texture	38
4.6	Correction Factors of the Measured Intensity	39
4.7	X-Ray Stress Analysis	41
4.7.1	$\sin^2 \Psi$ Method	42
4.7.2	Biaxial Stress Model	43
4.7.3	Residual Stress of a Weakly Textured Coating	44
5	X-Ray Absorption Fine-Structure Spectroscopy	46
5.1	Introduction	46
5.2	XANES at the Vanadium K edge	48
5.3	Determination of the Atomic Distance	49
6	Experimental details of the X-Ray Measurement	51
6.1	Geometries and Measurement Range of the XRD Experiments	51
6.2	X-Ray Absorption Fine Structure Spectroscopy	54
6.3	X-Ray Fluorescence	54
7	Pre-Characterization of V-Al-C-N Hard Coating on Cemented Carbide and Si	56
7.1	Deposition Parameters	56
7.2	Chemical Composition and Thickness as a Function of Position	57
7.3	Fluorescence Intensity Map	58
7.4	Coating Morphology	60
8	X-Ray Diffraction Results of (V,Al)(C,N) Thin Films on Cemented Carbide	61
8.1	Analysis of the Radial Scans	61
8.1.1	Substrate Reference	61
8.1.2	Coating Reflections	62
8.1.3	Whole Pattern Fitting Method	64
8.1.4	Lattice Spacing	65
8.1.5	Peak Broadening	67
8.1.6	Main Results	69
8.2	Texture Analysis	69
8.2.1	Texture Superposition for X = -18 mm	72
8.2.2	Texture Superposition for X = -6 mm	74
8.2.3	Texture Superposition for X = 6 mm	76
8.2.4	Texture Superposition for X = 18 mm	78
8.2.5	Main Results	79
8.3	Influence of the Texture Superposition on d_{hkl}	80
9	X-Ray Diffraction Results of (V,Al)(C,N) Thin Films on Si	84

9.1	Sample Coordinate System	84
9.2	Analysis of the Radial Scans	85
9.2.1	Coating Reflections	85
9.2.2	Whole Pattern Fitting Method	87
9.2.3	Lattice Spacing	88
9.2.4	Peak Broadening	91
9.2.5	Main Results	92
9.3	Textures Analysis	93
9.3.1	Texture Superposition for X = -5 mm	96
9.3.2	Texture Superposition for X = 5 mm	98
9.3.3	Texture Superposition for X = 15 mm	99
9.3.4	Texture Superposition for X = 25 mm	101
9.3.5	Main Results	102
9.4	Influence of Texture Superposition on d_{hkl}	104
10 XAFS Result of the (V,Al)(C,N) Coatings at Vanadium K-edge		108
10.1	XANES at the Vanadium K-edge	108
10.2	Atomic Distance	110
10.3	Main Results	112
11 In-Plane Compressive Stress of the V-Al-C-N Hard Coatings		113
11.1	Distorted fcc Unit Cell	113
11.1.1	Main Results	116
11.2	Residual Stress as a Function of Position	118
11.3	Main Results	120
12 Discussion		121
12.1	Crystalline Phase of V-Al-C-N Coating	121
12.1.1	Atomic Distance as a Function of Chemical Composition	123
12.1.2	Solubility Limit of AlN in fcc-VC Structure	126
12.2	The Development of the Texture of the V-Al-C-N Coating	127
12.2.1	Development of the Texture Superposition	129
12.2.2	Development of Monoaxially and Biaxially Aligned Texture	130
12.3	The Differences between Coatings on Cemented Carbide and Coatings on Si131	131
12.4	Interplay between Chemical Composition, Microstructure and Hardness	133
13 Summary, Conclusions and Outlook		137
13.1	Summary	137
13.2	Conclusions	140
13.3	Outlook	141

Contents

14 APPENDIX A	142
References	144
List of Symbols	152
Curriculum Vitae	156

List of Figures

2.1	(a) The desired properties of hard coatings, (b) three strong chemical bonds, (c) Holleck triangle (Adapted from [10]) and (d) desired chemical bonds and crystal structure for a new hard coating material.	6
2.2	Schematic representation of ΔG as a function of concentration for fcc, hcp and amorphous phases at constant T [9].	8
2.3	(a) Interaction energy of many fcc compounds and AlN [9], (b) calculated phase diagram of VC-AlN [9] and (c) mixed unit cells of fcc and hcp V-Al-C-N.	9
2.4	Hardening mechanisms: (a) crystal orientation, (b) grain size, (c) stress and (d) orientation distribution.	10
3.1	(a) Cross section of an rf magnetron sputtering chamber, (b) electron confinement and (c) erosion track of the target.	14
3.2	(a) Schematic of interaction between ionized sputter gas and target [Adapted from [37]], (b) angular distribution [34] and (c) typical energy distribution of the sputtered atoms [38].	17
3.3	Interactions between plasma and substrate: (1) surface diffusion, (2) deposited target atom, (3) re-sputtered atom, (4) deposited sputter gas atom and (5) chemical reaction between deposited target atom and reactive sputter gas atom.	18
3.4	(a) Cross section of the target-substrate geometry, (b) incoming flux at a point P_S on substrate surface is sum of the flux from the VC and the AlN target area (courtesy of B. Krause).	19
3.5	(a) Solid line: the calculated Al/(Al+V) ratio and thickness, points: measured data, (b) cross section of flux distribution at $Y = 0$ mm and (c) top view of flux distribution towards the substrate (courtesy of B. Krause).	22
4.1	Schematic illustration of the scattering from a crystal lattice in (a) real space and (b) reciprocal space (adapted from [49]).	24
4.2	(a) cubic, (b) rhombohedral and (c) hexagonal unit cells.	27
4.3	Crystal structure of (a) rock salt and (b) wurtzite structure.	28
4.4	(a) Schematic of a fiber texture, (b) cylindrical fiber where q_z is parallel to the cylinder axis and the $q_{ }$ is perpendicular to the cylinder axis, (c) normalized $ F_{shape} ^2$ for two cases.	30

List of Figures

4.5	Schematic of polycrystalline materials and their Bragg reflection for the case (a) without strain, (b) homogeneously strained, and (c) inhomogeneously strained.	31
4.6	Schematic of the crystal orientation of (a) a single crystal (b) a powder and (c) a fiber texture.	33
4.7	(a) A cubic unit cell with [111] orientation parallel to the surface normal, (b) orientation of different lattice planes relative to the (111) plane in polar coordinates, (c) schematic of (111), (200) and (220) pole figures for different types of (111) fiber textures, and (d) expected peak position for the (111) texture as a function of Ψ	35
4.8	(a) A cubic unit cell with [200] orientation parallel to the surface normal, (b) orientation of different lattice planes relative to the (200) plane in polar coordinates, (c) schematic of the (200), (111) and (220) pole figures for different types of (200) fiber textures, and (d) expected peak positions for the (200) texture as a function of Ψ	37
4.9	(a) A cubic unit cell with [220] orientation parallel to the surface normal, (b) orientation of different lattice planes relative to the (220) plane in polar coordinates, (c) schematic of the (220), (111) and (200) pole figures for different types of the (220) fiber textures, and (d) expected peak position for the (220) texture as a function of Ψ	39
4.10	(a) X-Ray beam illuminates and penetrates the sample schematically and (b) typical correction for the illuminated scattering volume correction of pole figure geometry as a function of tilting angle Ψ	40
4.11	(a) Stress tensor, (b) illustration of the $\sin^2 \Psi$ method, (c) strain map, and (d) schematic of the $\langle a \rangle$ vs $\sin^2 \Psi$ plot.	44
5.1	(a) Schematic of XAFS, (b) XANES and EXAFS regions of the XAFS spectra.	47
5.2	XANES spectra for (a) VC and (b) V_2O_5 as adapted from [58].	49
5.3	EXAFS spectrum as a function of (a) wavevector k and (b) atomic distance R	50
6.1	(a) Experimental station of the PDiff beamline. Sample and detector movement for (b) the radial scan, (d) the strain map, (e) the pole figure. Reciprocal space for (c) the radial scan, (e) the strain map, and (f) the pole figure.	52
6.2	The pre-determined scattering angle θ for a sample on cemented carbide at $X = -6$ mm of (a) (111) and (b) (200) reflections.	53
6.3	(a) Experimental station of XAS beamline, (b) sample rotation stage, and (c) schematic of the fluorescence geometry.	55

List of Figures

7.1	Bottom view projection of the substrates on the target for: (a) the coatings on cemented carbide and (b) on Si.	57
7.2	(a) Chemical composition and thickness, and (b) (V+Al)/(C+N) ratio of the coatings on cemented carbide as a function of X.	58
7.3	Fluorescence intensity map of the coatings on: (a) cemented carbide and (b) Si.	59
7.4	(a) and (b): SEM images, (c) and (d): AFM images of coatings on cemented carbide at selected positions, and (e) the roughness measured by AFM.	60
8.1	Diffraction profile of cemented carbide.	62
8.2	Radial scans measured at selected positions.	63
8.3	Radial scan for X = 30 mm and calculated peak position of a cubic unit cell with a = 4.2 Å.	64
8.4	The Whole Pattern Fitting Method (WPFM) for X = -6 mm.	65
8.5	Measured and calculated lattice spacing d_{hkl} as a function of X shown for different reflections.	66
8.6	The FWHM as a function of reflections and position.	68
8.7	The ratio of FWHM ₂₂₂ and FWHM ₁₁₁ as a function of position.	69
8.8	Strain maps for coatings in the range of -24 mm < X < 24 mm.	70
8.9	(111) and (200) pole figures of the coatings on cemented carbide.	71
8.10	(a) (111) and (b) (200) pole figures, (c) (220) strain map, (d) to (f): schematic (111), (200) and (220) pole figures for a superposition of the (111) texture, the (220) texture, and the powder-like crystallites, (g) to (i): line scans and fittings of the (111), the (200) and the (220) reflections.	73
8.11	Measured (a) (111) pole figure, (b) enhance (200) pole figure and (c) enhanced (220) strain map. Schematic (d) (111), (e) (200) and (f) (220) pole figures for a superposition of (111), (200) and (220) textures. Line scans of (g) the (111), (h) the (200) and (i) the (220) reflections are fitted by calculating the peak positions for cubic symmetry.	75
8.12	(a) (111) and (b) (200) pole figures, (c) (220) strain map, (d) to (f): schematic (111), (200) and (220) pole figures for a superposition of the isotropic and anisotropic (111) texture, (g) to (i): line scan and fitting of the (111), the (200) and the (220) reflections.	77
8.13	(a) (111) and (b) (200) pole figures, (c) (220) strain map, (d) to (f): schematic (111), (200) and (220) pole figures for a superposition of the isotropic and anisotropic (111) texture, (g) to (i): line scan and fitting of the (111), the (200) and the (220) reflections.	78
8.14	(a) Qualitative summary of the crystallographic orientation of the coatings as a function of position below the target (X), (b) fitted average orientation Ψ_{hkl} and (c) fitted orientation distribution σ_{hkl} of the textures.	80

List of Figures

8.15	Columns: d_{hkl} vs Ψ plot for the (111), the (200) and the (220) reflections. Rows: d_{hkl} vs Ψ plot at different X.	82
8.16	The texture superposition of (a) the (111), (b) the (200) and (c) the (220) reflection for the sample at X = -6 mm, and (d) to (f): their corresponding d_{hkl} vs Ψ plots.	83
9.1	(a). Projection of the sample positions on the target, (b) fluorescence intensity map of the coatings on Si and the corresponding coordinate system.	84
9.2	The diffraction profiles of the samples deposited on Si(001) substrates.	86
9.3	The Whole Pattern Fitting Method (WPFM) for X = -5 mm.	88
9.4	(a) Measured lattice spacings as a function of position for coatings on the first and second row coatings on Si. The measured and the calculated lattice spacing for (b) first row and (c) second row coatings on Si.	89
9.5	Measured and calculated lattice spacings of all reflections as a function of position for (a) coatings on cemented carbide and (b) second row coatings on Si.	90
9.6	The FWHM as a function of coating reflections for different X at (a) the first row and (b) the second row coatings on Si. (c) The $FWHM_{222}/FWHM_{111}$ ratio.	92
9.7	Strain map of coatings on Si as a function of position below the target.	94
9.8	(111) Pole figures of coatings on Si as a function of position below the target.	95
9.9	(200) Pole figures of coatings on Si as a function of position below the target.	96
9.10	Measured (a) (111) pole figure, (b) enhanced (200) pole figure and (c) enhanced (220) strain map. Schematic (d) (111), (e) (200) and (f) (220) pole figures for a superposition of (111), (200) and (220) textures. The (g) (111), (h) the (200), and (i) the (220) line scans are fitted by calculated peak positions assuming cubic symmetry and texture superposition.	97
9.11	Measured (a) (111) pole figure, (b) (200) pole figure and (c) enhanced (220) strain map for X = 5 mm. Schematic (d) (111), (e) (200) and (f) (220) pole figures for a superposition of the (111), the (200) and the (220) textures. The (g) (111), (h) the (200), and (i) the (220) line scans are fitted by calculated peak positions assuming cubic symmetry and texture superposition.	99
9.12	Measured (a) (111) pole figure, (b) (200) pole figure and (c) enhanced (220) strain map for X = 15 mm. Schematic (d) (111), (e) (200) and (f) (220) pole figures for a superposition of the (111) and the (220) textures. The (g) (111), (h) the (200), and (i) the (220) line scans are fitted by calculated peak positions assuming cubic symmetry and texture superposition.	100

List of Figures

9.13	Measured (a) (111) and (b) (200) pole figures and (c) enhanced (220) strain map for X = 25 mm. Schematic (d) (111), (e) (200) and (f) (220) pole figures for a superposition of the (111) and the (220) textures. The (g) (111), (h) the (200), and (i) the (220) line scans are fitted by calculated peak positions assuming cubic symmetry and texture superposition. . . .	102
9.14	(a) Qualitative summary of crystallographic orientation of the coatings as a function of position below the target X, fitted (b) average orientation Ψ_{hkl} and (c) distribution σ_{hkl} of each type of texture.	104
9.15	d_{hkl} vs Ψ plot for the (111), the (200) and the (220) rings at selected coating positions.	105
9.16	Texture superposition of (a) the (111), (b) the (200) and (c) the (220) reflection for sample at X = 15 mm. (d) to (f): Corresponding d_{hkl} vs Ψ plots.	106
10.1	XANES spectra of (a) VC and VN coatings, (b) VC coating and VC target, (c) V-Al-C-N coatings on cemented carbide, and (d) two V-Al-C-N coatings on Si(001).	109
10.2	(a) Fourier transformation of EXAFS spectra for coatings on cemented carbide (spectra are presented without phase shift correction), (b) calculated EXAFS amplitude assuming fcc (V,Al)(C,N) (c) a mixed (V,Al)(C,N) in fcc structure, and (d) atomic distance of V-(V,Al).	111
11.1	(a) Strain map for coatings on cemented carbide at X = 6 mm, (b) schematic (111) cubic unit cell, and (c) schematic distorted (111) oriented cubic unit cell.	114
11.2	Fitting of the coating reflections on cemented carbide at X = 18 mm assuming (a) to (c): a cubic unit cell and (d) to (f): a distorted cubic unit cell.	115
11.3	Fitting of the coating reflections on Si at X = 15 mm assuming (a) to (c): a cubic unit cell, and (d) to (f): a distorted cubic unit cell.	116
11.4	Projection of the substrate on the target and coordinate system of the coatings on (a) cemented carbide and (b) Si(001). Variation of the (c) lattice parameter, (d) distorting angle α and (e) volume of the unit cell of coatings on cemented carbide and on Si as a function of position. A red dashed line in (d) at $\alpha = 90^\circ$ corresponds to the α of a perfect cubic unit cell.	117
11.5	$\langle a \rangle$ versus $\sin^2\Psi$ plot of coating on cemented carbide and on Si(001). . .	118
11.6	(a) Measured reduced Young modulus, and (b) calculated residual stress.	120

List of Figures

12.1	(a) A (111) oriented cubic unit cell of a mixed fcc-(V,Al)(C,N), (b) atomic distance of V-(C,N) as a function of position and (c) the unit cell volume of the (111) texture as a function of the Al/(Al+V) ratio.	125
12.2	The schematic of expected crystalline phases as a function of Al/(Al+V) ratio.	127
12.3	The detailed texture analysis requires (a) the (111) pole figure, (b) the enhanced (200) pole figure and (c) the strain map.	128
12.4	The microstructure of the coatings on cemented carbide and on Si is different in the following aspects: (a) in-plane orientation; (b) texture superposition and (c) strain behavior.	132
12.5	(a) Hardness, (b) Al/(Al+V) percentage, (c) residual stress (d) $FWHM_{222}/FWHM_{111}$ ratio, (e) the (111) pole figure and (f) orientation and distribution of (111) texture as a function of position.	135
12.6	Green: hardness of our coatings, in red: hardness of other hard materials [11, 12, 32, 87, 93, 94, 95].	136
13.1	(a) Target-substrate geometry, (b) chemical composition and thickness as a function of position. All coatings have (c) a mixed phase rock salt structure and (d) the dominant (111) texture. However, (e) the Ψ_{111} , (f) the (200) pole figures, (g) the Ψ_{hkl} of the coexisting textures, (h) the volume unit cell, (i) the atomic distance, (j) the residual stress and (k) the hardness vary as a function of position.	139

List of Tables

3.1	Plasma Processes.	15
4.1	Fitting parameters for the atomic scattering factor calculation of V, Al, C and N [52].	26
4.2	Angle between plane $\Delta\Psi$ [deg].	36
6.1	Measurement range of the radial scan, strain map and pole figure.	54
7.1	Deposition parameters of the coatings on cemented carbide and on Si.	56
14.1	Atomic position of rock salt structure crystal such as VC	142

1 Introduction

A machining tool is a device that is used in the machining processes e.g. cutting, milling, grinding, and drilling. They are used in many industrial areas such as automotive, medical equipment, and military industry. Following the development of the tool devices, the hard coating plays an important role for enhancing the tool lifetime and maintaining their productivity. Currently more than 40% cutting tools are coated by the wear resistant coatings. The superhard coatings for high speed dry machining tool allows the industry to save high costs for recycling the currently used hazardous coolants. In Germany these costs are in the order of billion US\$ per year [1].

One of the deposition technique used for hard coatings is sputter deposition. This technique is widely used for scientific, small scale production in the laboratory as well as for mass scale production in the industry. Some of the interesting features of the sputter deposition are: it can be used to deposit materials for many applications such as LiCoO for solid state lithium ion battery, TiAlN for hard coating, ZnO for transparent conducting oxide (TCO) [2] to [5], it might be used to tailor the crystal properties of the coatings from amorphous to epitaxial growth, it has a faster deposition rate compared to e.g. Molecular Beam Epitaxy, and it is a cheap technique.

The hard coatings are used in very challenging application conditions such as high temperature, high load and high cutting rate [6]. Therefore for application purpose, the important features of the hard coatings are: high hardness, good toughness, high thermal stability, good adhesion and a low friction coefficient.

Materials for hard coatings are selected based on the chemical bond as well as the crystal structure. Combining the knowledge about the chemical bond and thermodynamic calculations, a new hard material consisting of Vanadium, Aluminum, Carbon and Nitrogen is expected to have better mechanical properties compared to commercially used hard materials e.g. TiC, TiN, TiAlN or TiAlCN [7].

The aim of the studies is to optimize the properties of the new V-Al-C-N hard coating. In order to optimize the toughness and the hardness properties, the coatings must have fcc structure and high concentration of AlN. This is a challenging task because the thermodynamically stable phase of AlN is hexagonal close packed (hcp). One solution is to deposit a metastable phase of mixed fcc V-Al-C-N where the AlN concentration in the

coating must be below the solubility limit of AlN in the fcc-VC structure.

Besides the chemical bond and the crystal phase, the hardness of the coatings is also controlled by their microstructure e.g. residual stress, crystal orientation, texture superposition as well as grain size.

The scientific questions which are addressed in this work are:

- A combinatorial approach is applied to deposit V-Al-C-N, i.e. where several substrates are placed below the target and coated simultaneously. A segmented target consisting of half a VC target and half an AlN target is used. The interest is to investigate which compositional range that can be achieved by using the segmented target.
- The crystal phase depends on the chemical composition. Within the composition range of the Al, N in the coating, the scientific interest is the determination of the crystal phase of the coatings.
- Besides the chemical composition and thickness variation, the microstructure of the coating is expected to vary as a function of the position below the target. It is challenging to analyze the microstructure variation of the coating.
- The next step is to study the relation of the deposition geometry (i.e. the position below the target) and the microstructure.
- The aim of the studies is to optimized the properties of the new V-Al-C-N. After investigation of the chemical composition, the microstructure and the hardness of the coatings, what are the possible solutions to increase the properties of the coating.

The microstructure is investigated by combining the complementary methods X-Ray Diffraction (XRD) and X-Ray Absorption Fine Structure Spectroscopy (XAFS). XRD is a probe to investigate the long-range ordering of the crystal structure while XAFS is a probe used to investigate the local environment of the absorbing atom e.g. the type of the nearest neighbor atom, the interatomic distance and the coordination number of the absorbing atom. Here, XRD is used to analyze the crystalline phase, the lattice parameter, the texture and the strain of the coating. All experiments were performed

at the synchrotron facility Angströmquelle Karlsruhe (ANKA): the XRD measurement were performed at the PDiff beamline while the XAFS spectra were measured at the XAS beamline. A test experiment using an XRD laboratory source was performed at the Leibniz Institut für Innovative Micro Electron, Frankfurt Oder.

Other methods which are used to characterize the coatings are: Electron Probe Micro Analyzer (EPMA) for chemical composition determination, calo tester for measuring the thickness, Scanning Electron Microscopy (SEM) for imaging the cross section of the coating, Atomic Force Microscopy (AFM) for imaging the surface morphology and nanointentation for hardness determination. The measurements were performed by our research collaboration partner, the Institut für Angewandte Materialien - Angewandte Werkstoffphysik (IAM-AWP) at Karlsruher Institut für Technologie (KIT), Germany.

The organization of the thesis is as follows. The scientific motivation to develop a new hard coating consisting of V,Al,C,N is described in detail in section 2. The theory of the sputter deposition technique is summarized in chapter 3. The theoretical description of the XRD and XAFS can be found in chapter 4 and chapter 5. The experimental details are shown in chapter 6. The sample description, the chemical composition and the coating morphology are described in chapter 7. The experimental results are reported in chapter 8 to 11. The discussion of the results is given in chapter 12. Chapter 13 contains the summary and some ideas how to continue the research project.

2 Hard Coating Materials

Hard coating materials are used as protection layers to enhance the lifetime of various devices such as machining tools. The coatings are classified as super hard if their Vickers Hardness H_v exceed 40 GPa [8].

In this chapter we describe the desired properties for hard materials (section 2.1). The promising candidate was then selected based on the chemical bond of the material and thermodynamic studies of many material systems (see section 2.2 and 2.3).

The mechanical properties of the hard coating are also influenced by the microstructure as described in section 2.4.

2.1 Influence of the Chemical Bond

The desired mechanical properties of the hard coating are summarized in Fig. 2.1 (a) : low friction coefficient, high hardness, good toughness and good adhesion to the metal substrate. These properties are influenced by the chemical bond of the coating material.

Depending on how the valence electrons are distributed, the strong chemical bonds are classified into covalent, ionic and metallic bonds as shown in Fig. 2.4 (b).

In the covalent bond, the valence electrons are shared between typically two atoms. This bond has a high strength and stiffness. A covalent hard material has typically hexagonal closed packed (hcp) structure [9] which has 6 slip systems.

The ionic bond is formed between a cation and an anion. The strength of the ionic bond increases with the electronegativity difference between the two ions. Ionic solids typically have the highest chemical stability, moderate strength and are extremely brittle.

The valence electrons of a material with metallic bond are delocalized forming an electron cloud where the electrons may move without disrupting the bond interactions. The metallic solids are therefore ductile, have a low melting point, low strength but are conductive. The typical thermodynamically stable structure of metallic hard materials is fcc which has 24 slip systems.

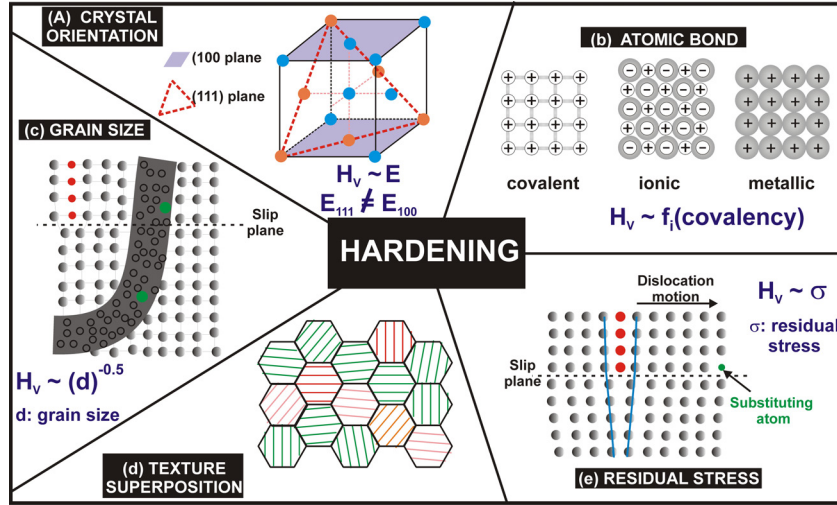


Figure 2.1: (a) The desired properties of hard coatings, (b) three strong chemical bonds, (c) Holleck triangle (Adapted from [10]) and (d) desired chemical bonds and crystal structure for a new hard coating material.

According to their chemical bonds, the hard coating materials can be divided into three groups, which are covalent, ionic, and metallic. The graphic representation of the bonding type is known as a Holleck triangle as given in Fig. 2.1 (c). Examples of typical covalent, ionic and metallic hard materials are listed in this figure.

The desired properties listed in Fig. 2.1 (a) can only be fulfilled by combining the different types of hard materials and crystal phases as summarized in Fig. 2.1 (d): (1) The hardness increases with increasing covalency [11, 12, 13, 14]; (2) compared to the covalent and ionic hard materials, the metallic hard material has a better adhesion properties on the metal substrate (typically e.g. steel and cemented carbide); (3) The toughness increases with the number of slip system. The fcc structure has more slip systems than hcp structure, therefore fcc crystal is expected to have a better toughness than hcp structure and (4) some materials such as amorphous carbon has a self lubricant effect which might decrease the friction coefficient [5].

Summing up of all parameters, we found that the combination of high hardness, good toughness and good adhesion is expected for a mixed crystal consisting of covalent and metallic hard materials in fcc phase. As it can be seen from the Holleck triangle in Fig. 2.1 (c), there are many candidates which might have all properties listed in Fig. 2.1 (a), e.g. combination of AlN (covalent hard material) and VC, TiC or ZrC (metallic hard materials). In order to select the promising candidate amongst many possible combina-

tions, S. Ulrich et al. at IAM-AWP performed thermodynamic studies on these material systems [9].

2.2 Gibbs Energy of a Binary System

Figure 2.2 shows schematically the typical Gibbs energy as a function of concentration for fcc, hexagonal and amorphous structure at constant temperature. $c_{fcc,min}$ and $c_{hex,min}$ are the concentrations at minimum ΔG_{fcc} and ΔG_{hex} respectively (hex refers to the hexagonal phase). The thermodynamically stable phase is determined by the lowest total Gibbs free energy ΔG [9]:

$$\Delta G = \sum_i n_i \cdot \Delta G_i + \epsilon \cdot c \cdot (1 - c) - RT(c \cdot \ln(c) + (1 - c) \cdot \ln(1 - c)) \quad (2.1)$$

where ΔG_i is the Gibbs free energy of the phases i as a function of concentration and n_i is the fraction of the phase i . c is the mol percentage of the metallic hard material and $(1 - c)$ is the mol percentage of the covalent material, T is the temperature and R is the ideal gas constant.

The second term of Eq. 2.1 contains the dependence of the free energy on the interaction energy ϵ . ϵ is proportional to the difference between the lattice constant of the metallic material and the theoretical lattice constant of the covalent material, assuming that the covalent hard material is cubic.

In the thermodynamically stable regime, a mixed crystal in fcc structure is expected for low concentration of covalent hard materials up to the transition concentration $c_{tr,fcc}$. From the transition concentration $c_{tr,hex}$ up to the pure covalent hard material, a mixed crystal in hexagonal close packed (hcp) structure is expected. Between these two transition concentrations, a mixture of both fcc and hcp phases are expected.

In order to enhance the hardness, the concentration of the covalent hard material should be as large as possible, i.e. a high solubility limit of the covalent hard material in the fcc lattice is desired. This is not possible in the thermodynamically stable regime. One solution is the formation of a metastable phase, e.g. by applying a high quenching rate during deposition. In the metastable phase, a mixed fcc phase is formed in a larger AlN concentration range up to $c_{tr,ms}$. Above critical concentration $c_{tr,ms}$, a mixed hcp phase is expected. The solubility limit of the covalent hard material in the fcc lattice, $c_{tr,ms}$, increases with decreasing ϵ .

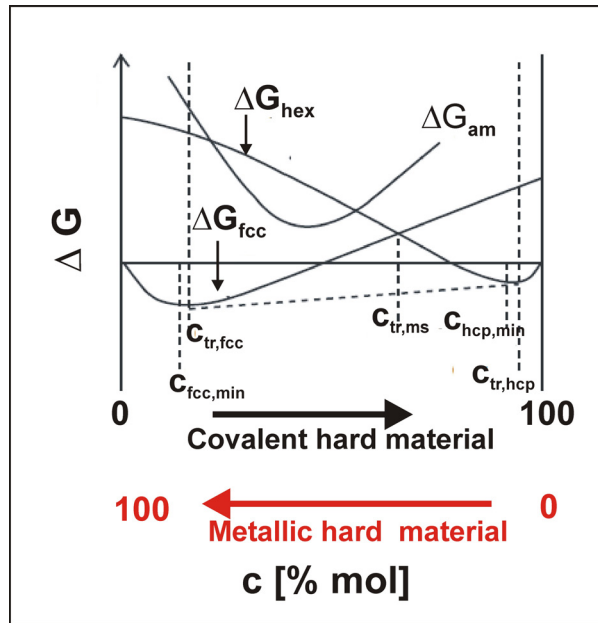


Figure 2.2: Schematic representation of ΔG as a function of concentration for fcc, hcp and amorphous phases at constant T [9].

In the following, we describe how the promising candidate for hard coating applications is selected.

2.3 A New and Promising Hard Coating Material: V-Al-C-N

One of the commercially used covalent hard materials is AlN. In order to search for the material system which has the highest solubility limit of AlN in the fcc structure, the ϵ values of quasi binary systems containing AlN and various metallic hard materials are calculated. The result is presented in Fig. 2.3 (a).

The highest AlN solubility (i.e. the lowest ϵ) is found for the VN-AlN combination, hence this material is expected to have the highest hardness (due to AlN), good toughness (related to fcc) and good adhesion to the metal substrate (due to VN). However, the low friction coefficient is also one of our desired properties. In order to decrease the friction coefficient, we need carbon content in our material system. Therefore, we decide to optimize the properties of VC-AlN instead of VN-AlN or CrN-AlN. Furthermore, at typical operating temperature of a tool around 500 - 700°, Vanadium Oxide might be

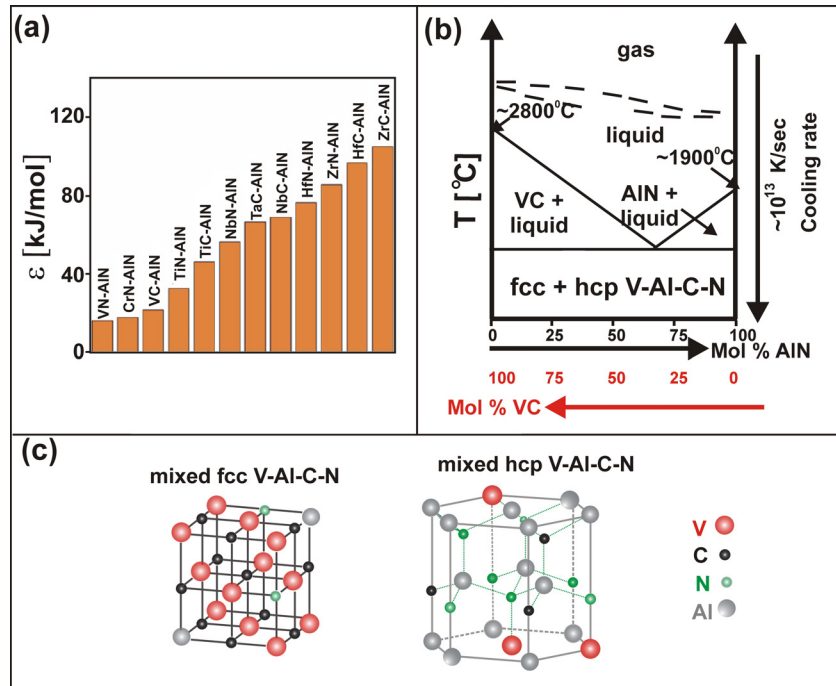


Figure 2.3: (a) Interaction energy of many fcc compounds and AlN [9], (b) calculated phase diagram of VC-AlN [9] and (c) mixed unit cells of fcc and hcp V-Al-C-N.

formed. This oxide has also a lubricating effect, therefore it expected to reduce the friction coefficient [9, 15].

The phase diagram of the VC-AlN system is calculated in order to predict the formation of the thermodynamically stable phase. This calculation was performed by S. Ulrich et al. at IAM-AWP, Karlsruher Institut für Technologie [9]. The result is presented in Fig. 2.3 (b).

At very low concentration of covalent hard material, the expected thermodynamically stable phase is a mixed crystal of fcc V-Al-C-N, while at very high concentration of covalent hard material, the expected phase is hcp V-Al-C-N. The expected phases at moderate concentration are a mixture of fcc and hcp V-Al-C-N. Figure 2.3 (c) presents schematically those phases.

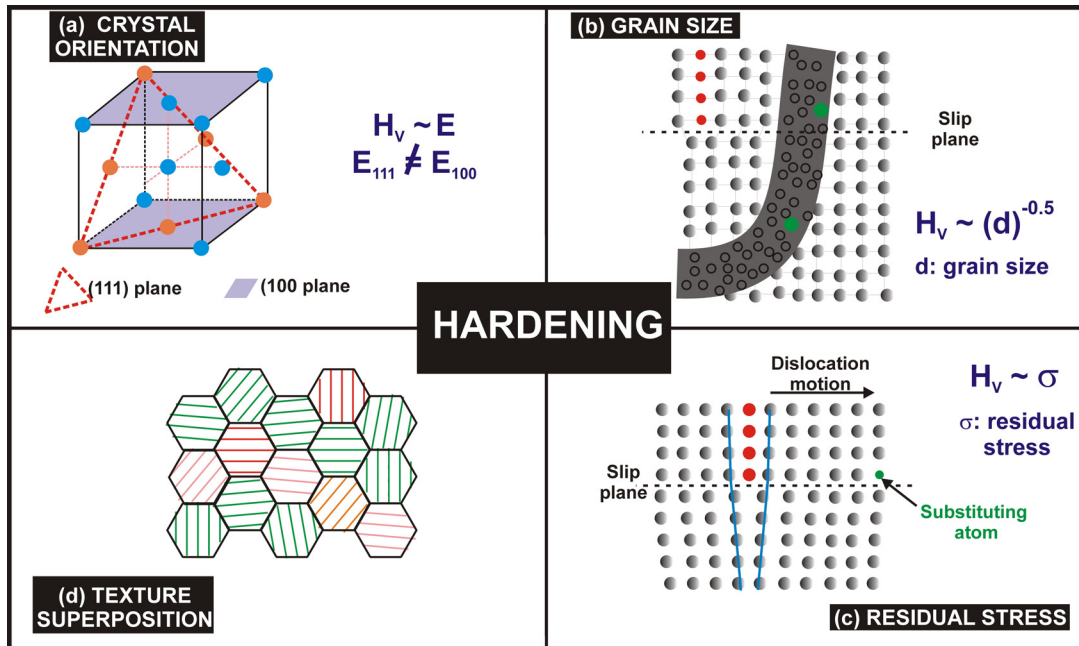


Figure 2.4: Hardening mechanisms: (a) crystal orientation, (b) grain size, (c) stress and (d) orientation distribution.

2.4 Influence of the Microstructure

Mechanical properties such as hardness and toughness are related to the material response when the stress is applied. Hardness is a measure of the resistance against plastic deformation when a force is applied while toughness is the ability of a material to deform plastically without fracture.

Plastic deformation is created through the dislocation and grain boundary motions (for detailed mechanisms see e.g. references [16, 17]). Therefore, the mechanical properties of the hard coating are not only influenced by the chemical composition, but also by the microstructure. Hence the aim of tailoring the microstructure of hard coatings (e.g. their crystalline phase, crystal size, crystal orientation or residual stress) is to create obstacles to hinder the dislocation movement [18] to [25]. An example for this is the synthetic polycrystalline diamond which has a better hardness than a single crystal of natural diamond [26].

Figure 2.4 presents schematically different aspects of the microstructure which might influence the hardness. In the following we describe the hardening mechanisms which are related to those aspects.

One parameter describing the mechanical properties is the elastic modulus E which measures the stiffness of the material. Plastic deformation is due to the dislocation activity where the energy of the dislocation activity is proportional to the shear modulus. Plastic deformation is more difficult at high E , i.e. at high covalent interatomic binding energy, short bond distance and high coordination number [27]. The hardness is proportional to the elastic modulus E , i.e. $H_v \sim E$. For a large number of different superhard nanocomposites, the proportional constant is in the range of 3.7 to 9 [27]. Since E varies as a function of crystal orientation, e.g. $E_{111} \neq E_{200}$, the hardness also varies as a function of the crystal orientation. It is reported that a (200) textured TiN/CrN superlattice exhibits higher hardness than the (111) texture of the same superlattice [22].

The gray area in Fig. 2.4 (b) is the grain boundary (GB) which separates two neighboring grains. A grain boundary has a different structure (typically amorphous) than the neighboring grains. Therefore, it hinders the dislocation motion from one grain to another grain [28]. The amount of grain boundaries increases with decreasing grain size.

The yield stress, i.e. the stress at which a material begins to deform plastically, increases with decreasing grain size. The relation between yield stress and grain size is known as Hall-Petch relationship and given in [28]:

$$\sigma_y = \sigma_0 + \frac{k_y}{\sqrt{d}} \quad (2.2)$$

where σ_y is the yield stress, σ_0 is the stress required for an individual dislocations motion, k_y is a strengthening constant and d is the grain size. The hardness itself is proportional to the yield stress. It is reported that the Vickers hardness H_v is approximately three times σ_y [29, 30].

The grain boundary hardening is only observed above a critical grain size, $d \approx 10$ nm. Below this size, the number of dislocations is nearly zero and thus instead of dislocation motion, the plastic deformation mechanism is governed by grain boundary sliding.

The crystal imperfections formed during growth such as dislocations, grain boundaries or substituting atoms create a residual stress field. The residual stress of hard coatings deposited by magnetron sputtering can reach 10 GPa [15]. Depending on the interaction of the stress centers, the residual stress might increase the hardness by hindering the dislocation motion. An examples of the interaction of two stress centers located above the glide plane is schematically given in Fig. 2.4 (c), i.e. a dislocation line and a solute atom (green sphere). The dislocation line creates a local compressive stress field while the solute atom which has smaller size than the regular atoms decrease the volume locally [28]. If the edge dislocation approaches the substituting atom (see the arrow), the

compressive strain is relieved and the edge dislocation is attracted to the solute atom. However, it is also known that large residual stress might lead to the severe problems e.g. substrate-film cracking at large tensile stress or the film decohesion by buckling in case of large compressive stress.

Another factor which influences the hardness is texture coexistence. Figure 2.4 (d) shows schematically a polycrystal with texture superposition. It is reported that the superposition of the (200) and the (220) texture in TiFeN coating leads to a higher hardness than hardness of a coating with one type of texture only [19].

The hardness is also influenced by the crystal phase. It is reported that the formation of a hexagonal AlN phase through spinodal decomposition of the supersaturated $\text{Ti}_{1-x}\text{Al}_x\text{N}$ decreases the hardness [31]. Other reports on the influence of crystal phase on the hardness can be found in [18, 19, 32].

The microstructure change, e.g. stress relaxation or decreasing number of dislocations are often observed at operating temperature of a tool in such a way that it might decrease the room-temperature hardness. Therefore, the research is focused on searching a new material which (1) has high intrinsic hardness (i.e. hardness which is related to the chemical bond) and (2) shows high thermal stability at elevated temperature, e.g. by depositing the coating with low residual stress $\sigma_{\parallel} < 0$.

2.5 Summary

The desired properties of the hard coating were described in this chapter. From our understanding about the chemical bond of the typical hard materials, and supported by the thermodynamic calculation of many material systems, we conclude that V-Al-C-N is a promising candidate for a new hard material. This material system is expected to combine a high hardness, a good adhesion to metal substrate and a low friction coefficient. For better toughness, we would like to have a fcc mixed phase of V-Al-C-N.

We also describe that the mechanical properties are not only influenced by the chemical composition, but also the microstructure e.g. crystalline phase, grain size, residual stress and texture. For this reason, the microstructure (as described in section 2.4) of the new V-Al-C-N hard coating is investigated by x-ray diffraction and x-ray absorption fine structure spectroscopy. The results are shown in chapter 8 to 11.

3 Radio Frequency (rf) Magnetron Sputter Deposition

One of the techniques to deposit hard coatings is the sputter deposition. Sputtering is a process where atoms are ejected from a solid surface (called target) due to the bombardment by energetic particles. The target atoms are sputtered if the energy transfer during bombardment is higher than the surface binding energy. The sputtered atoms are then deposited on the substrate. For a detailed description of the mechanism of sputter deposition, we propose the references [33, 34, 35] to the readers.

The new hard material system which we would like to study is V-Al-C-N (the reason is given in chapter 2). We deposit this material using the reactive radio frequency (rf) magnetron sputter technique. In this chapter, the rf magnetron sputter system and the sputter deposition process are described briefly in section 3.1 and 3.2. The calculated flux distribution of our V-Al-C-N deposition is described in section 3.3.

3.1 rf Magnetron Sputter System

The schematic cross section of the rf magnetron sputtering system which we used to deposit our samples is presented in Fig. 3.1 (a). The main components of the sputter system are briefly described as follows.

Before deposition, the sputter chamber is kept in vacuum to minimize the impurity level [36]. In our deposition, the residual gas pressure is $3 \cdot 10^{-6}$ Pa. During deposition, the flow of sputter gas (Ar and CH₄ in our case) into the chamber increases the pressure. The working pressure is kept constant by controlling the sputter gas flow rate and the pumping speed. The sputter gas flow rate is measured and controlled by mass flow controllers (MFC).

A planar magnetron mounted behind the target creates a magnetic field gradient and confines the electron motion close to the target surface. In a magnetic field \mathbf{B} , electrons move in cycloidal motion as represented by the black lines around the magnetic field (pink lines) in Fig. 3.1 (b). This confinement prolongs the electron life time in the plasma so that the high deposition rate can be realized at lower gas pressure. Target

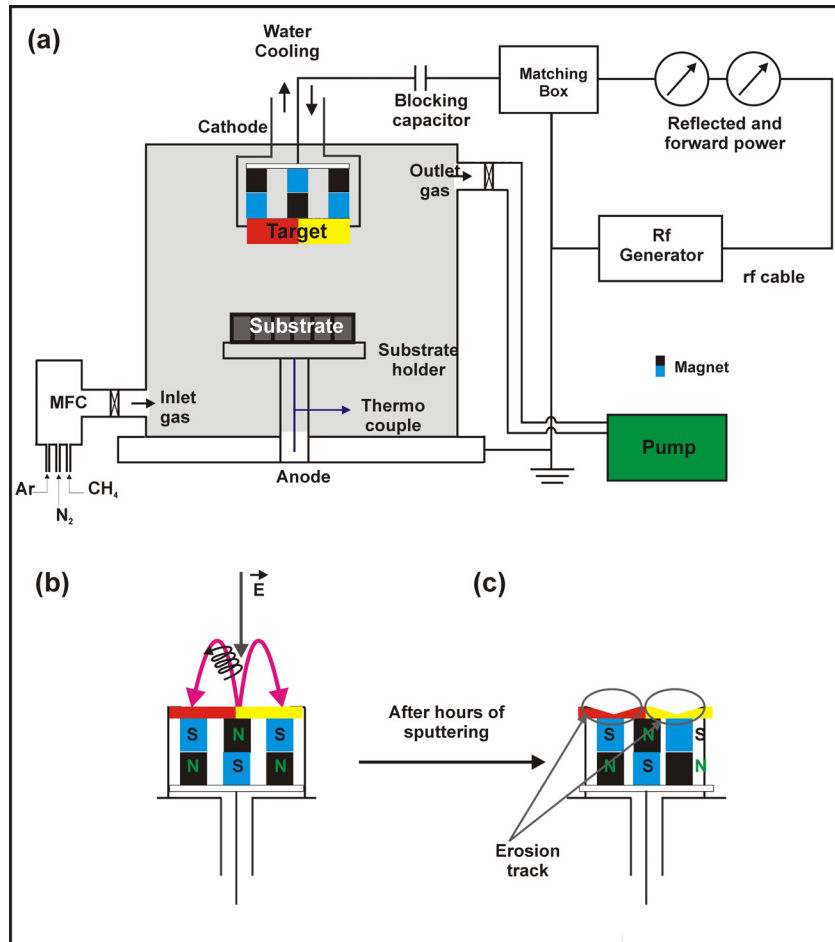


Figure 3.1: (a) Cross section of an rf magnetron sputtering chamber, (b) electron confinement and (c) erosion track of the target.

atoms are mostly ejected from the area with larger magnetic field, resulting in an erosion track after hours of sputtering as shown in Fig. 3.1 (c) [37, 38].

A thermocouple is attached close to the sample. It measures the substrate temperature which differs from the growth temperature at the sample surface. The surface temperature is increased due to the energy impact of atoms and the radiation from the plasma.

The energy source which we used for sputtering is a radio frequency (rf) originating from the power supply. The rf source alters automatically the electric field polarity so that it removes positive charge build up on the target surface. Therefore, it can be used to sputter both conductive and insulating materials. However due to the pulsed power, the deposition rate of rf sputtering is generally low compared to DC sputtering. In an rf

Table 3.1: Plasma Processes.

No	Interaction	Processes
1.	Ionization	$A + e \rightarrow A^+ + 2e$
2.	Excitation	$e + A \rightarrow e + A^*$
3.	Relaxation	$e + A^* \rightarrow e + A + h\nu$
4.	Penning ionization	$A + A^* \rightarrow A^+ + A + e$
5.	Charge transfer	$A^+(\text{fast}) + A(\text{rest}) \rightarrow A(\text{fast}) + A^+(\text{rest})$
6.	Dissociation	$e + C_xD_y \rightarrow e + xC + yD$
7.	Recombination	$A^+ + e^- \rightarrow A$

sputtering system, a matching box is used to adjust the impedance so that the power transfer to the plasma is optimized. A blocking capacitor is used to avoid a short circuit between target and ground.

It is reported that 80% of the electric power during sputter deposition is transferred as a heat load to the sputter target [39]. Therefore a water cooling system is mounted close to target to enhance the target life time.

3.2 Sputter Deposition Processes

Sputter deposition can take place only if (1) a plasma is generated and sustained, (2) energetic particles such as ions (generated in the plasma) bombard the target and (3) the ejected target atoms are deposited onto substrate.

In the following, the reactions that take place in the plasma, between plasma and target and between plasma and substrate are described.

3.2.1 Interactions in the Plasma

A plasma is a partially ionized gas consisting of an equal number of positive and negative charges. Hence it is quasi neutral. In the sputtering chamber, the plasma is initialized by applying an electrical field between the electrodes. At a given gas pressure, electrode spacing and voltage, the plasma is ignited through an avalanche-like ionization of the sputter gas such as Ar, Kr, N₂ and CH₄ [37].

Plasma species are neutral atoms (A), ionized atoms (A⁺), excited atoms (A^{*}), neutral

molecules (C_xD_y), electrons (e) and photons. They mainly come from the sputter gas, target bombardment, plasma species interaction and re-sputtering of deposited atoms from substrate. They sustain the plasma by several processes such as ionization, excitation, relaxation, dissociation, charge transfer and recombination [37, 38] as listed in table 3.1 and described in the following.

Energy is transferred when an electron collides with a neutral gas. If the transferred energy is higher than the ionization threshold of neutral atom, the atom is ionized by releasing an electron (interaction no. 1). Recombination of a positive ion and an electron produces a neutral atom and hence this decreases electron concentration in plasma (reaction no. 7).

At lower transferred energy, a valence electron of an atom is excited to higher state (interaction no. 2). This excited state is not stable. The electron decay to the ground state is accompanied by photon emission with energy $h\nu$ which leads to the characteristic color of the plasma (interaction no. 3). If the excited atoms have an energy higher than the ionization potential of an atom, they might ionize neutral atom (interaction no. 4). Collision between an electron and a molecule such as CH_4 may dissociate this molecules into neutral atom (reaction no. 6).

The collisions between sputter gas atoms and electrons play a significant role in the sputter deposition. This collision produces a positive ion which then bombards the target, ejects the atoms and creates electrons for a successive plasma process.

3.2.2 Interactions between Plasma Species and Target

In a sputtering chamber, the target is mounted on a negative electrode. The dominant plasma species which bombards the target is positively ionized sputter gas such as Ar^+ . Most of the incident ions bombard the target with an angle 90° relative to the target surface [33, 36].

Depending on the incident energy, several possible interactions may take place when sputter gas ion bombards the target surface. They are shown schematically in Fig. 3.2 (a). The collision between high energy incident ions and target atoms might cause (1) sputtering of target atoms, (2) generation of secondary electrons, (3) collision cascades which displace target atoms from their site (see gray area in the figure), (4) implantation of bombarding ions into the target and (5) implantation of target atoms into deeper subsurface regions. The incident ions with low energy might be reflected from the target surface (number 6) [33].

In the presence of reactive gases such as CH_4 (as in our case) target atoms might un-

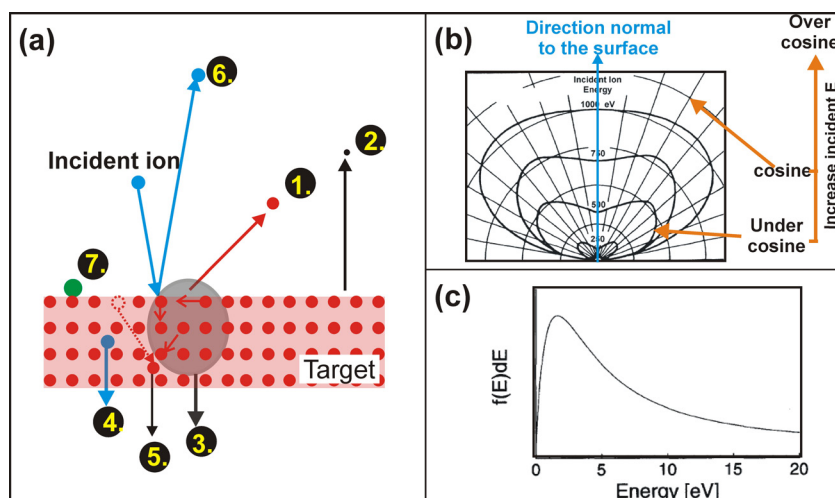


Figure 3.2: (a) Schematic of interaction between ionized sputter gas and target [Adapted from [37]], (b) angular distribution [34] and (c) typical energy distribution of the sputtered atoms [38].

dergo a chemical reaction with these reactive molecules and form a compound layer on the target surface (number 7). This might lead to target poisoning which prevents a successive sputtering [37, 40].

Amongst other interactions between the bombarding ions and the target, sputtering of the target atoms and generation of secondary electrons are the most important for the deposition process. The secondary electrons are then repelled by the negative electrode, enter the plasma and take part in the plasma processes as described in section 3.2.1.

Most of the sputtered particles are neutrals and leave the target with an angular and energy distribution. The angular distribution of the sputtered atoms depends on (1) target materials, (2) sputter gas, (3) energy of incidents ions and (4) incident angle of the bombarding ions. Figure 3.2 (b) shows an example for the angular distribution of sputtered atoms of a polycrystalline target bombarded by ions at different incident energy as presented in reference [34]. At lower ion energy, the target atoms are sputtered more to the side relative to the surface normal directions (under-cosine distribution). At higher ion energy, a cosine distribution is observed. The typical energy distribution of sputtered particles is presented in Fig. 3.2 (c) which shows a maximum at low energy.

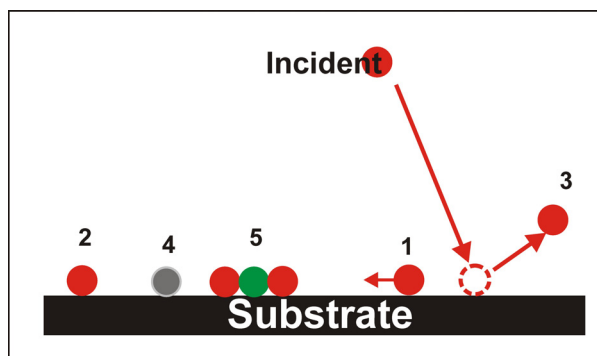


Figure 3.3: Interactions between plasma and substrate: (1) surface diffusion, (2) deposited target atom, (3) re-sputtered atom, (4) deposited sputter gas atom and (5) chemical reaction between deposited target atom and reactive sputter gas atom.

3.2.3 Interactions between Plasma and Substrate

Sputtered atoms from the target are transported through the plasma and arrive on the substrate surface. Figure 3.3 shows schematically the interaction on the substrate surface. Sputtered atoms might (1) diffuse on surface before (2) it is bonded to substrate or (3) being re-sputtered due to the subsequent energetic bombardment [41]. Besides the sputtered atom, (4) the sputter gas may also be trapped as impurities in the coating [42].

Beside the interactions illustrated in Fig. 3.3, similar interactions as at the target may also occur on the substrate, e.g. collision cascade.

Depending on the interaction between sputtered atoms and plasma species, the sputtered target atoms might arrive at the substrate surface with different angular distribution compared to the angular distribution when they left the target.

In our deposition process, we use a mixture of Ar and CH_4 as sputter gas. The reactive gas CH_4 may undergo a chemical reaction with the deposited atoms (interaction 5 in Fig. 3.3) which influences the chemical composition of the coating. The reactive gas CH_4 arrives on the substrate randomly and it has a smaller momentum transfer than the momentum transfer of the sputtered target atom.

The fundamental growth parameters of the sputter deposition are the incident energy and the angular distribution of the sputtered atom when arriving at the substrate as well as the substrate temperature. These factors are controlled by a combination of process parameters, i.e. the type of sputter gas, working pressure, the applied power, the target-substrate distance and the substrate bias. The influence of each parameter on

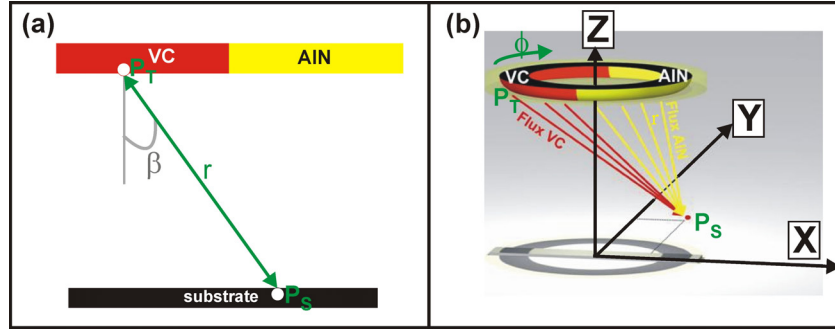


Figure 3.4: (a) Cross section of the target-substrate geometry, (b) incoming flux at a point P_S on substrate surface is sum of the flux from the VC and the AlN target area (courtesy of B. Krause).

the deposition process is discussed elsewhere, e.g. in the references [18, 19, 36, 38, 41, 43].

In the following, the calculated flux distribution during the deposition of our V-Al-C-N hard coatings from a segmented target is described.

3.3 Combinatorial Approach

V-Al-C-N is a new material system for hard coating applications. There are many parameters to be varied and optimized. The optimization approach where one sample is deposited and characterized, followed by deposition and characterization of another sample, requires a large number of samples and is very time-consuming [44]. Therefore a combinatorial approach, similar to the pioneering work at Berkeley [45], is used. In the combinatorial approach, several coatings are deposited simultaneously in such a way that the chemical composition is varied [5, 44, 46].

In our work, the combinatorial approach is implemented by using a segmented circular target with 75 mm diameter. It consists of half a VC target and half an AlN target. Several substrates are placed below the target. The schematic cross section of the target-substrate arrangement is shown in Fig. 3.4 (a). Figure 3.4 (b) illustrates schematically that the incident flux onto a given substrate position P_S is coming from the entire VC and AlN target area.

As described in section 3.1, the target atoms are not ejected homogeneously from the entire target area. Figure 3.4 (b) shows schematically the region of the target which has higher probability to be sputtered (erosion track). The Cartesian coordinate system of

the substrate-target arrangement is indicated.

The simulation of the flux distribution during V-Al-C-N deposition was performed by Dr. B. Krause (Institute for Synchrotron Radiation (ISS), Karlsruhe, Germany). The assumptions and the calculated result are described as follows.

3.3.1 Calculated Flux Distribution

The sputtering yield Y is defined as the number of atoms sputtered from the target per incident bombarding ion [34]. The Y of a point source is approximated by [43]:

$$Y(\beta) \sim \cos^n \beta \quad (3.1)$$

where β is the angle between sputtered particle and surface normal as shown in Fig. 3.4 (a). The constant n depends on the incident energy. At low ion energy, n is typically in the range of $0 < n < 1$ while at higher energy $1 < n < 2$ [38].

The region of the target which has higher probability to be sputtered is experimentally determined by measuring the erosion area of the target after hours of sputtering. The erosion area of the segmented VC-AlN target has a Gaussian profile as shown on top of Fig. 3.5 (b) and (c). The erosion area of the VC target is larger than the erosion area of the AlN target. This indicates that the sputtering yield of VC is larger than the sputtering yield of AlN.

The deposition of our coatings was performed at the sputter gas pressure 0.6 Pa using a mixture of Ar + 2%CH₄ as sputter gas. The relation between the pressure, the temperature and the mean free path λ_{mfp} of two particles is [34]:

$$\lambda_{mfp} = \frac{k_B T}{\sqrt{2}\pi(r_1 + r_2)^2 P} \quad (3.2)$$

where k_B is the Boltzmann constant (1.38×10^{-23} Pa·m³·K⁻¹), T is the temperature, r_1 and r_2 are the radius of the colliding particles ($r_V = 135$ pm and $r_{Ar} = 71$ pm [47]) and P is the pressure. The deposition temperature was not measured, however assuming $T = 150^\circ$ (this is the substrate temperature. The deposition temperature is expected higher than this value), the mean free path of Vanadium in the sputter gas is ≈ 5.2 cm. Other target atoms (C, Al and N) are smaller than Vanadium, thus their mean free paths are larger than the mean free path of Vanadium.

The incident flux towards the substrate is proportional to: (1) the sputtering yield $Y(\beta)$, (2) $(1/r^2)$ where r is the distance between a point source P_T and a given position on the substrate P_S , (3) the projection of the flux on the substrate $\cos\beta$ and (4) the Gaussian function of the target erosion area $G(P_T)$. Thus the incident flux at any position on substrate from a point source $F(P_S, P_T)$ is formulated as:

$$F(P_S, P_T) = \frac{Y(\beta)}{r^2} \cdot \cos\beta \cdot G(P_T) \quad (3.3)$$

Assuming no collision between the sputtered particles and the sputter gas in the plasma, the total incident flux $F(P_S)$ is formulated as:

$$F(P_S) = \int_{VC \text{ area}} F(P_S, P_T)_{VC} \cdot dA_{VC} + C \int_{AlN \text{ area}} F(P_S, P_T)_{AlN} \cdot dA_{AlN} \quad (3.4)$$

where A_{VC} and A_{AlN} are the area of VC and AlN target respectively. The constant C is the deposition rate ratio of R_{AlN} and R_{VC} . The value for C is determined experimentally from the concentration ratio of AlN and VC at $X = 0$. At this position, the chemical composition of the coating is not influenced by the target-substrate arrangement. We found that C is equal to $1/3$. In our calculation, the value for n is taken as 1.5. We have verified that the n values does not influence significantly the flux distribution.

In order to verify our model, the simulated thickness and the Al to (Al+V) ratio are compared to the measured data. Figure 3.5 (a) shows the simulated and measured thickness and Al to (Al+V) ratio as a function of position below the target X.

The open black circles are the measured thickness while the black line represents the simulated thickness. In the range of $-20 < X < 10$ mm, the simulated thickness fits with the measured thickness. Beyond this range, a small deviation between the measured and the simulated thickness is observed. This might be explained by the opposite edge effect where collisions of the sputtered particles and the plasma species are more significant.

Figure 3.5 (a) indicates the simulated (red solid line) and the measured (open red circle) Al to (Al+V) ratio. It shows that the simulated and the measured values are in agreement.

Both the simulated thickness and Al to (Al+V) ratio do not deviate significantly from the measured data. This means that our model is a good approximation to simulate the general features of the flux distribution during VC-AlN deposition. The simulated flux distribution is shown in Fig. 3.5 (b) and (c).

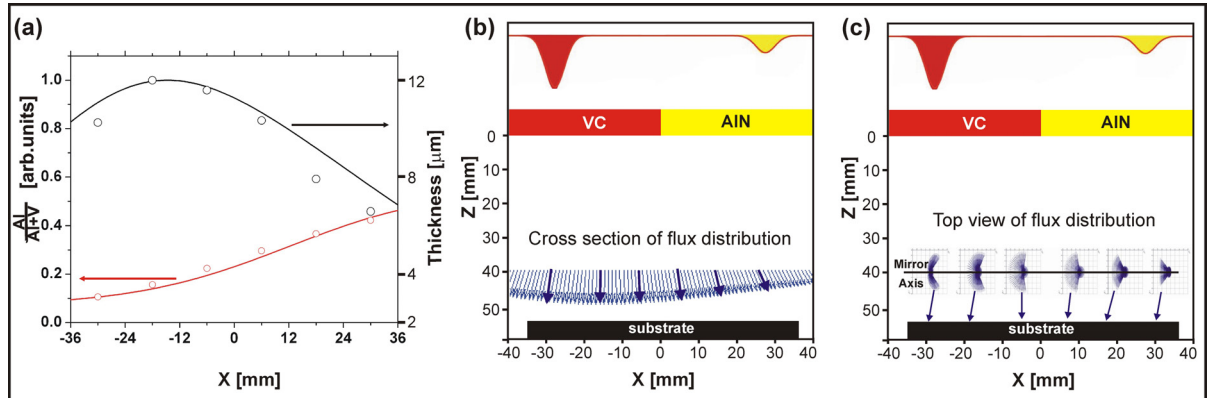


Figure 3.5: (a) Solid line: the calculated Al/(Al+V) ratio and thickness, points: measured data, (b) cross section of flux distribution at $Y = 0$ mm and (c) top view of flux distribution towards the substrate (courtesy of B. Krause).

Figure 3.5 (b) shows the cross section of the calculated flux distribution as a function of X at $Y = 0$. The blue arrows indicate the direction and the magnitude of the incident flux. The flux is larger at positions below the VC part than below the AlN part.

The lateral distribution of the incident flux is shown in figure 3.5 (c). The local flux distribution has a two-fold symmetry with the mirror axis parallel to the X axis. This is expected because mirror axis of the target is also in this direction.

4 Microstructure Analysis by X-Ray Scattering

It has been described in chapter 2 that the coatings properties are influenced by their microstructure e.g. crystal structure, lattice parameter, crystallographic orientation and residual stress. X-ray scattering is used as the main microstructure analysis of the samples studied in this work. The x-ray scattering methods are described in this chapter.

The organization of the chapter is as follows. Section 4.1 describes briefly the basics of x-ray scattering. The formulas for lattice parameter, angle between two lattice planes and volume of cubic, rhombohedral and hexagonal unit cell are given in section 4.2. The allowed reflections of typical crystal structures of hard coating materials are described in section 4.3. This will be used later to determine crystal structure of V-Al-C-N (see section 8 and 9).

The size and strain broadening are described in section 4.4. Section 4.5 discusses how the intensity distribution in reciprocal space maps and pole figures is influenced by the crystallographic orientation, i.e. whether the coating is single crystalline, random polycrystalline or textured. The correction factor of the measured intensity is given in section 4.6. The last section 4.7 describes the residual stress analysis by x-ray diffraction.

For a basic understanding of x-ray scattering, crystallography and elastic property (necessary for residual stress analysis), the references [48, 49, 50, 51] are recommended.

4.1 X-Ray Scattering

In this section, Bragg's law and the Laue condition for constructive interference and the scattering amplitude from a crystal are summarized.

4.1.1 Bragg's Law and Laue condition

The scattering process from atoms (red dots) arranged in a crystal lattice is illustrated in Fig. 4.1 (a). The x-ray beam (green line) with the wave vector \mathbf{k}_i and the incident angle θ relative to the lattice plane (black line) illuminates the atoms. The x-ray beam is then scattered with the scattering angle θ and the wave vector \mathbf{k}_f . In the kinematic

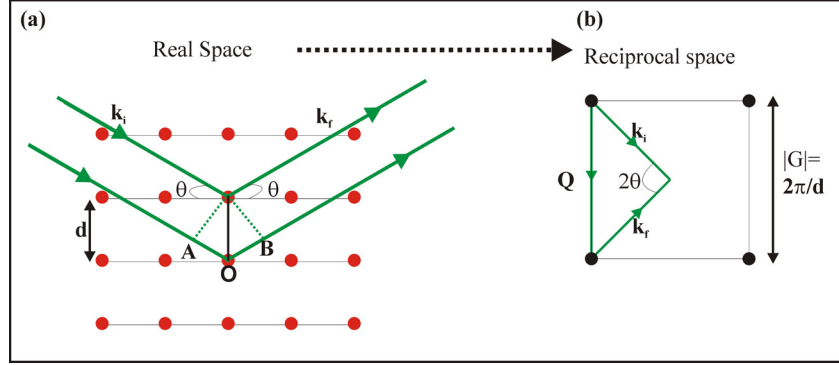


Figure 4.1: Schematic illustration of the scattering from a crystal lattice in (a) real space and (b) reciprocal space (adapted from [49]).

approximation, $|\mathbf{k}_i| = |\mathbf{k}_f| = 2\pi/\lambda$ where λ is the x-ray wavelength in Angström.

AOB in this figure is a path length difference between the scattering at neighboring lattice planes. From the geometry, AOB is equal to $2d\sin\theta$ where d is a lattice spacing. If the path length difference is equal to the integer multiple of λ , the constructive interference occurs which is formulated as Bragg's law:

$$n\lambda = 2d\sin\theta \quad (4.1)$$

The momentum transfer \mathbf{Q} is defined as $\mathbf{k}_f - \mathbf{k}_i$ where the $|\mathbf{Q}|$ is given by:

$$|\mathbf{Q}| = \frac{4\pi\sin\theta}{\lambda} \quad (4.2)$$

Figure 4.1 (b) shows schematically the triangle formed by the incident wave vector \mathbf{k}_i , the scattered wave vector \mathbf{k}_f and the momentum transfer \mathbf{Q} in the reciprocal space.

The black dots in Fig. 4.1 (b) represent reciprocal lattice points where the reciprocal lattice vector \mathbf{G} is defined as $2\pi(h\mathbf{a}_1^* + k\mathbf{a}_2^* + l\mathbf{a}_3^*)$ and $|\mathbf{G}| = 2\pi/d_{hkl}$. (h,k,l) are the Miller indices of a given lattice plane and \mathbf{a}_1^* , \mathbf{a}_2^* and \mathbf{a}_3^* are reciprocal basis vectors. The Laue condition for constructive interference occurs if $\mathbf{Q} = \mathbf{G}$:

$$Q = \frac{4\pi}{\lambda}\sin\theta = \frac{2\pi}{d} \quad (4.3)$$

The relation between real space and reciprocal space basis vectors is given below :

$$a_1^* \cdot a_2 = a_1^* \cdot a_3 = a_2^* \cdot a_1 = a_2^* \cdot a_3 = a_3^* \cdot a_1 = a_3^* \cdot a_2 = 0 \quad (4.4)$$

$$a_1^* \cdot a_1 = a_2^* \cdot a_2 = a_3^* \cdot a_3 = 1 \quad (4.5)$$

where a_1 , a_2 and a_3 are the real space basis vector.

4.1.2 Structure Factor of a Crystal

The scattering amplitude of a crystal $F_{crystal}$ is the sum of scattering of all atoms in the lattice:

$$F_{crystal}(Q) = \sum_{r_j} \underbrace{f_j(Q) e^{i\vec{Q} \cdot \vec{r}_j}}_{unitcell} \sum_{R_n} \underbrace{e^{i\vec{Q} \cdot \vec{R}_n}}_{lattice} \quad (4.6)$$

The first term in equation 4.6 is called unit cell structure factor which depends on the atomic scattering factor f_j , the momentum transfer \mathbf{Q} and the atomic positions in a unit cell \mathbf{r}_j .

The atomic scattering factor f_j is the sum of the atomic scattering factor without correction f_j^0 , the real part and the imaginary part of the dispersion correction factors f' and f'' [49]:

$$f_j(Q, E) = f_j^0(Q) + f'(E) + if''(E) \quad (4.7)$$

$f_j^0(Q)$ has been approximated analytically by:

$$f_j^0(Q) = \sum_{i=1}^4 a_i e^{-b_i (\frac{Q}{4\pi})^2} + c \quad (4.8)$$

a_j , b_j and c are constants specific for the material. The coatings studied in this work consist of V, Al, C, and N. Their a_j , b_j and c are given in table 4.1.

The second term of the scattering amplitude is called lattice sum. The value depends on size and shape of the crystallites. The influence of size of cylindrical crystallites will be described in section 4.4.1.

Table 4.1: Fitting parameters for the atomic scattering factor calculation of V, Al, C and N [52].

Parameter	V	Al	C	N
a_1	10.297	6.420	2.310	12.213
a_2	0.439	1.900	1.020	3.132
a_3	2.070	1.594	1.589	2.013
a_4	2.057	1.965	0.865	1.166
b_1	6.866	3.039	20.844	0.006
b_2	7.351	0.743	10.208	9.893
b_3	26.894	31.547	0.056	28.998
b_4	102.478	85.089	51.651	0.583
c	1.220	1.115	0.216	-11.529

4.2 Cubic, Rhombohedral and Hexagonal Unit Cells

The Bragg equation (Eq. 4.1) formulates the relation between the lattice spacing d_{hkl} , the scattering angle θ and the wave length of the x-ray beam λ for the constructive interference. In this section, the relation between the lattice spacing and the crystal phase are shown.

The expected crystal phases of the V-Al-C-N coatings used in our works are cubic or hexagonal (see chapter 2). For a cubic unit cell, the lattice parameters have the same size ($a = b = c$). The angles α , β and γ are also same, i.e. 90° .

Figure 4.2 (a) shows the (111) oriented cubic unit cell. Due to the lateral compression, a (111) oriented cubic unit cell might be distorted to a rhombohedral unit cell as shown in Fig. 4.2 (b). As in a cubic unit cell, all lattice parameters of a rhombohedral unit cell have the same size. The angles α , β and γ are equal, however they are smaller than 90° .

The formulas for the calculation of lattice parameter a , the volume V and the cosinus of the angle between two planes (h_1, k_1, l_1) and (h_2, k_2, l_2) $\cos \phi$ of rhombohedral unit cell are given below [53]:

$$d_{hkl}^2 = \frac{a^2(1 - 3 \cos^2 \alpha + 2 \cos^3 \alpha)}{(h^2 + k^2 + l^2) \sin^2 \alpha + 2(hk + kl + hl)(\cos^2 \alpha - \cos \alpha)} \quad (4.9)$$

$$V = a^3 \sqrt{1 - 3 \cos^2 \alpha + 2 \cos^3 \alpha} \quad (4.10)$$

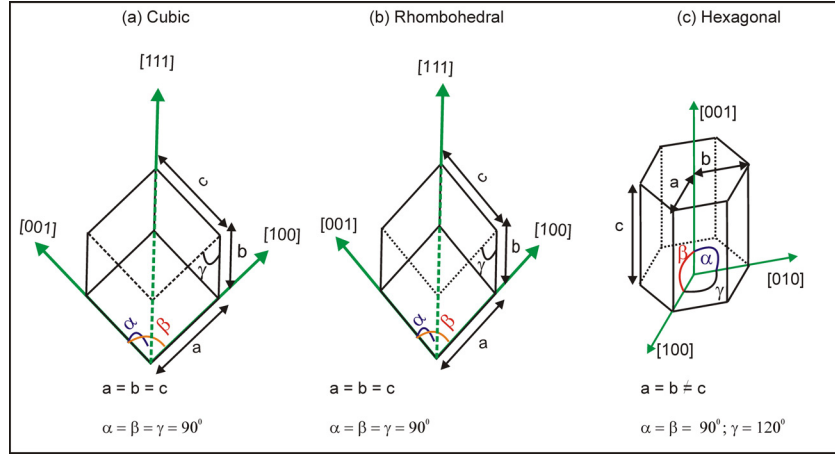


Figure 4.2: (a) cubic, (b) rhombohedral and (c) hexagonal unit cells.

$$\cos \phi = \frac{a^4 d_1 d_2}{V^2} [\sin^2 \alpha (h_1 h_2 + k_1 k_2 + l_1 l_2) + (\cos^2 \alpha - \cos \alpha) (k_1 l_2 + l_1 h_2 + h_1 k_2 + k_2 l_1 + l_2 h_1 + h_2 k_1)] \quad (4.11)$$

where d_1 and d_2 are the lattice spacings of $(hkl)_1$ and $(hkl)_2$ planes respectively. Lattice parameter, volume and angle between planes of a cubic unit cell can be calculated from Eq. 4.9 - Eq. 4.11 by inserting $\alpha = 90^\circ$ so that:

$$d_{hkl}^2 = \frac{a^2}{(h^2 + k^2 + l^2)} \quad (4.12)$$

$$V = a^3 \quad (4.13)$$

$$\cos \phi = \frac{h_1 h_2 + k_1 k_2 + l_1 l_2}{\sqrt{(h_1^2 + k_1^2 + l_1^2)(h_2^2 + k_2^2 + l_2^2)}} \quad (4.14)$$

A hexagonal unit cell is shown in Fig. 4.2 (c) where lattice parameters and angles between principle axis are $a = b \neq c$ and $\alpha = \beta = 90^\circ$, $\gamma = 120^\circ$. Lattice parameter, volume and angle between the planes are calculated from equation 4.15 to 4.17.

$$\frac{1}{d_{hkl}^2} = \frac{4}{3} \left(\frac{h^2 + k^2 + hk}{a^2} \right) + \frac{l^2}{c^2} \quad (4.15)$$

$$V = \frac{\sqrt{3}}{2} a^2 c \quad (4.16)$$

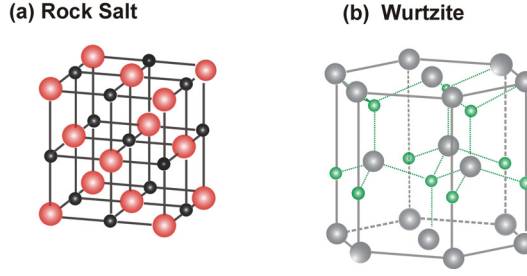


Figure 4.3: Crystal structure of (a) rock salt and (b) wurtzite structure.

$$\cos \phi = \frac{h_1 h_2 + k_1 k_2 + \frac{1}{2}(h_1 k_2 + h_2 k_1) + \frac{3a^2}{4c^2} l_1 l_2}{\sqrt{(h_1^2 + k_1^2 + h_1 k_1 + \frac{3a^2}{4c^2} l_1^2)} \sqrt{(h_2^2 + k_2^2 + h_2 k_2 + \frac{3a^2}{4c^2} l_2^2)}} \quad (4.17)$$

4.3 Allowed Reflections of the Rock Salt and the Wurtzite Structure

The unit cell structure factor $F_{u.c}$ depends on the atomic scattering factor f_j and the atomic position in a unit cell r_j at given momentum transfer \mathbf{Q} , i.e. $F_{u.c} = \sum_{r_j} f_j(Q) e^{i\mathbf{Q} \cdot \mathbf{r}_j}$.

For our material system V-Al-C-N, the expected crystal structures of the coating depend on the chemical composition. At high VC concentration, the rock salt structure is expected while at high AlN concentration, the wurtzite structure is expected (see chapter 2).

The atomic positions r_j in the rock salt and in the wurtzite structure are different, therefore the characteristic peak positions of each structure are different. Allowed reflection of rock salt (space group $Fm\bar{3}m$) and wurtzite (space group $P63mc$) structures are described as follows.

Figure 4.3 (a) shows the unit cell of rock salt structure. The rock salt structure consists of two fcc lattices where the atomic positions of the first fcc lattice (red spheres in Fig. 4.3 (a)) are $(0,0,0)$, $(1/2,1/2,0)$, $(0,1/2,1/2)$ and $(1/2,0,1/2)$. The second fcc lattice (black spheres in Fig. 4.3 (a)) is translated by $(1/2, 1/2, 1/2)$ from the first fcc lattice.

$F_{rock\ salt}$ is then calculated by inserting r_j into the first term of Eq. 4.6. The detailed derivation is given in Appendix A. Assuming that Vanadium occupies the first lattice and Carbon occupies the second lattice, the allowed reflections of the rock salt structure are:

$$F = \left\{ \begin{array}{ll} 0 & \text{for mixed indices} \\ 4(f_V + f_C) & \text{if all h, k, l are even} \\ 4(f_V - f_C) & \text{if all h, k, l are odd} \end{array} \right\} \quad (4.18)$$

where f_V is the atomic scattering factor of V and f_C is the atomic scattering factor of C.

The wurtzite structure (space group $P63mc$, #186) consists of two types of atoms arranged in a hexagonal lattice e.g. AlN. The first type of atoms (Al) occupies the (0,0,0), (1/3, 2/3, 0) and (2/3, 1/3, 1/2) sites while the second type of atoms (N) occupies the (0,0,0.38), (1/3, 2/3, 0.38) and (2/3, 1/3, 0.88) positions. By substituting those atomic positions into equation 4.6, the allowed reflections for wurtzite AlN are summarized as:

$$F \neq 0 \text{ if } \left\{ \begin{array}{l} l \text{ even} \\ h + 2k \neq 3n \end{array} \right\} \quad (4.19)$$

4.4 Peak Broadening

Depending on the size and strain distribution, the Bragg reflections might be broadened. This broadening is quantified by the Full Width at Half Maximum (FWHM), i.e. the peak width at half of maximum peak intensity. The influence of size and strain distribution to the FWHM are described as follows.

4.4.1 Influence of Size of a Fiber on Peak Broadening

Hard coatings often have a fiber texture as shown schematically in Fig. 4.4 (a). The shape of the fiber can be approximated by a cylinder. The red arrow in this figure represent the fiber axis. The crystallite size and shape influence the second term of the crystal structure factor $F_{shape} = \sum e^{i\vec{Q} \cdot \vec{R}_n}$. Q can be written as:

$$Q = Q_{hkl} + q \quad (4.20)$$

where Q_{hkl} is the momentum transfer at the Bragg reflection and q is defined as $Q - Q_{hkl}$. For a cylinder with the axis oriented parallel to z, the shape function F_{shape} is calculated as [54]:

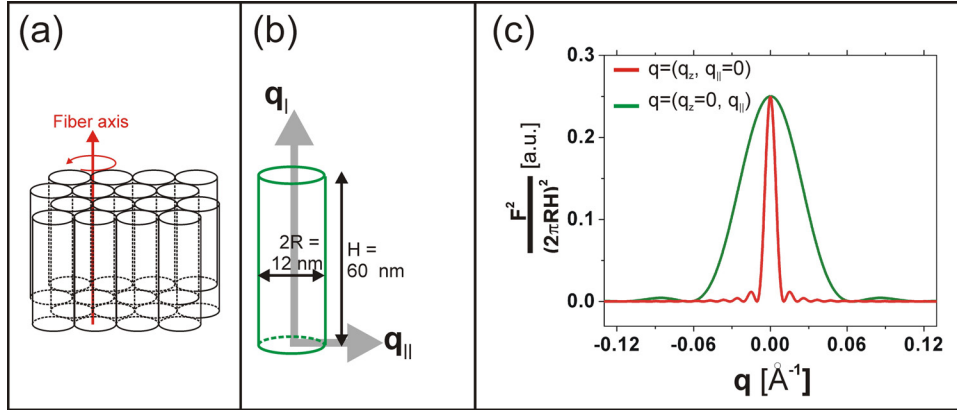


Figure 4.4: (a) Schematic of a fiber texture, (b) cylindrical fiber where q_z is parallel to the cylinder axis and the $q_{||}$ is perpendicular to the cylinder axis, (c) normalized $|F_{shape}|^2$ for two cases.

$$F_{shape}(q, R, H) = 2\pi R^2 H \frac{J_1(q_{||}R)}{q_{||}R} \text{sinc}(q_z H/2) e^{iq_z H/2} \quad (4.21)$$

where $q_{||}$ is $\sqrt{q_x^2 + q_y^2}$, J_1 is first order Bessel function, H is the length of the cylinder and R is the radius of the cylinder. Assuming q_z is zero, the shape function is influenced only by radius of the cylinder. If $q_{||}$ is zero, then the shape function is influenced by the cylinder height only.

The scattering amplitude is proportional to $|F_{shape}|^2$. In order to determine size of the cylinder, the FWHM in two directions is calculated, e.g. for $q_z = 0$ and $q_{||} = 0$. Assuming a cylinder with $R = 6$ nm and $H = 60$ nm, the expected normalized $|F_{shape}|^2$ for these directions are presented in Fig. 4.4 (c). It is shown that the FWHM at $q(q_z = 0, q_{||})$ (influenced only by the radius of cylinder) is larger than the FWHM at $q(q_z, q_{||} = 0)$.

4.4.2 Influence of Strain Distribution on Peak Broadening

The previous section describes that the FWHM of a Bragg reflection in radial direction is influenced by the size, i.e. it is larger for a smaller size. Besides size, the peak broadening is also influenced by the strain distribution.

Figure 4.5 shows schematically three types of polycrystalline material with different strain distribution. The black thick lines represent grain boundaries while the red, green and blue lines represent different lattice planes. The size is assumed large so that size broad-

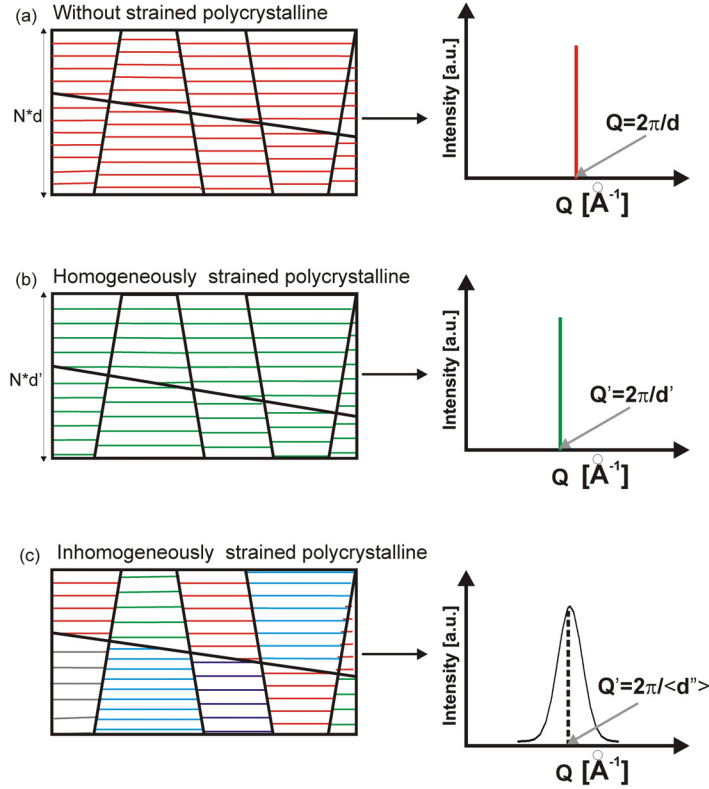


Figure 4.5: Schematic of polycrystalline materials and their Bragg reflection for the case (a) without strain, (b) homogeneously strained, and (c) inhomogeneously strained.

ening is negligible.

Figure 4.5 (a) shows schematically a film consisting of unstrained crystallites which have the same lattice spacing d . At \mathbf{Q} orthogonal to the lattice plane, the peak position is expected at $Q = 2\pi/d$. If the polycrystallite is strained homogeneously as shown in Fig. 4.5 (b), the new lattice spacing d' is equal to $(d + \delta)$ where δ is lattice spacing deviation relative to the strained-free d . Since there is no lattice spacing distribution, the peak position is expected at $Q = 2\pi/d'$ without broadening.

Figure 4.5 (c) shows schematically a film consisting of inhomogeneously strained crystallites where the lattice spacings are distributed in the range of $(d - \delta) < d'' < (d + \delta)$. Thus the (hkl) reflection can be observed in the range $2\pi / (d + \delta) < Q < 2\pi / (d - \delta)$. The peak position is expected at $Q = 2\pi / \langle d'' \rangle$ where $\langle d'' \rangle$ is the average lattice spacing. The peak is broader for a larger strain distribution.

4.4.3 Peak Broadening as a function of the Order of the Reflections

The FWHM in radial direction is influenced by the size and strain distribution of the crystallites. In order to find out which factors are dominating the peak broadening, the FWHM of the same family of reflections can be evaluated.

1. The FWHM is dominated by size broadening.

If the strain broadening is small compared to the size broadening, then the ratio between FWHM of a (hkl) reflection and FWHM of any n^{th} its higher order reflection is:

$$\frac{FWHM_{(nh,nk,nl)}}{FWHM_{(h,k,l)}} \approx 1 \quad (4.22)$$

2. The FWHM is dominated by the strain broadening.

Assuming small size broadening, the FWHM ratio between (hkl) reflection and its n^{th} higher order reflection is :

$$\frac{FWHM_{(nh,nk,nl)}}{FWHM_{(h,k,l)}} \approx n \quad (4.23)$$

4.5 Fiber Texture

The macroscopic properties such as hardness are influenced by the crystallographic orientation (see chapter 2). Therefore it is important to study the crystallographic orientation of the material.

Figure 4.6 presents schematically different types of orientation distribution. The black and red lines represent grain boundaries and crystallographic planes respectively. For each type of orientation, the corresponding expected intensity distribution in reciprocal space is shown.

Figure 4.6 (a) shows a single crystal. The crystallographic planes are oriented parallel to the surface normal with the lattice distance d_{hkl} . In the Q_x/Q_z map, the bragg reflection of this (hkl) plane is expected at $Q_x = 0$ and at $Q_z = 2\pi / d_{hkl}$.

Figure 4.6 (b) shows a polycrystalline material with randomly oriented lattice planes. Therefore the corresponding Q_x/Q_z map of the powder crystallites shows a homogeneous intensity distribution along the powder ring with the radius $2\pi / d_{hkl}$.

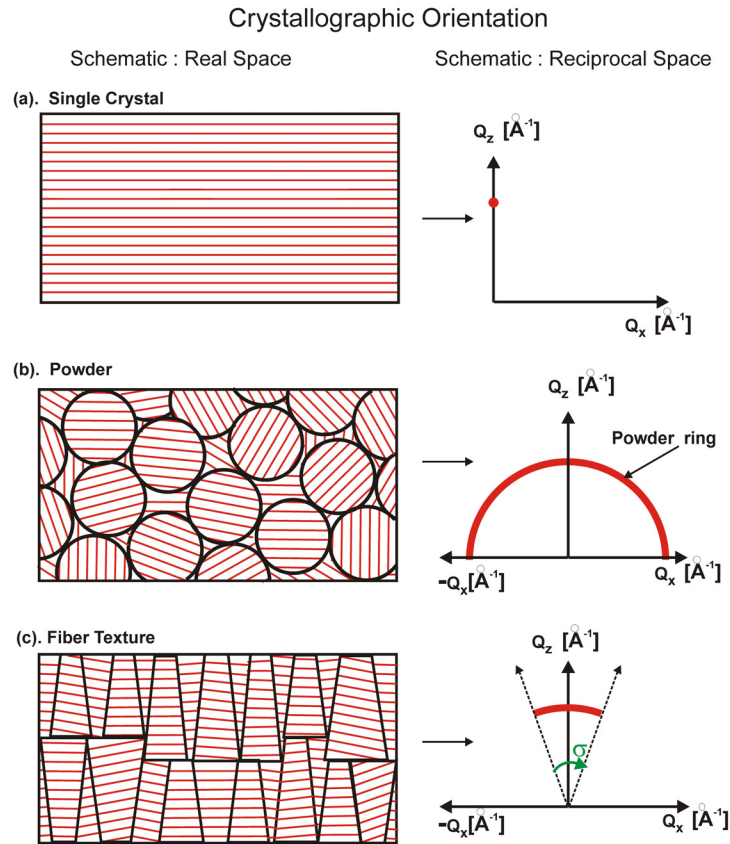


Figure 4.6: Schematic of the crystal orientation of (a) a single crystal (b) a powder and (c) a fiber texture.

The fiber texture is shown schematically in Fig. 4.6 (c). Here, the orientation of the crystal planes is distributed around the surface normal. In the Q_x/Q_z map, the Bragg reflection is expected at $Q_r = 2\pi/d_{hkl}$ (Q_r is Q in the radial direction) with orientation distribution σ_{hkl} (see section 4.5.1-4.5.3).

The (111), (200) and (220) textures are often observed for fcc hard coating materials (section 2). Typically orientation distribution of the fiber axis can be described by a Gaussian distribution around the surface normal without lateral preferential orientation. However, the tilted fiber texture is also reported in several publications. The fiber texture might also have in-plane orientation.

In the following, the crystallographic orientation and symmetry of the (111), the (200) and the (220) textures are described.

4.5.1 (111) Fiber Texture

A cubic unit cell with $[111]$ direction parallel to the surface normal is shown in Fig. 4.7 (a). The orientation of different lattice planes relative to the (111) plane in polar coordinates (Ψ, ϕ) is shown in Fig. 4.7 (b) where black, red and blue spheres represent the $\{111\}$, the $\{200\}$ and the $\{220\}$ family of reflections. (Ψ, ϕ) are related to the angle between the (hkl) planes and (111) . It is seen from Fig. 4.7 (b) that the (111) texture has a three-fold symmetry.

The texture can be studied from pole figures which measure the intensity distribution of a given (hkl) reflection. The intensity distribution of the (111) , the (200) and the (220) pole figure for different types of (111) fiber texture is described as follows.

The (111) , the (200) and the (220) pole figures for (111) fiber texture without lateral orientation are presented schematically in Fig. 4.7 (c) i. For all reflections, Ψ is indicated in this figure. Since the (hkl) plane has no lateral orientation, the intensity is distributed homogeneously along $0 < \phi < 360^\circ$ and forms a (hkl) ring. The intensity of this ring is proportional to the multiplicity, i.e. number of reflections that have same Ψ . The multiplicity of the reflections $(\bar{1}\bar{1}1)$, (200) and (220) is three and the multiplicity of $(2\bar{2}0)$ reflection is six.

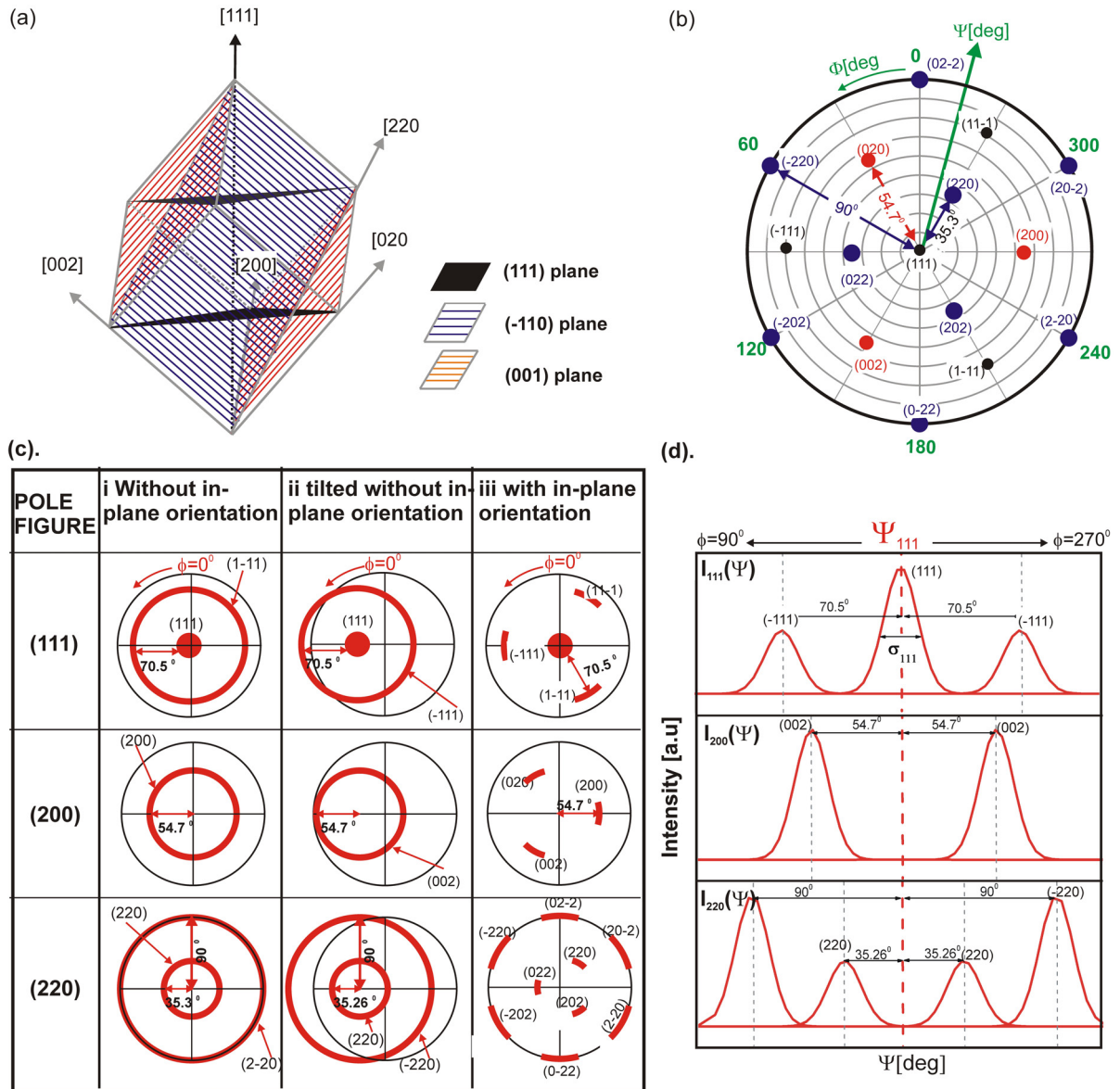


Figure 4.7: (a) A cubic unit cell with [111] orientation parallel to the surface normal, (b) orientation of different lattice planes relative to the (111) plane in polar coordinates, (c) schematic of (111), (200) and (220) pole figures for different types of (111) fiber textures, and (d) expected peak position for the (111) texture as a function of Ψ .

If the average orientation of the (111) fiber texture is tilted relative to the surface normal, then the (111) reflection is shifted from center of the pole figure. The intensity distribution is also shifted towards this tilting angle as shown in Fig. 4.7 (c) ii. If the tilt

Table 4.2: Angle between plane $\Delta\Psi$ [deg].

(hkl) plane	(111)	(200)	(220)
(111)	0	54.7	35.3
($\bar{1}\bar{1}1$)	70.5	54.7	90
($2\bar{2}0$)	90	45	90
(020)	54.7	90	45

angle is large, some of the intensity might not be within the accessible Q range above the sample surface, e.g. in the (220) pole figure, only part of the ($2\bar{2}0$) ring is expected.

The third type of texture described here is the texture with in-plane orientation. In this case, the intensity of the (hkl) reflection is not distributed in the entire ϕ range as shown in Fig. 4.7 (c) iii. The three-fold symmetry of the [111] orientation is expected.

Assuming that the intensity distribution $I_{hkl}(\Psi)$ is Gaussian with the average orientation Ψ_{111} and the distribution σ_{111} , the intensity distribution can be written as:

$$I_{hkl}(\Psi) = \text{Constant} \times \frac{1}{\sqrt{2\pi\sigma_{111}^2}} e^{-\frac{(\Psi-\Psi_{hkl})^2}{2\sigma_{111}^2}} \quad (4.24)$$

where $\Psi_{hkl} = \Psi_{111} + \Delta\Psi$. $\Delta\Psi$ is the angle between the (hkl) and the (111) planes (calculated with Eq. 4.14) as listed in table 4.2.

Figure 4.7 (d) shows schematically the expected (111), (200) and (220) line scans for the (111) texture without in-plane orientation. If the distribution σ_{111} is large, the peaks of the line scans might be overlapping. $\{1\bar{1}1\}$ has lower intensity than (111) because the intensity of $\{1\bar{1}1\}$ is distributed along a ring which is not the case for the (111) reflection. From the multiplicity, the intensity ratio of $\{220\}$ and $\{2\bar{2}0\}$ is 1:2.

If the texture has in-plane orientation, the reflection is only observed at certain ϕ depending on the lateral distribution.

4.5.2 (200) Fiber Texture

Figure 4.8 (a) shows a cubic unit cell where the [002] direction is oriented parallel to the surface normal. The orientation of other reflections relative to (200) in polar coordinates is presented in Fig. 4.8 (b). It is seen that (200) texture has a four-fold symmetry.

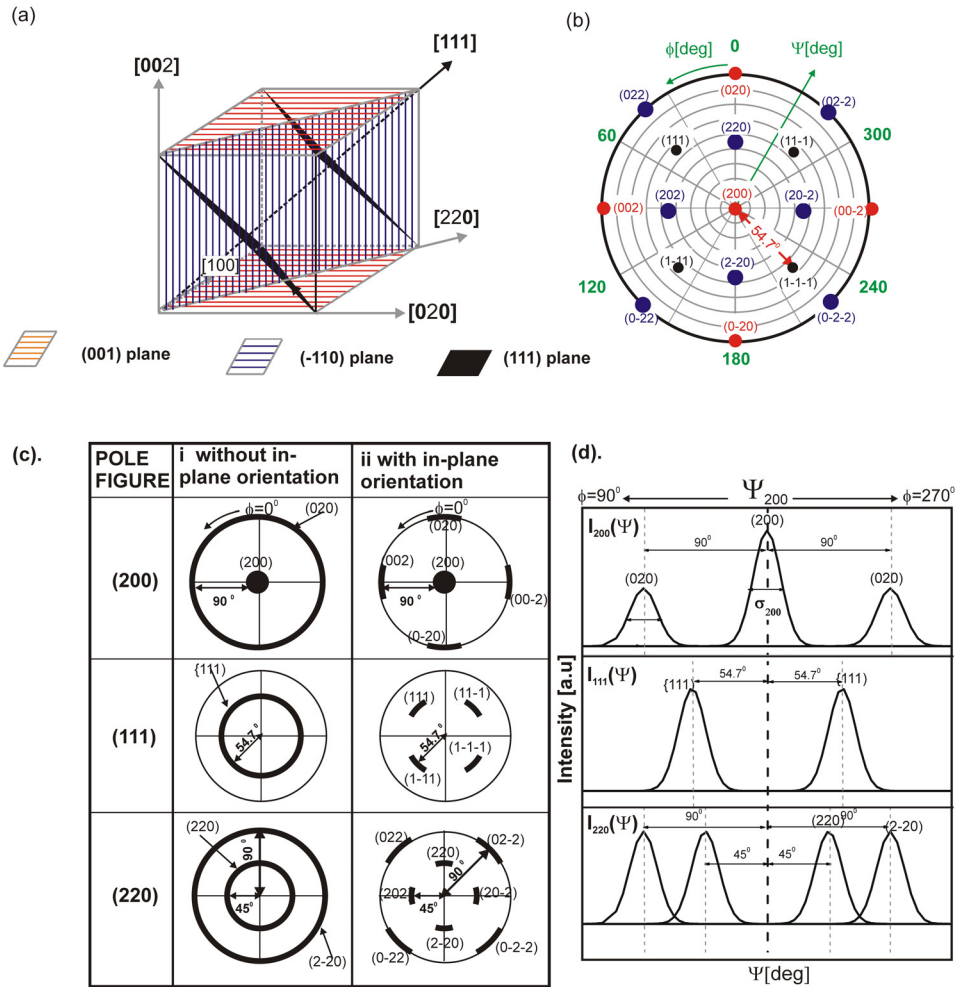


Figure 4.8: (a) A cubic unit cell with $[200]$ orientation parallel to the surface normal, (b) orientation of different lattice planes relative to the (200) plane in polar coordinates, (c) schematic of the (200), (111) and (220) pole figures for different types of (200) fiber textures, and (d) expected peak positions for the (200) texture as a function of Ψ .

Figure 4.8 (c) shows schematically the (111), the (200) and the (220) pole figures for the (200) texture. The expected Ψ is indicated in the figure. For texture without in-plane orientation, the intensity of all reflections other than the (200) reflection is distributed homogeneously along the (hkl) ring. The intensity distribution with four-fold symmetry around the $[200]$ axis is expected if the (200) texture has in-plane orientation.

Figure 4.8 (d) shows schematically the expected (hkl) peak positions which are calculated in the same way as for (111) texture, i.e. the intensity distribution as a function of Ψ

is Gaussian with the average orientation Ψ_{200} and distribution σ_{200} (see equation 4.25). The intensity of a (hkl) reflection is:

$$I_{hkl}(\Psi) = \text{Constant} \times \frac{1}{\sqrt{2\pi\sigma_{200}^2}} e^{-\frac{(\Psi-\Psi_{hkl})^2}{2\sigma_{200}^2}} \quad (4.25)$$

where $\Psi_{hkl} = \Psi_{200} + \Delta\Psi$. $\Delta\Psi$ is angle between any (hkl) and (200) plane which has positive value for the peak in the $\phi = 270^\circ$ direction and negative for the peak in the $\phi = 90^\circ$ direction.

4.5.3 (220) Fiber Texture

Figure 4.9 (a) shows the crystallographic orientation of a cubic unit cell where the [220] direction is oriented parallel to the surface normal. The corresponding orientation of all other reflections relative to the (220) reflection is given in Fig. 4.9 (b). The figure has a two-fold symmetry around [220] axis.

Figure 4.9 (c) shows schematically the (111), the (200) and the (220) pole figures for (220) texture. Without in-plane orientation, the (hkl) rings are observed at Ψ indicated in the figure. If the texture has in-plane orientation, two-fold symmetry which is a characteristic feature of the (220) texture is expected.

The expected peak positions in Fig. 4.9 (d) are calculated in the same way as for the (111) and the (200) textures. Assuming the Gaussian distribution, the relation between the average orientation Ψ_{220} , the distribution σ_{220} , and the intensity $I_{hkl}(\Psi)$ of (220) texture is:

$$I_{hkl}(\Psi) = \text{Constant} \times \frac{1}{\sqrt{2\pi\sigma_{220}^2}} e^{-\frac{(\Psi-\Psi_{hkl})^2}{2\sigma_{220}^2}} \quad (4.26)$$

where $\Psi_{hkl} = \Psi_{220} + \Delta\Psi$.

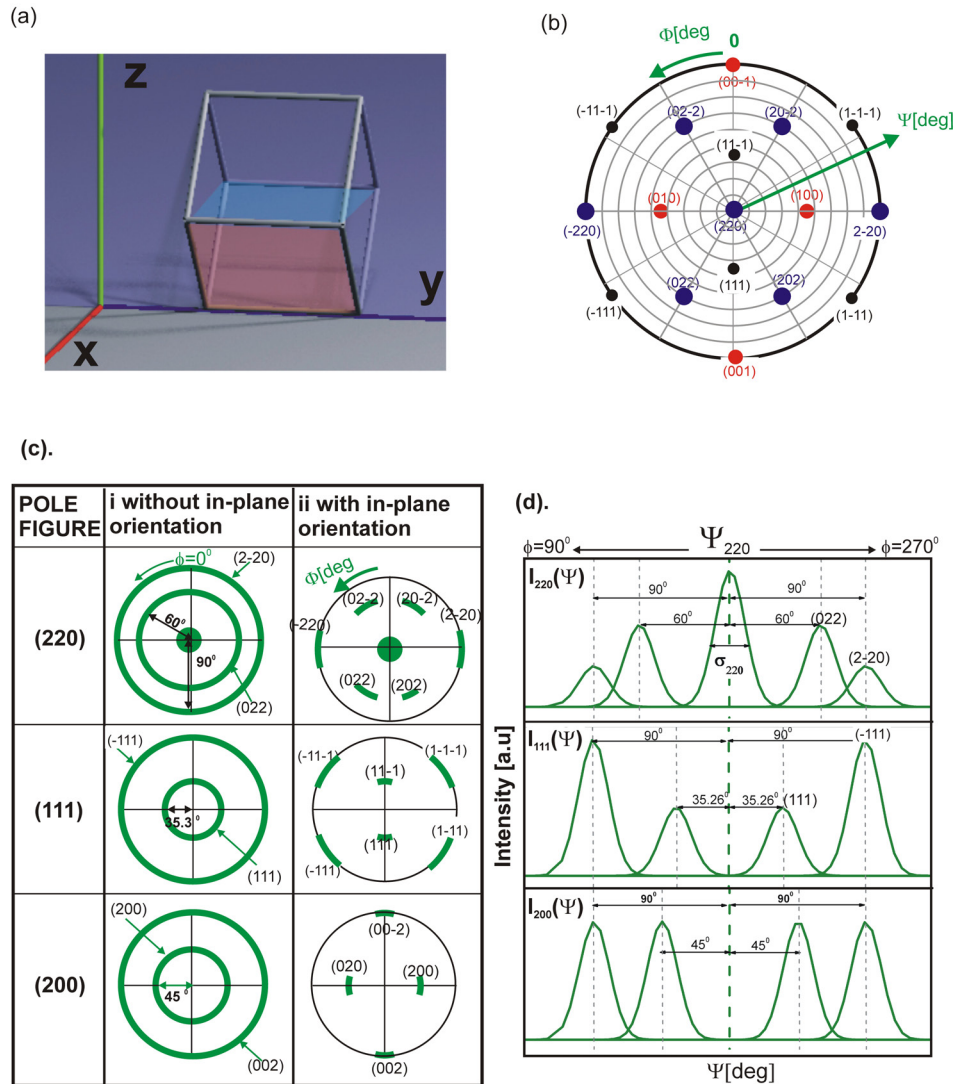


Figure 4.9: (a) A cubic unit cell with [220] orientation parallel to the surface normal, (b) orientation of different lattice planes relative to the (220) plane in polar coordinates, (c) schematic of the (220), (111) and (200) pole figures for different types of the (220) fiber textures, and (d) expected peak position for the (220) texture as a function of Ψ .

4.6 Correction Factors of the Measured Intensity

In the x-ray scattering experiment, the scattering intensity is measured. The intensity is proportional to the square of the scattering amplitude multiplied by a correction factor C:

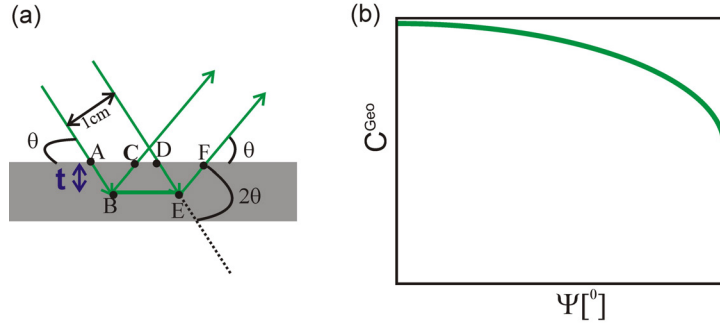


Figure 4.10: (a) X-Ray beam illuminates and penetrates the sample schematically and (b) typical correction for the illuminated scattering volume correction of pole figure geometry as a function of tilting angle Ψ .

$$I = C \cdot |F_{crystal}|^2 \quad (4.27)$$

In the following, we describe the correction factor due to the polarization of the incident beam, the absorption and the illuminated scattering volume.

In the synchrotron, the electrons are accelerated in the horizontal plane. Therefore, the emitted light is also polarized in the horizontal plane. Depending on the scattering plane relative to the direction of polarization of the incident beam, the polarization factor correction C^{pol} is equal to [49]:

$$C^{pol} = \left\{ \begin{array}{ll} 1 & \text{if the scattering plane is normal to the incident beam polarization} \\ \cos^2 \theta & \text{if the scattering plane is in the same plane as the incident beam polarization} \end{array} \right\} \quad (4.28)$$

Since all of our x-ray measurements are carried out in the perpendicular scattering plane relative to the incident beam polarization, our C^{pol} is equal to one.

Figure 4.10 (a) shows the incident x-ray beam with size 1×1 mm illuminates and penetrates the sample before it is diffracted by the crystalline plane at a given distance t from the surface. While traveling in the sample, some of the x-ray intensity is absorbed by the sample. The intensity correction due to the absorption depends on the absorption coefficient of the sample μ and the measurement geometry. One of our measurement geometries we use is the pole figure geometry (see Fig.6.1 (d) and (e)). The absorption correction factor (C^{Abs}) for pole figure measurements is: [55]

$$C^{Abs} = 1 - e^{(-2\mu t / \sin \theta \cos \Psi)} \quad (4.29)$$

where t is the sample thickness, θ is the scattering angle and Ψ is the tilting angle. For infinite sample thickness or a large absorption coefficient, C^{Abs} is equal to 1 so that this correction factor is more significant for thin or weakly absorbing samples.

The correction factor C^{Geo} is due to the illuminated scattering volume variation as a function of Ψ . It depends on the instrumental setup such as the width of detector slit. Some researchers determine the C^{Geo} experimentally by measuring the pole figure of powder reference. Typical correction factor for pole figure geometry is shown in Fig. 4.10 (b).

4.7 X-Ray Stress Analysis

The residual stress is built up during the coating formation due to several reasons including: (1) a mismatch between thermal coefficient of the substrate and the films, (2) crystallite growth process, and (3) the ion bombardment during sputter deposition [55, 56]. In our work, the residual stress of the coating is analyzed by x-ray diffraction.

There are two types of residual stress, i.e. compressive and tensile stress. Both types of residual stresses deform the crystalline lattice. The compressive stress contracts the lattice spacing d_{hkl} in the stress direction and expands the d_{hkl} in the orthogonal direction. The tensile stress deforms the unit cell in the reverse way compared to the compressive stress.

Figure 4.11 (a) shows the stress tensor components σ_{ij}^S of a rectangular shape body which is defined with respect to the surface in the sample coordinate system S . Because $\sigma_{ij}^S = \sigma_{ji}^S$, the stress tensor has only six independent components.

Strain ϵ_{ij} is a response of the body on the applied stress. The relation between strain and the applied stress is formulated in the Hooke's law. For isotropic material, the Hooke's law is [55]:

$$\epsilon_{ij} = \frac{1 + \nu}{E} \sigma_{ij} - \delta_{ij} \frac{\nu}{E} \sum \sigma_{kk} \quad (4.30)$$

where the Young's modulus E and the Poisson ratio ν are the elastic constants for an isotropic material. E measures the response of the body in the stress direction while ν measures the response of the body perpendicular to the stress direction.

In the following, we will describe the $\sin^2 \Psi$ method and the biaxial stress model which are commonly used to calculate the residual stress of thin coatings. This method is well suited for calculating the residual stress of the powder-like polycrystalline material which is assumed to be isotropic. However, we show later that the elastic constants E and ν can still be used to calculate the residual stress of a weakly texture material.

4.7.1 $\sin^2 \Psi$ Method

In the x-ray stress analysis, the strain is determined by measuring the position of a given Bragg reflection. The residual stress is then calculated by inserting the measured strain and the elastic constants of a given material into the strain-stress equation (see Eq. 4.30).

Figure 4.11 (b) illustrates the $\sin^2 \Psi$ method which we use to determine the strain of the coating. In this method, the lattice spacing d_{hkl} is measured as a function of Ψ at a given ϕ , i.e. in the $\mathbf{Q}_{\phi, \Psi}$ direction. The strain measured in the \mathbf{Q} direction is written as ϵ_{33}^M or $\epsilon_{\phi, \Psi}$.

The strain in the measured direction is related to the strain in the sample coordinate system ϵ_{ij}^S by:

$$\epsilon_{33}^M = \sum_{ij} a_{3i}^{MS} a_{3j}^{MS} \epsilon_{ij}^S \quad (4.31)$$

where a_{ij}^{MS} is the matrix which transforms the stress/strain tensor from the measured direction to the sample coordinate system S and has the form:

$$a_{ij}^{MS} = \begin{pmatrix} \cos \phi \cos \Psi & \sin \phi \cos \Psi & -\sin \Psi \\ -\sin \phi & \cos \phi & 0 \\ \cos \phi \sin \Psi & \sin \phi \sin \Psi & \cos \Psi \end{pmatrix} \quad (4.32)$$

By inserting this matrix transformation into the general strain-stress relation, Eq. 4.30 can be re-written as:

$$\begin{aligned} \epsilon_{\phi, \Psi} = & \left(\frac{1 + \nu}{E} \right) [(\sigma_{11}^S \cos^2 \phi + \sigma_{22}^S \sin^2 \phi + \sigma_{12}^S \sin 2\phi) \sin^2 \Psi \\ & + (\sigma_{13}^S \cos \phi + \sigma_{23}^S \sin \phi) \sin 2\Psi + \sigma_{33}^S \cos^2 \Psi] - \frac{\nu}{E} (\sigma_{11}^S + \sigma_{22}^S + \sigma_{33}^S) \end{aligned} \quad (4.33)$$

It will be shown in the next section that the strain-stress relation in Eq. 4.33 can be simplified by assuming the biaxial stress model.

4.7.2 Biaxial Stress Model

The residual stress of a thin coating often can be estimated by assuming a biaxial stress model. The assumptions of this model are:

- The residual stress has a rotational symmetry around surface normal, which means $\sigma_{11} = \sigma_{22} = \sigma_{||}$
- There is no force parallel to the film surface. With this assumption, the shear stress components vanish, i.e. $\sigma_{12} = \sigma_{21} = 0$
- The surface is free, i.e. $\sigma_{33} = 0$. As the thickness of the film is much smaller than the thickness of the substrate, the other stress components parallel to the surface normal are considered as zero as well, i.e. $\sigma_{13} = \sigma_{23} = 0$.

Thus the biaxial stress assumption reduces the stress components from six to two components, i.e. $\sigma_{11} = \sigma_{22} = \sigma_{||}$ where $\sigma_{||}$ is the in-plane residual stress.

If the assumptions of the biaxial stress model are valid, then the general strain-stress relation for an isotropic material becomes:

$$\epsilon_{\phi, \Psi} = \frac{1 + \nu}{E} \sigma_{||} \sin^2 \Psi - 2 \frac{\nu}{E} \sigma_{||} \quad (4.34)$$

In most cases, the hard coatings are textured and therefore the strain is anisotropic. For anisotropic materials, the isotropic elastic constants cannot be used. In the following, we show the approximation that we use to calculate the stress (analyze the strain) of a weakly textured material coating.

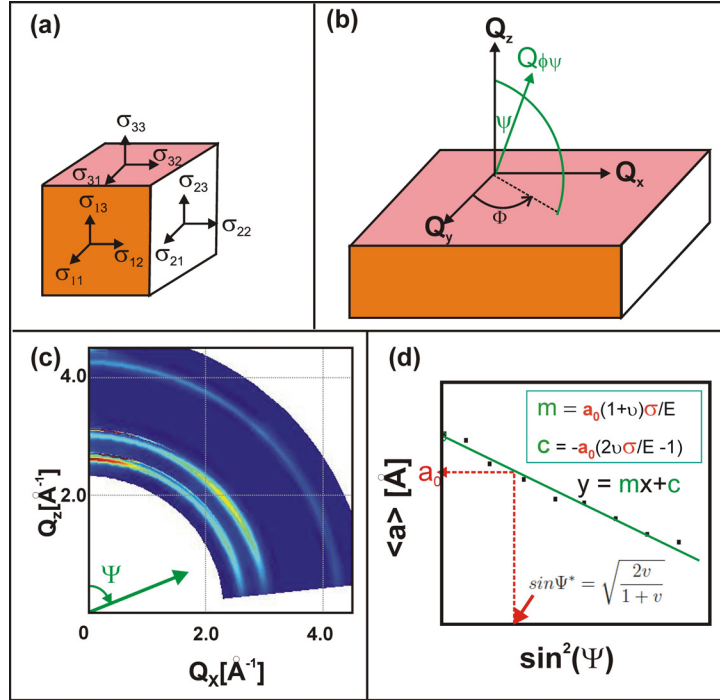


Figure 4.11: (a) Stress tensor, (b) illustration of the $\sin^2 \Psi$ method, (c) strain map, and (d) schematic of the $\langle a \rangle$ vs $\sin^2 \Psi$ plot.

4.7.3 Residual Stress of a Weakly Textured Coating

Figure 4.11 (c) shows an example of a strain map covering three (hkl) reflections. The intensity of all reflections is not homogeneously distributed along the powder ring which indicates texture. However, those reflections are still measurable within a broad Ψ range. This situation can be considered as a weak texture.

In the case of weak texture, the isotropic elastic constants E and ν are still a good approximation. In order to reduce the crystal anisotropy, $\epsilon_{\phi, \Psi}$ is then calculated from the normalized difference between the weighted average of lattice parameter $\langle a \rangle$ and the relaxed lattice parameter a_0 :

$$\epsilon_{\phi, \Psi} = \frac{\langle a \rangle - a_0}{a_0} \quad (4.35)$$

$\langle a \rangle$ is weighted by the multiplicity m_{hkl} as follows [55]:

$$\langle a \rangle (\Psi) = \frac{\sum_{hkl} m_{hkl} a_{hkl}(\Psi)}{\sum_{hkl} m_{hkl}} \quad (4.36)$$

where a_{hkl} is the lattice parameter calculated from d_{hkl} .

By substituting Eq. 4.35 into Eq. 4.34, we derive the linear relation between $\langle a \rangle$ and $\sin^2 \Psi$:

$$\langle a \rangle (\Psi) = a_0 \frac{1 + \nu}{E} \sigma_{\parallel} \sin^2 \Psi - 2a_0 \frac{\nu}{E} \sigma_{\parallel} + a_0 \quad (4.37)$$

The $\langle a \rangle$ vs $\sin^2 \Psi$ plot is schematically shown in Fig. 4.11 (d). The black dots represent measured data and the green line represents the linear fit. The gradient m and the axis intercept of this plot are:

$$m = a_0 \frac{1 + \nu}{E} \sigma_{\parallel} \quad (4.38)$$

$$c = a_0 \left(-\frac{2\nu}{E} \sigma_{\parallel} + 1 \right) \quad (4.39)$$

Ψ^* is the angle where $\epsilon_{\psi, \Phi} = 0$ and therefore $\langle a \rangle = a_0$. If ν is known, $\sin^2 \Psi^*$ can be calculated as:

$$\sin^2 \Psi^* = \frac{2\nu}{1 + \nu} \quad (4.40)$$

5 X-Ray Absorption Fine-Structure Spectroscopy

Microstructure analysis by x-ray diffraction has been described in chapter 4. A complementary x-ray techniques to analyze the microstructure is X-Ray Absorption Fine Structure Spectroscopy (XAFS). X-Ray Diffraction is a probe which is sensitive to the long-range crystal structure of the material while XAFS is a short-range order probe which is sensitive to the local environment of the material, and hence it can be used to study non-crystalline material as well.

In our work, we would like to investigate (1) the type of the neighbor atoms of Vanadium and (2) the atomic distance between the Vanadium and the neighboring atoms. For these purposes, we perform the XAFS experiments at Vanadium K-edge.

In this chapter, two regions of XAFS are described, i.e. X-Ray Absorption Near Edge Spectroscopy (XANES) and Extended X-Ray Absorption Fine-Structure Spectroscopy (EXAFS). For further reading on XAFS, the references [57] to [61] are proposed.

5.1 Introduction

The XAFS measures the change of the absorption coefficient as a function of energy E due to the interaction of the x-ray beam and the matter. The principle of XAFS is shown schematically in Fig. 5.1 (a). For both absorbing and neighboring atoms, electrons are represented by black dots while the nuclei are represented by white dots.

If the incident x-ray energy E is higher than binding energy E_B of a core level electron, the photon is absorbed and an electron is ejected from the atom (called photoelectron). The absorbing atom is now in an excited state with an empty core hole. Each atom has core-level electrons with their characteristic binding energy, therefore XAFS is an element sensitive probe.

The kinetic energy of the photoelectron E_{kin} is equal to the difference between incident x-ray energy E and the binding energy E_B :

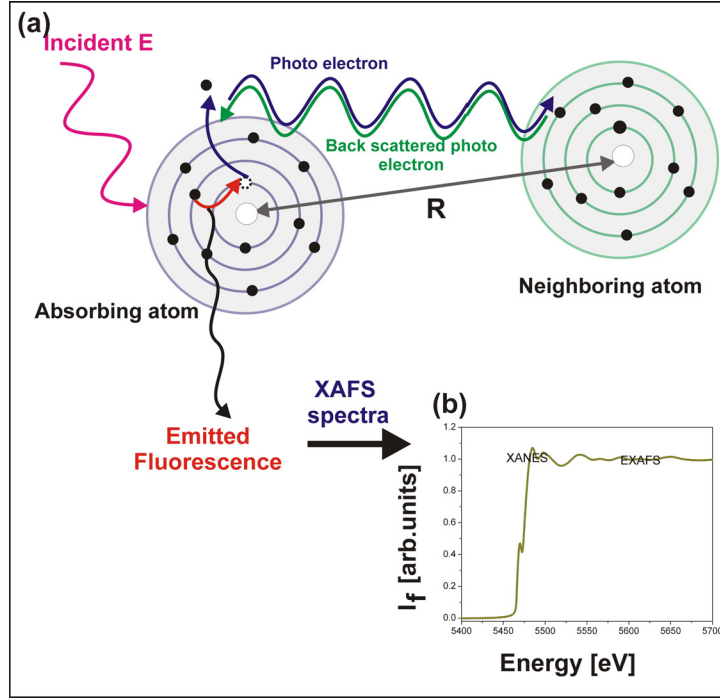


Figure 5.1: (a) Schematic of XAFS, (b) XANES and EXAFS regions of the XAFS spectra.

$$E_{kin} = E - E_B \quad (5.1)$$

The photoelectron might be backscattered by electrons of neighboring atoms and return to the absorbing atom. The interference between the outgoing photoelectron and the backscattered waves is the origin of the wiggles or oscillation in the XAFS spectra (see Fig. 5.1 (b)). In order to participate in XAFS, the backscattered photoelectron should return to the absorbing atom within the life time of the excitation state (typically in a few femto seconds [57]). Therefore, XAFS is sensitive to the neighbor atoms in a distance of typically 5-6 Angström from the absorbing atom.

One of the decay mechanisms is the fluorescence where the higher energy core-level electron fills the deeper core-level hole (red line in Fig. 5.1 (a)) and the atom emits a photon. In the XAFS, the fluorescence intensity I_f is recorded as a function of incident energy E close to the adsorption edge of the absorbing atom. The absorption edge is the sharp increase of the absorption coefficient at an x-ray energy equal to the binding energy of an electron shell.

Figure 5.1 (b) presents a XAFS spectrum, indicating both XANES and EXAFS regions.

XANES is the XAFS region up to about 40 eV from the absorption edge. EXAFS is the XAFS region above 40 eV from the absorption edge.

In fluorescence geometry, the absorption coefficient of absorbing atom μ_x influences the measured fluorescence intensity [62]:

$$\frac{I_f}{I_0} \propto \frac{A}{r^2} \epsilon_x \frac{\mu_x(E)}{\mu_{tot}(E) + \mu_{tot}(E_f) \frac{\sin\phi}{\sin\theta}} \left[1 - e^{(-\frac{\mu_{tot}(E)}{\sin\phi} + \frac{\mu_{tot}(E_f)}{\sin\theta})d} \right] \quad (5.2)$$

where I_f is the fluorescence intensity and I_0 is the incident intensity. A and r^2 are the area of the detector and the distance of the sample to the detector respectively. ϵ_x is the fluorescence yield of the absorbing atom while μ_x and μ_{tot} are the absorption coefficient of the absorbing atom and of all atoms in the samples. E and E_f are energy of the incident x-ray beam and energy at the fluorescence line. ϕ and θ are the angles of the incident beam and the detector relative to the sample surface. The relation between these angles in the standard measurement geometry is $\phi + \theta = 90^\circ$.

5.2 XANES at the Vanadium K edge

The distinguished features of the XANES spectra are the pre-edge peak, main edge and the region up to about 40 eV from the main edge. Figure 5.2 shows the XANES spectrum at Vanadium K-edge for different Vanadium compounds, i.e. (a) VC where the Vanadium has an octahedral symmetry and (b) V_2O_5 where the Vanadium has a distorted tetrahedral symmetry [58].

The pre-edge peak arises from the electronic transition of the core level electron to the vacant valence state [58, 61, 63, 64]. At Vanadium K-edge, the pre-edge peak is related to the $1s \rightarrow 3d$ electronic transition. This transition is dipole forbidden but quadrupole allowed for octahedral symmetry as in VC, and it is a dipole allowed if the octahedral symmetry is broken as in V_2O_5 . The pre-edge peak intensity for VC is weaker than for V_2O_5 because the transition is dipole forbidden in VC and it is dipole allowed in V_2O_5 .

The main edge arises from the transition of the electron at $1s$ level to the continuum. This edge is shifted to higher energy with increasing formal valence [58, 63]: (a) it is 9.9 eV for VC with formal valence +4 and (b) it is 15.1 eV for V_2O_5 which has formal valence +5. At an energy equal to or above the $1s \rightarrow 4p$ transition (20.4 eV for VC and 30.1 eV for V_2O_5 [58]), the features might also be influenced by the multiple scattering of the photoelectron. Therefore, this region is also sensitive to the interatomic distances and the bond lengths [63].

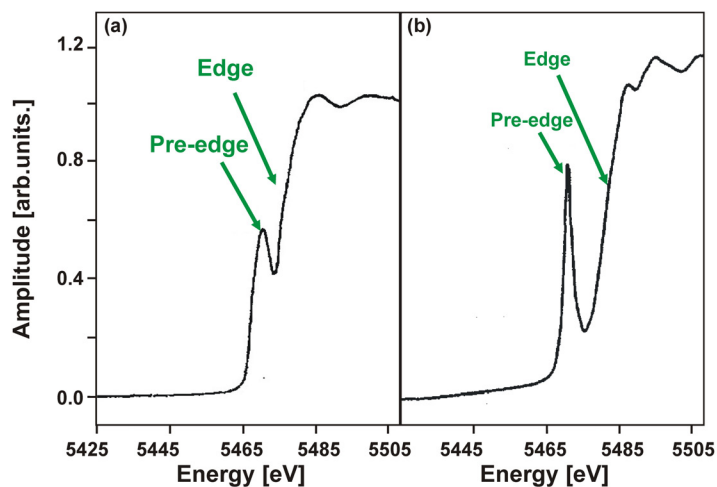


Figure 5.2: XANES spectra for (a) VC and (b) V_2O_5 as adapted from [58].

The position of the peak (energy shift) is influenced mainly by the valence electron and the electronegativity of the neighbor atoms. The intensity is influenced mainly by the coordination number and the symmetry around the absorbing atom.

Even though the atomic distance influences the features of the XANES region, the atomic distance is more accurately determined from the EXAFS region described in the next section.

5.3 Determination of the Atomic Distance

The atomic distance between the absorbing atom (in our case is Vanadium) and its neighboring atom is determined from the oscillation well above the absorption edge, i.e. in the EXAFS region. For the data analysis, the EXAFS intensity is presented as a function of the wave number k of the photoelectron with:

$$k = \sqrt{\frac{2m(E - E_B)}{\hbar^2}} \quad (5.3)$$

where $E - E_B$ is the difference between incident energy and binding energy of the core level electron, m is the electron mass and \hbar is the reduced Planck constant.

In the simplified EXAFS equation, $\chi(k)$ is proportional to the change of absorption co-

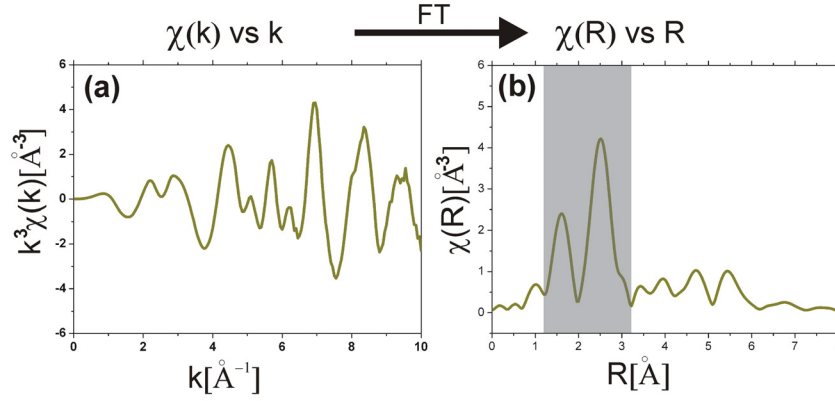


Figure 5.3: EXAFS spectrum as a function of (a) wavevector k and (b) atomic distance R .

efficient due to the back-scattered photoelectron:

$$\chi(k) = \sum_j \frac{N_j f_j(k) e^{-2k^2 \sigma_j^2} e^{-2R_j/\lambda(k)}}{k R_j^2} \sin[2kR_j + \delta_j(k)] \approx \Delta\mu \quad (5.4)$$

where $\Delta\mu$ is the background corrected absorption coefficient, i.e. the difference between the measured absorption coefficient and the absorption coefficient of an isolated atom (see reference [57] for extracting $\Delta\mu$ from the measured spectra), N_j is the number of neighbor atoms j , R_j is the atomic distance between absorbing atom and atom j and σ_j is a measure for the atomic distance distribution. δ_j is a phase shift, i.e. a correction of the atomic distance R_j because the photoelectron is backscattered by the electrons and not by the nucleus of neighboring atoms. f_j is the scattering amplitude of the atom j , $\lambda(k)$ is the mean free path of the photoelectron.

Figure 5.3 (a) shows an example of the measured spectrum on our V-Al-C-N coatings. $k^3\chi(k)$ is presented as a function of k (the weighting factor k^3 enhances the oscillation). In order to calculate the atomic distance, $\chi(k)$ is Fourier transformed into $\chi(R)$. The Fourier transformation of $\chi(k)$ to R space is presented in Fig. 5.2 (b) without phase-shift correction.

Figure 5.2 (b) shows two peaks (see gray shaded area) which can be used to determine the atomic distance between Vanadium and the neighboring atoms. Out of this gray region, the noise has a significant contribution to the observed peaks.

6 Experimental details of the X-Ray Measurement

In order to investigate the microstructure of the coatings, two main characterization methods were used, which are X-Ray Diffraction (XRD) and X-Ray Absorption Fine Structure Spectroscopy (XAFS). All the data presented in this thesis were measured at the synchrotron facility Angströmquelle Karlsruhe (ANKA), located at Karlsruhe, Germany. Prior to the pole figure measurements at ANKA, we performed test experiments (the data are not presented here) at the Leibniz Institut für Innovative Mikroelektronik (Frankfurt Oder) using an x-ray laboratory source with the help of Dr. Peter Zaumseil.

The measurement details such as geometries and measurement ranges are described in the following.

6.1 Geometries and Measurement Range of the XRD Experiments

All x-ray diffraction experiments were performed at the PDiff beamline of ANKA at the x-ray energy 9.5 keV. Figure 6.1 (a) shows the Kappa diffractometer which was used for all measurements. The incident beam, the diffracted beam, the sample stage and the detector arm are indicated in the figure. The scattering intensity was recorded by a point detector with an analyzer for better energy resolution and background reduction. Three measurement types were used, i.e. radial scan, strain map and pole figure.

Figure 6.1 (b), (d) and (f) illustrate the sample (green rectangle) and detector movements for radial scan, strain map and pole figure geometries respectively. (X,Y,Z) is the laboratory coordinate system where the Y axis is pointed out of the paper plane and the X axis is parallel to the incident beam direction. The scattering vectors Q_x and Q_y are parallel to the sample surface, and Q_z is parallel to the surface normal.

The blue solid line indicates the x-ray beam where α_i is the angle between the incident beam and the sample surface and α_f is the angle between the diffracted beam and the sample surface. 2θ is the detector angle. ω is the sample rotation angle around the Y axis. Ψ and ϕ are rotation angles which are defined with respect to the surface normal.

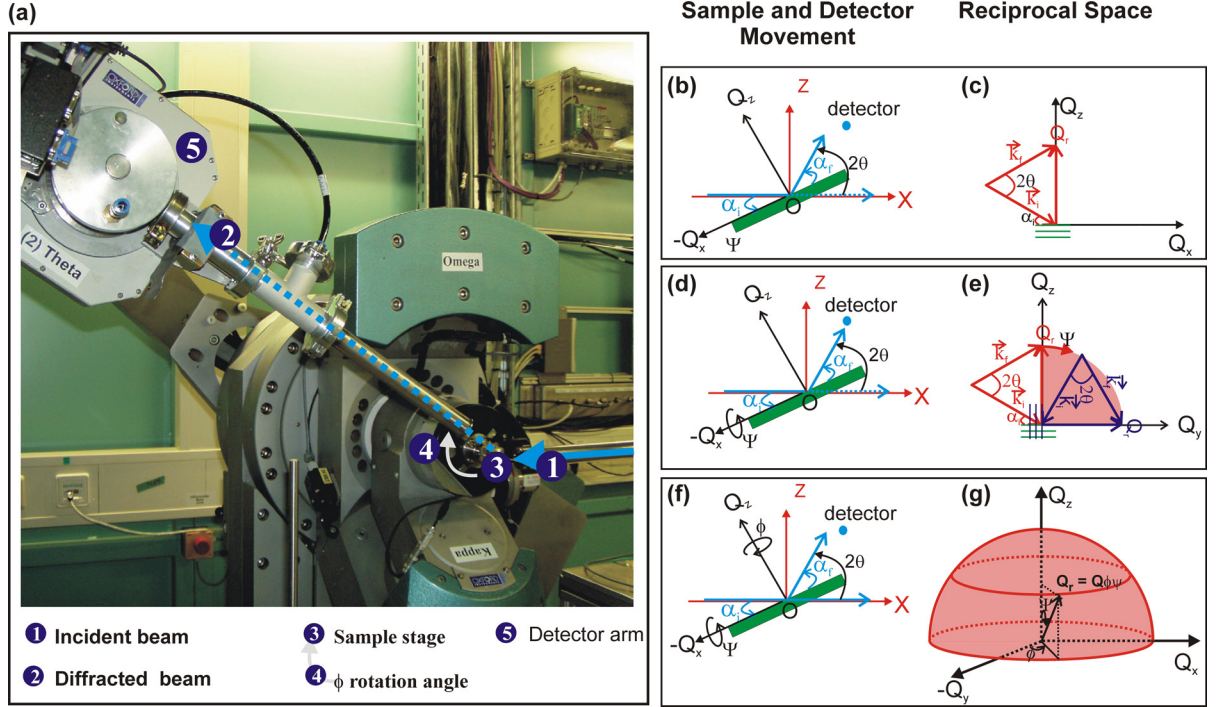


Figure 6.1: (a) Experimental station of the PDiff beamline. Sample and detector movement for (b) the radial scan, (d) the strain map, (e) the pole figure. Reciprocal space for (c) the radial scan, (e) the strain map, and (f) the pole figure.

Figure 6.1 (c), (e), and (g) show the reciprocal space for the radial scan, the strain map and the pole figure geometry. Red lines in Fig. 6.1 (c) and (e) indicate the incident and the scattered wave vectors and the momentum transfer Q in reciprocal space for radial scan and strain map measurements. The green solid lines indicate the lattice planes which are orthogonal to Q_z .

The radial scan measures the diffracted intensity in a given Q_r direction where the sample and the detector move in such a way that $\Delta\omega/\Delta 2\theta = 1/2$. A particular case of a radial scan is the specular or Q_z scan where $\Psi = 0^\circ$ and $\omega = 2\theta/2$. Figure 6.1 (c) shows schematically the reciprocal space representation of a Q_z scan.

The strain map was obtained by measuring a set of radial scans at different tilt angles Ψ . The measurement in reciprocal space is shown in Fig. 6.1 (e). The red background represents the area in reciprocal space which is covered by the strain map. It is shown schematically that at $\Psi = 0^\circ$ (red lines), the radial scan measures the Bragg reflection of the lattice planes which are parallel to surface normal. At $\Psi = 90^\circ$ (blue lines), the scan

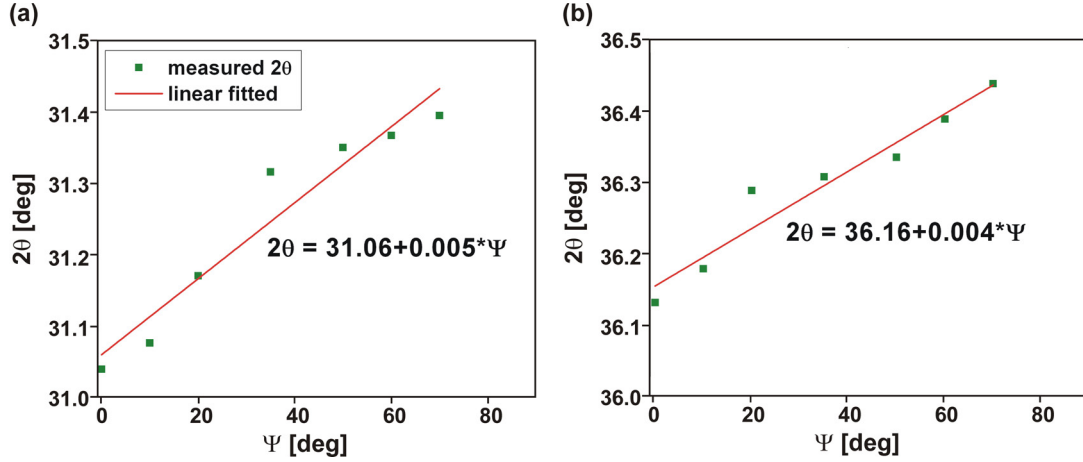


Figure 6.2: The pre-determined scattering angle θ for a sample on cemented carbide at $X = -6$ mm of (a) (111) and (b) (200) reflections.

measures the Bragg reflection of the lattice planes which are orthogonal to surface normal.

The intensity distribution of a given Bragg reflection in all accessible directions above the sample surface is measured by the pole figure. In the pole figure geometry, the sample is rotated in the angular range $0^\circ < \phi < 360^\circ$ and $0^\circ < \Psi < 90^\circ$. The red background represents the region in reciprocal space which is covered by the pole figure measurement (see Fig. 6.1 (g)). The measured intensity is then presented in polar coordinates.

Prior to the pole figure scans, we measured the peak positions of the (111) and the (200) reflections. Figure 6.2 shows the measured peak positions (presented as 2θ) as a function of Ψ for (a) the (111) and (b) the (200) reflections of the coating on cemented carbide at $X = -6$ mm. It was observed that the peak positions increase with increasing Ψ . The linearly fitted $2\theta(\Psi)$ is indicated in the figure. Because the peak is broad (FWHM_{111} at $\Psi = 0^\circ$ is 0.25° and 1° at $\Psi = 70^\circ$), all fitted points at given Ψ are still located close the maximum of the Bragg peaks. Thus the measured intensity does not vary significantly for small 2θ offset relative to the actual peak position. The same tendency was found for all others samples (the 2θ vs Ψ plot is not given here). The pole figures were performed at 2θ which follows the linear fit.

The measurement ranges used for the XRD experiments presented in this manuscript are summarized in table 6.1. The radial scan was measured at Ψ_{111} and ϕ_{111} corresponding to the maximum intensity of the (111) texture as determined from the (111) pole figure. The radial scan covers the first six coating reflections which are necessary to determined the crystal structure of the samples. The strain map covers the first three strongest reflections. They are used to analyze the texture and determine the residual stress. Both

Table 6.1: Measurement range of the radial scan, strain map and pole figure.

Geometry	2θ [deg]	Ψ [deg]	ϕ [deg]
Radial Scan	$25 < 2\theta < 80$	Ψ_{111}	ϕ_{111}
Strain Map	$25 < 2\theta < 60$	$0 < \Psi < 72$	ϕ_{111}
Pole Figure	(111) & (200) reflections	$0 < \Psi < 72$	$0 < \phi < 360$

pole figure and strain map were not measured for $\Psi > 72^\circ$ because of the low intensity.

6.2 X-Ray Absorption Fine Structure Spectroscopy

The X-Ray Absorption Fine Structure Spectroscopy (XAFS) and X-Ray Fluorescence measurements (see next section) were performed at the XAS beamline shown in Fig. 6.3 (a). The XAFS measurements were performed in the fluorescence geometry because the sample is thick (coating plus substrate are in the mm range) so that the measurement in the transmission geometry is not possible. The beam direction in fluorescence geometry is presented schematically in Fig. 6.3 (c). The green dashed line represents the fluorescence intensity which was measured at 90° with respect to the incident beam using a five-element Ge detector. The ionization chambers (number 2) are used for transmission geometry. The sample wheel in Fig. 6.3 (b) can hold up twelve samples simultaneously.

The EXAFS scans in the range of $5315 \text{ eV} < E < 6445 \text{ eV}$ were measured for selected coating. This range covers the pre-edge and the EXAFS region of the Vanadium K edge (at 5465 eV). The acquisition time was 75 ms and the energy resolution was approximately 1 eV.

The data were analyzed by Dr. Stefan Mangold of the XAS beamline and Dr. Baerbel Krause using the Artemis software which use the IFEFFIT library [65]. The result is summarized in chapter 10.

6.3 X-Ray Fluorescence

Another x-ray measurement which we performed was the X-Ray Fluorescence where the samples were irradiated by x-rays with an incident energy of 5800 eV , and the fluorescence intensity at 4953 eV was recorded. This line corresponds to the Vanadium $K_{\alpha 1}$ line. The fluorescence intensity is influenced by the chemical composition and the thickness (see Eq. 5.2).

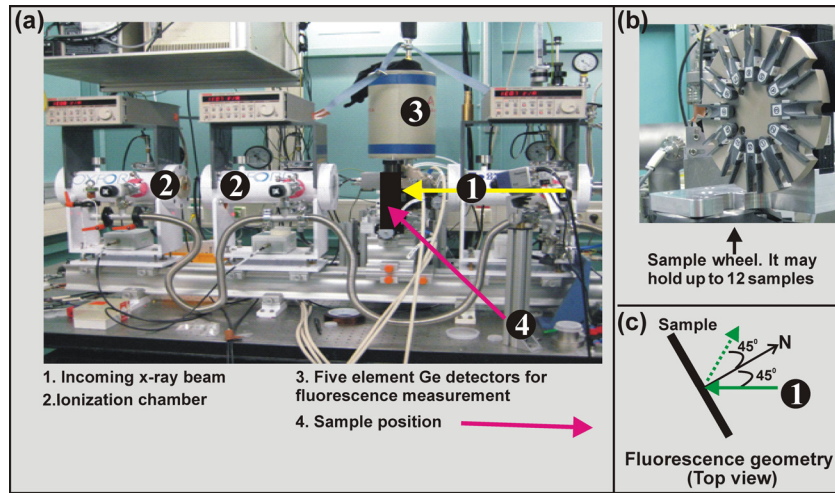


Figure 6.3: (a) Experimental station of XAS beamline, (b) sample rotation stage, and (c) schematic of the fluorescence geometry.

The sample holder with two x-y translation motors allow us to map the fluorescence intensity at different sample positions. In our experiment, the beam size was 1 X 1 mm and the scan step was 1 mm in both x-y directions. As for the XAFS measurements, the fluorescence intensity was measured at 90° with respect to the incident beam using a five-element Ge detector.

7 Pre-Characterization of V-Al-C-N Hard Coating on Cemented Carbide and Si

The work reported in this thesis is a result of collaboration between the Institut für Synchrotron Strahlung (ISS) and the Institut für Angewandte Materialien - Angewandte Werkstoffphysik (IAM-AWP) of the Karlsruher Institut für Technologie (KIT). Two series of V-Al-C-N coatings, i.e. on cemented carbide and on Si(001) were deposited by researchers at IAM-AWP. They also performed elemental analysis as well as the thickness and the hardness determination. The microstructure analysis of the samples using XRD and XAFS methods were performed by ISS.

In this chapter, the deposition parameters, the chemical composition, the thickness of the coatings, the fluorescence intensity maps as well as coating morphology are summarized.

7.1 Deposition Parameters

V-Al-C-N coatings were deposited by radio frequency magnetron sputtering without substrate bias. A segmented circular target composed of half a VC and half an AlN target was used. The diameter of the target was 75 mm. The substrates were ultrasonically cleaned in acetone and isopropanol for 15 minutes. The background pressure in the deposition chamber was around 3.10^{-6} mbar.

Figure 7.1 shows schematically the projection of the substrates on the target for the

Table 7.1: Deposition parameters of the coatings on cemented carbide and on Si.

Parameters	on cemented carbide	on Si
Power [W]	250	250
substrate-target distance [mm]	60	50
Working Pressure [Pa]	0.6	0.55
Ar flow [sccm]	60	60
CH ₄ flow [sccm]	1.5	1.5
Deposition time [min]	240	75
Substrate temperature [°]	150	150

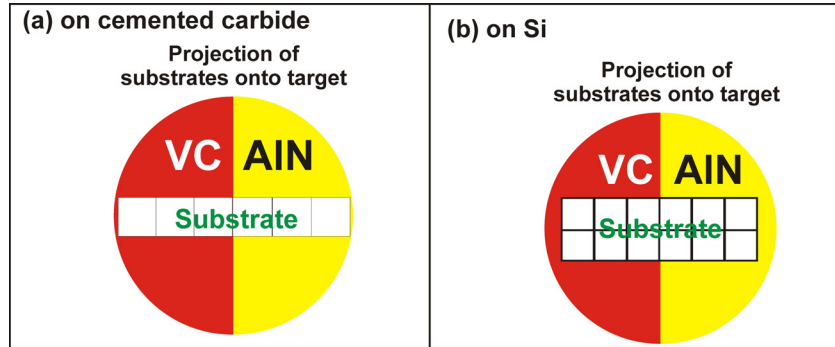


Figure 7.1: Bottom view projection of the substrates on the target for: (a) the coatings on cemented carbide and (b) on Si.

coatings on (a) cemented carbide and (b) Si(001)substrate.

Two types of substrates were used, which are cemented carbide (size 12 mm x 12 mm x 45 mm) and Si(001) (size 10 mm x 10 mm x 0.5 mm). For each type, a series of substrates was coated simultaneously with deposition parameters as listed in table 7.1.

The chemical composition, the thickness, and the morphology of the coatings on cemented carbide are described in the following.

7.2 Chemical Composition and Thickness as a Function of Position

The chemical composition of the coatings was measured by Electron Probe Micro Analysis (EPMA) [66] and the thickness was determined using a calo tester. The chemical composition in atomic percent at. % and the thickness t in μm as a function of position are shown in Fig. 7.2 (a) for coatings on cemented carbide.

The chemical composition is influenced by the sputtering yield of VC and AlN as well as by the deposition geometry. It is found that independent of position, the Vanadium and Carbon concentrations are higher than the Aluminum and Nitrogen concentrations. This indicates that the sputtering yield of VC, Y_{VC} , is bigger than sputtering yield of AlN, Y_{AlN} . At $X = 0$, the concentration is not influenced by the deposition geometry. It is found that at this position, $Y_{VC} \approx 3Y_{AlN}$.

The thickness of the coating as a function of position is represented by green stars. The

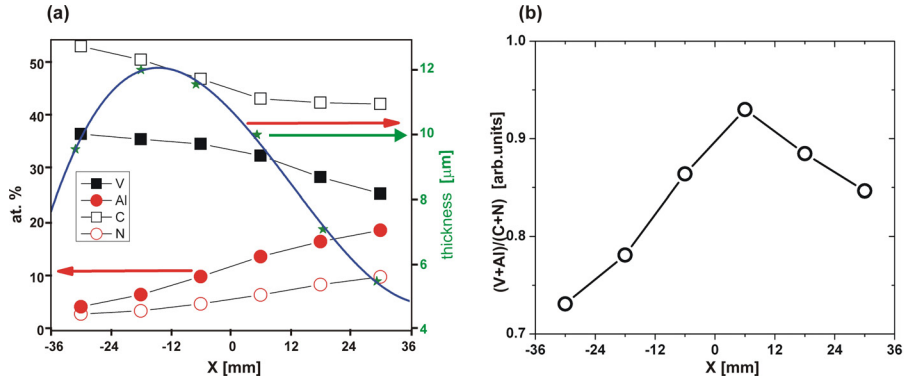


Figure 7.2: (a) Chemical composition and thickness, and (b) $(V+Al)/(C+N)$ ratio of the coatings on cemented carbide as a function of X.

blue line is the polynomial fit of the thickness profile. The maximum thickness is found for coating below the VC target. This is expected because the sputtering yield of VC is bigger than the sputtering yield of AlN.

Figure 7.2 (b) shows the $(V+Al)/(C+N)$ ratio of the coatings. It is described in section 2.2 that the expected metastable phase is a mixed crystal either in hexagonal or fcc structure consisting of Vanadium, Aluminum, Carbon and Nitrogen. The $(V+Al)/(C+N)$ ratio is 1 for stoichiometric fcc or hcp. The $(V+Al)/(C+N)$ ratio of all coatings is smaller than one. This indicates that (Carbon + Nitrogen) is in excess. The carbon in excess is desired for reducing the friction coefficient.

The chemical composition and thickness of the coating on Si were not determined. Since the deposition parameter are similar except for the deposition time, the chemical composition variation of the coatings on Si is expected to be similar to the coatings on cemented carbide. Assuming a linear deposition rate as a function of time, the thickness of the coating on Si is expected to be a third of the thickness of the coating on cemented carbide.

7.3 Fluorescence Intensity Map

The fluorescence intensity maps of the coatings on cemented carbide and on Si were performed by measuring the fluorescence intensity I_f at 4953 eV which corresponds to the Vanadium $K_{\alpha 1}$ line. The measured fluorescence intensity I_f depends on the thickness, chemical composition and the absorption coefficient of the coatings as given in Eq. 5.2.

The fluorescence intensity maps (FIM) of both series of coatings are presented in Fig. 7.3

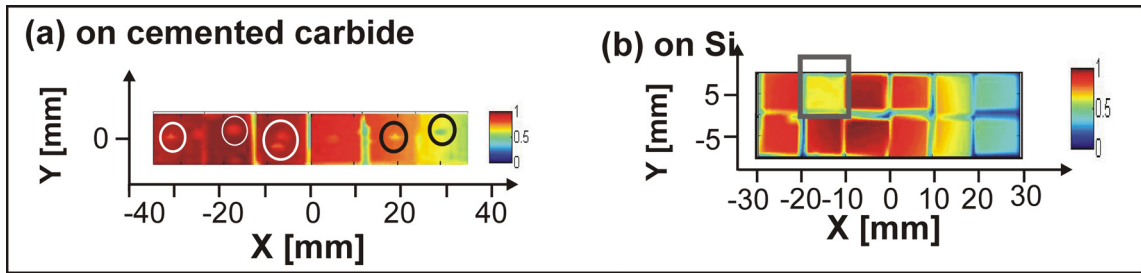


Figure 7.3: Fluorescence intensity map of the coatings on: (a) cemented carbide and (b) Si.

(a) and (b). The edges of the individual samples are visible. The fluorescence intensity of the coatings on cemented carbide was measured after the scratch test and the use of calo tester (for thickness measurement). Those tests removed some of the coating from the surface which decreases the thickness at these positions. The white and black circles in Fig. 7.2 (a) indicates the location of damaged parts of the coating.

The FIM is influenced by the Vanadium concentration and the coating thickness. In order to transform the FIM to the Vanadium concentration map, the concentration of other elements, i.e. C, Al, N and the thickness should be known accurately along the coating position X. Because our measured data points are not sufficient, the Vanadium concentration from the fluorescence intensity map cannot be determined more accurately than the EPMA results. However, the maps show qualitatively the chemical composition and thickness gradient as a function of X and help to verify the orientation of the substrates during deposition. This information is important for us to analyze the influence of the deposition geometry on the microstructure.

Independent of the substrate type, the maximum fluorescence intensity is found for coatings below the VC target, i.e. for $-20 \text{ mm} < X < 0 \text{ mm}$. This is expected because as it is shown by EMPA and the thickness measurement, the coating at this position has the highest Vanadium concentration and the largest thickness.

The fluorescence intensity of the first ($Y = 5 \text{ mm}$) and second row samples ($Y = -5 \text{ mm}$) on Si is symmetric, except for the sample at $(X, Y) = (-15, 5)$. The similar fluorescence intensity is expected because the deposition geometry of the first and the second row coatings is symmetric with X axis as a mirror axis. The abrupt change of the fluorescence intensity at $(X, Y) = (-15, 5)$ indicates that this coating was not at the intended position during the deposition.

7.4 Coating Morphology

The Scanning Electron Microscopy (SEM) images of the coatings on cemented carbide were taken at the edge of scratches. The images for selected positions (indicated in the figure) are shown in Fig. 7.4 (a) and (b). The images show the surface and the cross section of the coatings. The cross section shown in Fig. 7.4 (b) indicates the fiber texture with the height of the crystallites smaller than the coating thickness. The black circle in Fig. 7.4 (a) indicates that the surface has holes.

The Atomic Force Microscope (AFM) images of coatings on cemented carbide at selected positions are shown in Fig. 7.4 (c) and (d). The black circles indicates the surface with gaps/holes. This is consistent with the observation of the SEM image at $X = -6$ mm. The holes at surface allow us to see the wall of the hole where the crystallites seems to be elongated in vertical direction. This might indicate a fiber texture.

The surface roughness as measured by the AFM is presented in Fig. 7.4 (e). It is shown that the roughness of the coatings is in the nm range.

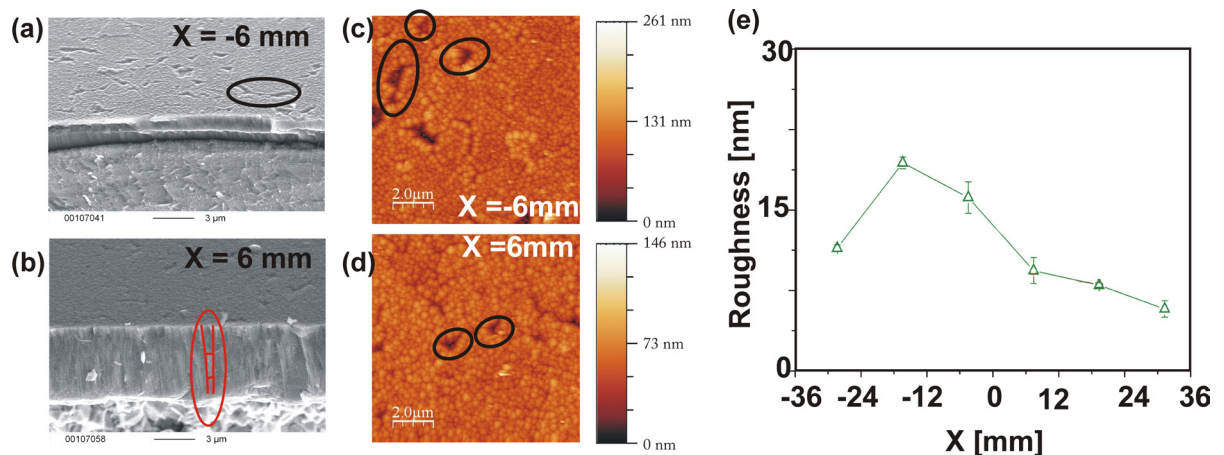


Figure 7.4: (a) and (b): SEM images, (c) and (d): AFM images of coatings on cemented carbide at selected positions, and (e) the roughness measured by AFM.

8 X-Ray Diffraction Results of (V,Al)(C,N) Thin Films on Cemented Carbide

The microstructure of a series of hard thin (V,Al)(C,N) coatings on cemented carbide was investigated by X-Ray Diffraction (XRD). The results are presented in this chapter in three sections.

Section 8.1 presents the radial scans for selected positions. Crystal structure and lattice spacing of the coatings are then determined from the peak positions. The influence of the size and the strain distribution on the Full Width Half Maximum (FWHM) is discussed.

Pole figure and strain map of selected position were measured in order to investigate texture of the coatings. The type of textures, the average orientation and the orientation distribution width of each type of texture are determined. This texture analysis is presented in section 8.2.

The influence of the texture superposition on the lattice spacing as a function of Ψ is discussed in section 8.3. The results of this chapter will be used to determine the lattice parameter and the residual stress of the coatings which are given in chapter 11. The interplay of micro structure of the coatings and hardness will be discussed in chapter 12.

8.1 Analysis of the Radial Scans

In this section, radial scans measured at selected positions (X) are presented. X is the position of the sample below the target during deposition. The radial scan is measured in the direction of the average orientation of the (111) texture (see section 8.2 for a detailed texture analysis), which is almost in specular direction for all positions. The coating reflections are identified. Their peak position and FWHM are analyzed.

8.1.1 Substrate Reference

At the used x-ray energy, the penetration depth is larger than the coating thickness. Thus the radial scans of the samples consist of a superposition between the scattering

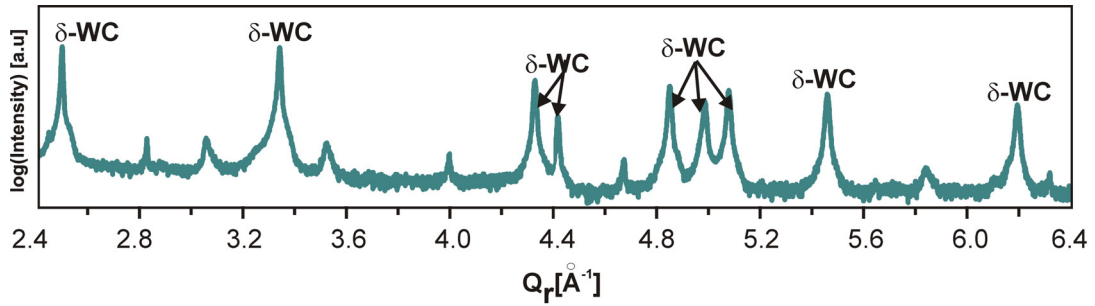


Figure 8.1: Diffraction profile of cemented carbide.

of the coating and the substrate. In order to identify the substrate reflections, a radial scan of a substrate without coating was measured. Figure 8.1 shows the radial scan of a cemented carbide substrate. The intensity is plotted in a logarithmic scale as a function of the scattering vector Q_r .

Two types of substrate reflections are observed, i.e. strong and weak reflections. The cemented carbide substrate is composed of 95% WC (tungsten carbide) and cobalt as a binder. Kurlov et al. [67], reported several stable phases of WC such as δ -WC, β -WC and γ -WC. The strong reflections in figure 8.1 are attributed to the δ -WC phase, i.e. a hexagonal phase with $a = 2.906 \text{ \AA}$ and $c = 2.837 \text{ \AA}$. The weaker reflections cannot be attributed to one crystalline phase only. They might be related to a mixture of Co, other WC phases or alloys.

8.1.2 Coating Reflections

Figure 8.2 shows radial scans measured for sample position in the range $-30 \text{ mm} < X < 30 \text{ mm}$. The intensity is plotted in logarithmic scale.

Two types of reflections are observed, i.e. narrow and broad reflections. The peak positions of the narrow reflections are identical to the peak positions of the substrate reference (see 8.1.1). Therefore the narrow reflections are attributed to the substrate reflections. The remaining broader peaks are attributed to the coating. In Fig. 8.2, the coating reflections are indicated by shaded gray areas and labeled as A, B, C, D, E and F. Independent of the position, A is the strongest and F is the weakest reflection.

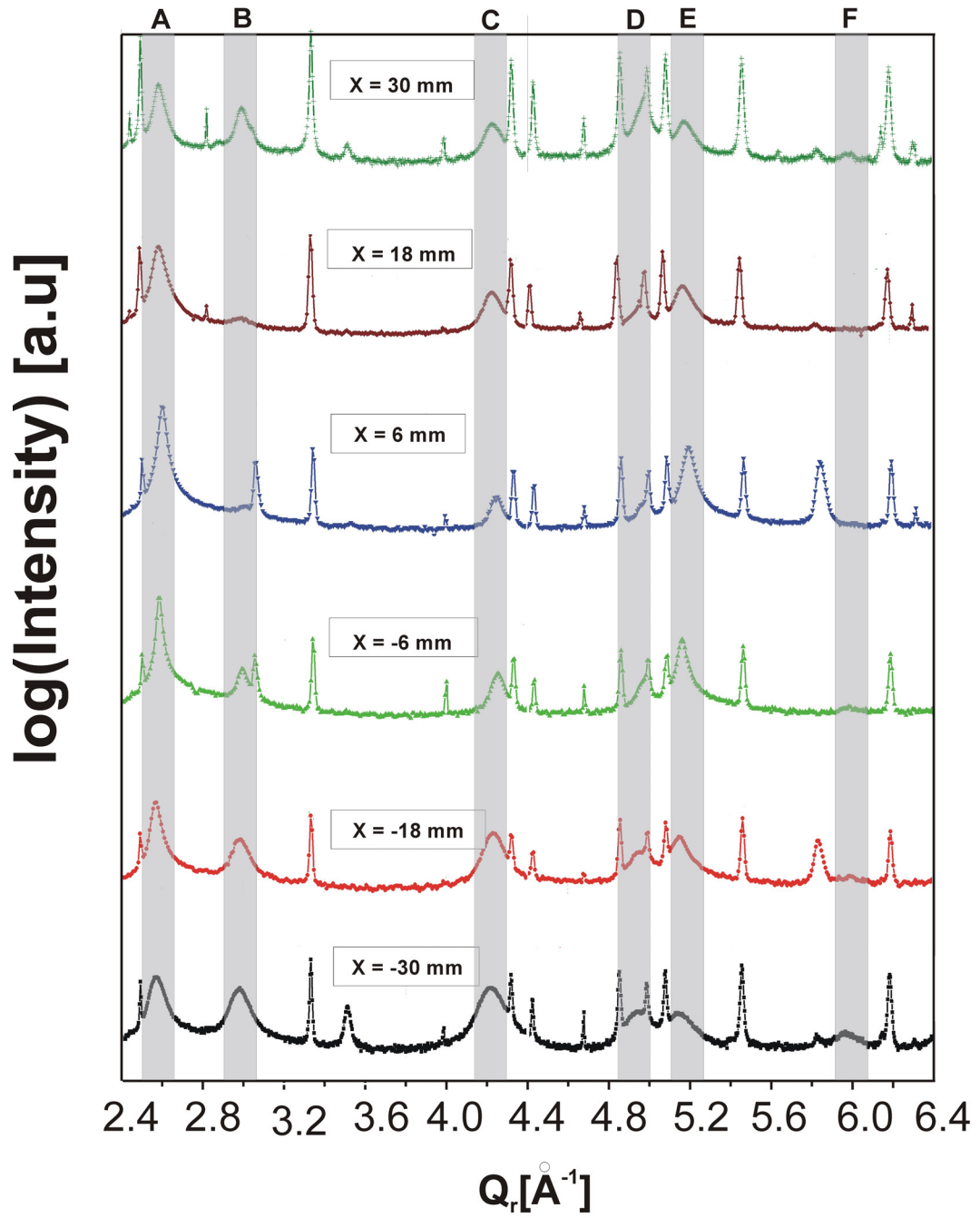


Figure 8.2: Radial scans measured at selected positions.

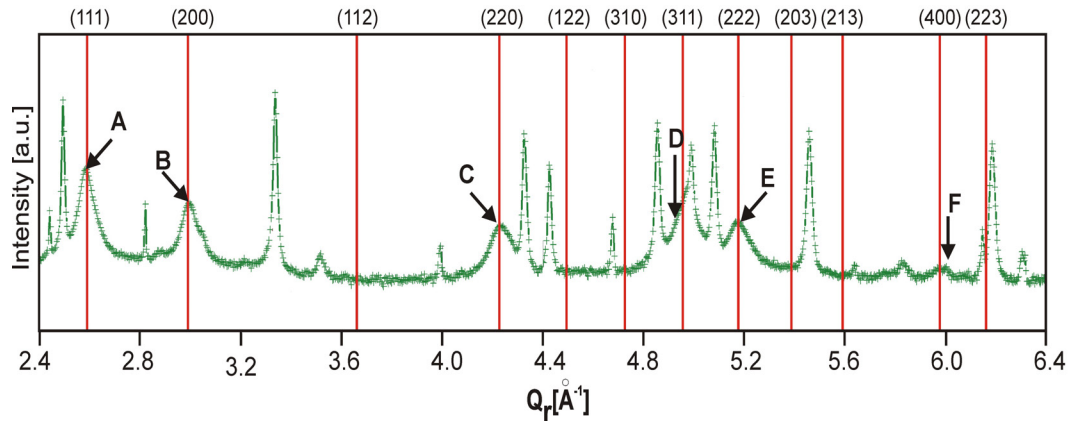


Figure 8.3: Radial scan for $X = 30$ mm and calculated peak position of a cubic unit cell with $a = 4.2$ Å.

The peak positions of the coatings are related to their crystal structure. Each crystal structure has a set of characteristic peak positions. The typical crystal structure of metallic hard coatings is cubic.

Figure 8.3 shows the radial scan at $X = 30$ mm. The red lines are calculated peak positions of a cubic unit cell for $a = 4.2$ Å. The Miller indices of these peaks are indicated on top of the figure.

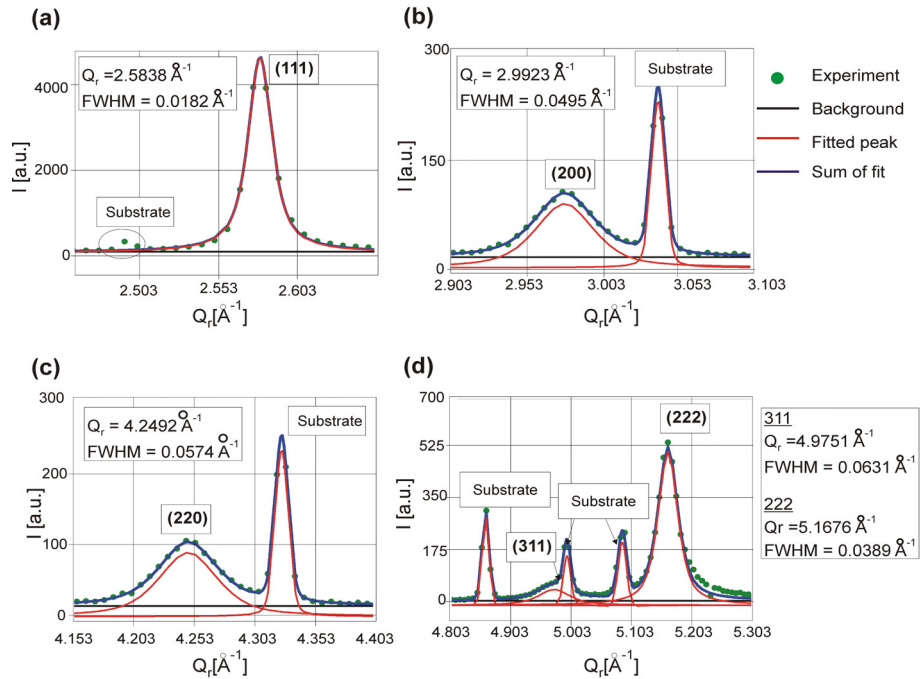
All coating reflections (A to F) can be attributed to reflections of the cubic unit cell with all odd or all even Miller indices, i.e. (111), (200), (220), (311), (220) and (400) respectively. Those reflections are the allowed reflections of the face centered cubic (fcc) lattice.

Independent of X , all measurements show the same reflections. Therefore it is concluded that independent of position, the crystal structure of all coatings is fcc.

8.1.3 Whole Pattern Fitting Method

For further data analysis, the whole pattern fitting method (WPFM) was performed using the Fityk software [68]. The coating and substrate reflections were fitted by a pseudo Voigt peak shape, and the background is assumed to be linear. Figure 8.4 shows the fitting result of the radial scan at $X = -6$ mm. The intensity is plotted in linear scale. The fitted peak position and the FWHM of the coating reflections are indicated.

The superposition of the coating and the substrate reflections influences the fitting error of the peak position and the FWHM. The fitting error is larger for stronger overlapping


 Figure 8.4: The Whole Pattern Fitting Method (WPFM) for $X = -6$ mm.

of neighboring peaks. Figure 8.4 (a) shows that the (111) reflection is well separated from the nearest substrate reflection. The substrate reflections are superimposed with tails of the (200), the (220) and the (222) coating reflections. The overlapping between the substrate reflections and those reflections are weak so that the fitting errors are still small. Figure 8.4 (d) shows the (311) reflection is overlapping with a substrate reflection close to the (311) peak position. This strong superposition leads to larger fitting errors than for all other reflections.

The results of the fits are summarized in Fig. 8.5 and 8.6. The fitted peaks are used to calculate the lattice spacings and their error bars.

8.1.4 Lattice Spacing

The peak positions of all reflections for all coatings have been fitted by Fityk software. Using the Bragg equation (see section 4), the lattice spacing of all reflections is calculated from the fitted peak position.

Figure 8.5 shows the lattice spacing of all measured reflections in Angström as a function of position. The error bar and the direction of decreasing V concentration are indicated.

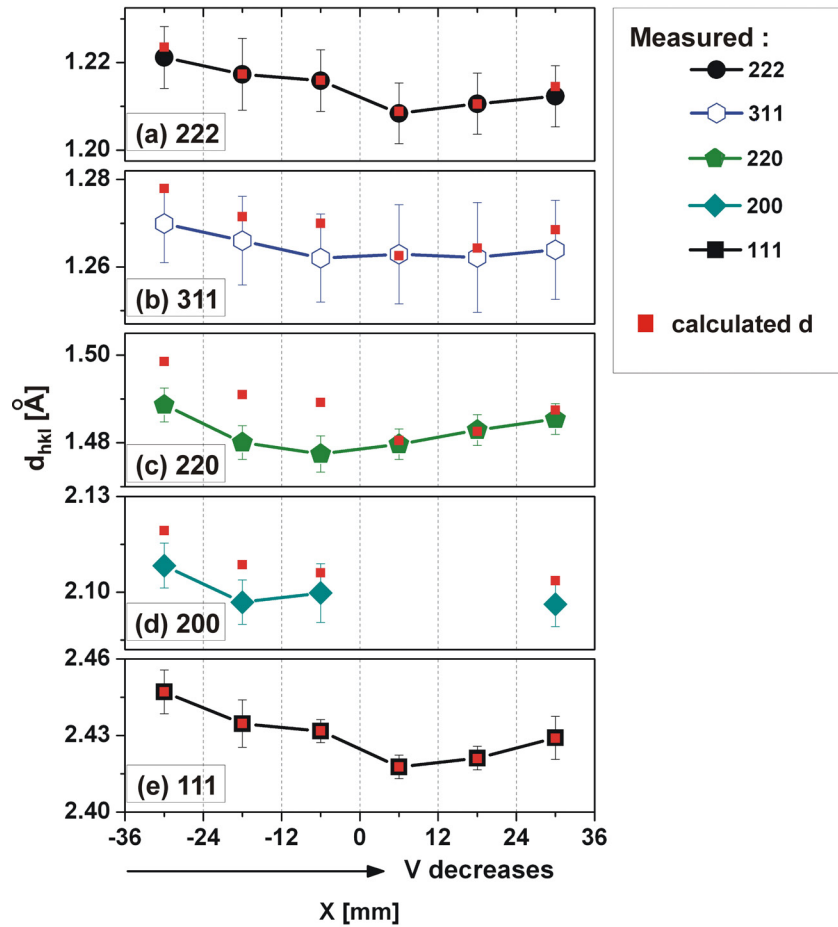


Figure 8.5: Measured and calculated lattice spacing d_{hkl} as a function of X shown for different reflections.

The peak positions of the (200) reflection for X = 6 and 18 mm could not be fitted reliably because these reflections are very weak and broad.

As a function of position, d_{hkl} of all reflections shows a parabolic shape. Except for the (200) reflection, d_{hkl} has a minimum in the range of $-10 \text{ mm} < X < 10 \text{ mm}$. These positions correspond to the position approximately below the center of the target during deposition.

Assuming a homogeneous and relaxed mixed crystal, a monotonous decrease of lattice spacing is expected for decreasing Vanadium concentration, i.e. for our coatings in the direction of increasing X. This has not been observed, indicating that the lattice spacing is not only influenced by the chemical composition, but also by the microstructure.

In order to analyze the behavior of different (hkl) reflections, the d_{hkl} are calculated assuming a cubic, unstrained unit cell parameter with $a = a_{111}$ as shown as red squares in Fig. 8.5. For the (111) and the (222) reflections, the measured and calculated lattice spacing are the same. This is expected since the lattice spacing is calculated from a_{111} and the (222) reflection is a higher order of the (111) reflection.

The measured and calculated d_{220} and d_{311} for $X = 6$ and $X = 18$ mm are the same. This is expected for unstrained powder. For all other positions, the measured lattice spacings other than d_{111} and d_{222} are smaller than the calculated d_{hkl} . This indicates that the (111) crystallites are differently strained compared to all other oriented (hkl) crystallites.

8.1.5 Peak Broadening

Figure 8.6 shows the FWHM in reciprocal Angström as a function of X . The fitting error is indicated. Independent of position, FWHM_{222} is larger than FWHM_{111} (see the dashed red line). Except for FWHM_{200} for coatings at $X = -30$ and 30 mm, FWHM of all other reflections are above the line connecting FWHM_{111} and FWHM_{222} . This indicates that the size and strain distribution of (111) reflection differs compared to size and strain distribution of all other (hkl) reflections.

The FWHM might be influenced by both crystallite size (i.e. size broadening) and strain distribution (i.e. strain broadening). As discussed in section 4.4, size and strain broadening have different behavior. If size broadening is dominant, then FWHM of a given (hkl) reflection is approximately same as FWHM of its higher order reflection. If strain broadening is dominant, then FWHM of the n^{th} higher order reflection is approximately n times larger than FWHM of (hkl) reflection.

A higher order reflection was only measured for the (111) reflection. In order to evaluate which factor is dominating the peak broadening, the ratio between FWHM_{222} and FWHM_{111} was calculated. The results are presented in Fig. 8.7 for coatings in the range of $-36 \text{ mm} < X < 36 \text{ mm}$.

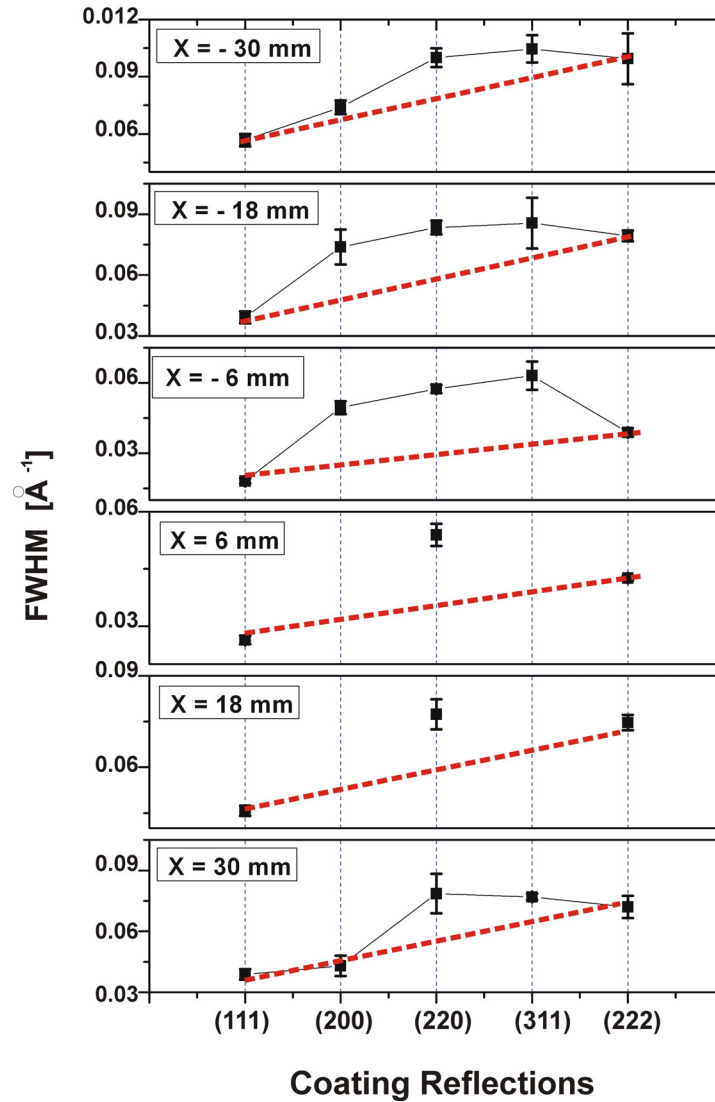


Figure 8.6: The FWHM as a function of reflections and position.

In the range $0 \text{ mm} < X < 24 \text{ mm}$, the ratio between FWHM_{222} and FWHM_{111} is between 1 (expected for the size broadening only) and 2 (expected for strain broadening only). This indicates that at these positions, both size and strain broadening cannot be neglected. For other positions, FWHM_{222} is approximately two times larger than FWHM_{111} . For these positions, the FWHM is dominated by the strain broadening and the size broadening can be neglected.

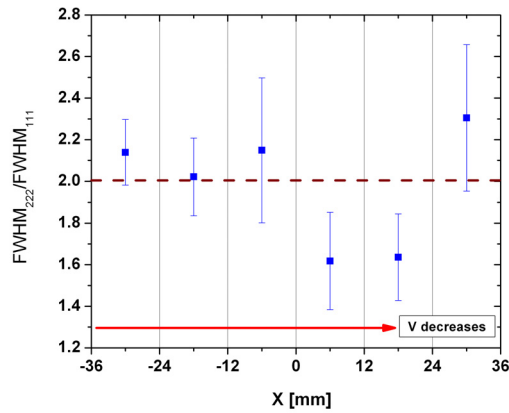


Figure 8.7: The ratio of FWHM_{222} and FWHM_{111} as a function of position.

8.1.6 Main Results

Radial scans for selected position below the target have been measured. They consist of coating and substrate reflections which can be separated.

The crystal structure, the lattice spacing and the peak width of the coatings have been analyzed as a function of position below the target. We found that independent of X , all coating reflections are attributed to fcc lattice.

Independent of the reflection, the lattice spacing has a parabolic like shape as a function of position. The minimum d_{hkl} is not found for coating having the smallest Vanadium concentration. This indicates that the lattice spacing is not only influenced by chemical composition but also by microstructure.

The peak width is a superposition of the strain and size distribution. In order to evaluate which factors are dominant, the ratio of FWHM_{222} and FWHM_{111} are calculated. It is found that for coatings in the range $0 \text{ mm} < X < 24 \text{ mm}$, the peak width is influenced by both size and strain broadening. For all other positions, the size broadening is negligible.

8.2 Texture Analysis

The radial scans of all selected positions indicate a strong (111) texture. Other types of texture cannot be identified from the radial scan only.

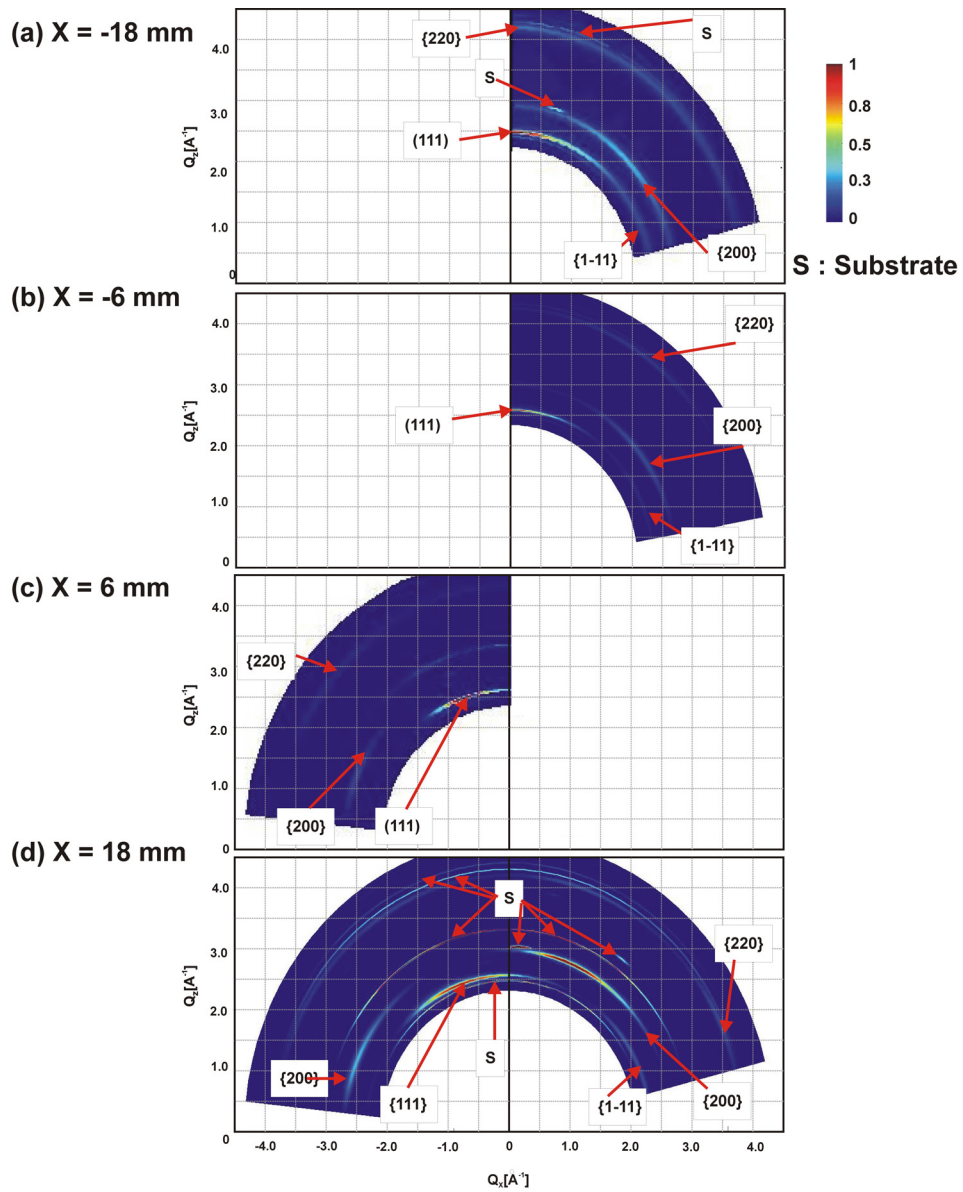


Figure 8.8: Strain maps for coatings in the range of $-24 \text{ mm} < X < 24 \text{ mm}$.

In order to analyze the texture in detail, the (111) and (200) pole figures and a strain map covering the (111), the (200), and the (220) reflections were measured for sample position in the range of $-24 \text{ mm} < X < 24 \text{ mm}$.

Figure 8.8 shows the strain map at selected positions presented in the linear intensity scale. For each position, the measured intensity is normalized to the maximum intensity. The maximum intensity for $X = 18 \text{ mm}$ is found for the (200) reflection. For all other

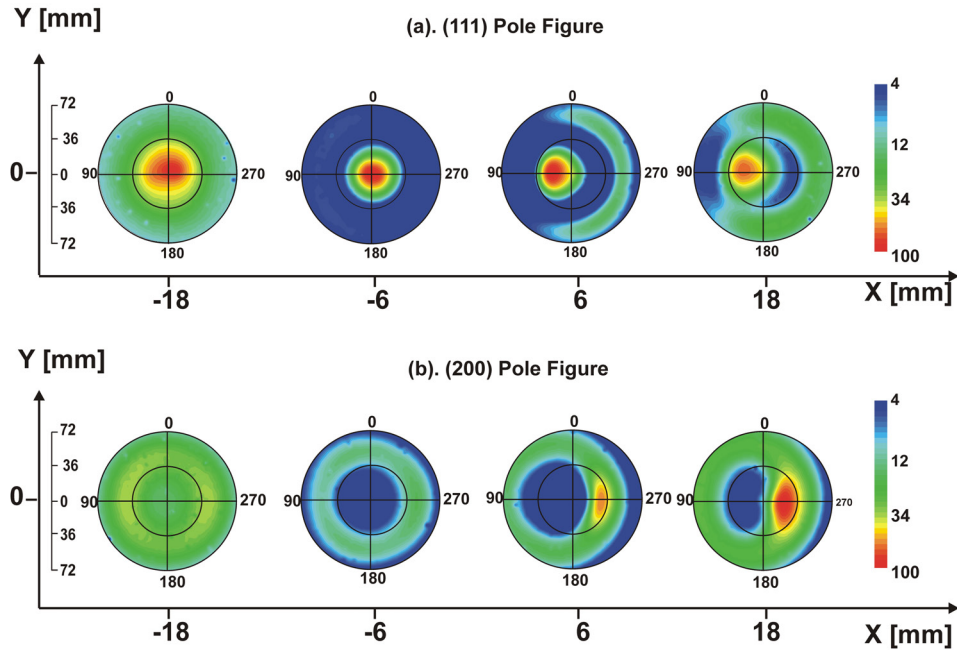


Figure 8.9: (111) and (200) pole figures of the coatings on cemented carbide.

positions, the strongest intensity is attributed to the (111) reflection. For all positions, the (220) reflection is the weakest. Independent of X, intensity of the coating reflections is not distributed homogeneously along the powder rings. This indicates texture.

The crystallographic orientation of the crystallites is studied by analyzing the pole figure. Figure 8.9 shows the (111) and (200) pole figures in logarithmic scale. They were measured in the range of $0^\circ < \Psi \leq 72^\circ$ and $0^\circ < \phi \leq 360^\circ$. The measured intensity is corrected for absorption as described in [55], but not for geometry effects.

The intensity of the (111) and the (200) pole figures is normalized to the maximum intensity of stronger reflection, similar to the normalization of the strain maps.

Independent of the sample position below the target, the maximum intensity of the (111) pole figure is observed close to center of the pole figure which indicates (111) texture. For the (200) pole figure, the (200) ring is attributed to this (111) texture without in-plane orientation. Thus both (111) and (200) pole figures and the strain maps indicate that the dominant texture of the coatings is the (111) texture.

For all positions, the (200) ring is superimposed with another intensity distribution. This indicates a superposition of the isotropic (111) texture and other textures. In the follow-

ing, the co-existing textures at different sample positions below the target are described.

8.2.1 Texture Superposition for X = -18 mm

The (111) pole figure for X = -18 mm is shown in Fig. 8.10 (a). For better observation of intensity distribution, the (200) pole figure and the (220) strain map are presented with enhanced color scale in Fig. 8.10 (b) and (c).

For X = -18 mm, the (200) pole figure indicates a superposition between the (200) ring and an intensity distribution which has a two-fold symmetry. This intensity distribution is expected for an in-plane oriented (220) texture. The (220) texture is also indicated by the intensity distribution of the (220) strain map at $\Psi \approx 0^\circ$ (dashed circle in Fig. 8.10 (c)).

The schematic (111), (200) and (220) pole figures expected for a superposition of the isotropic (111) texture and the in-plane oriented (220) texture are shown in Fig. 8.10 (d) to (f). The gray background corresponds to the measurement range of our pole figures. The expected intensity distribution of the (111) texture is represented in red while the expected intensity distribution of the in-plane oriented (220) texture is represented in green.

For confirmation of a superposition of the (111) texture and the (220) texture, line scans the (111) pole figure, the (220) pole figure and the (220) strain maps were fitted with the calculated peak position taking into account the cubic symmetry (described in section 4.5.1 and 4.5.3). The cut directions of the line scans are indicated as blue arrows in the schematic pole figures.

The fitting results are presented in Fig. 8.10 (g) to (i). The sum of the fitted peaks (blue lines) at lower Ψ is adjusted to the measured intensity while at higher Ψ the sum is adjusted larger than measured intensity to account for geometry corrections [70].

The average orientation Ψ_{111} and orientation distribution σ_{111} are determined from the fit of the (111) peak close to $\Psi = 0^\circ$ which is shown as red shaded area in Fig. 8.10 (g).

The (220) strain map was not measured in the complete range of Ψ and covers the peak only partially. To minimize the fitting error, Ψ_{220} and σ_{220} are determined not only from the maximum of the (220) strain map but also from the line scan of (200) pole figure (green shaded area in Fig. 8.10 (h) and (i)).

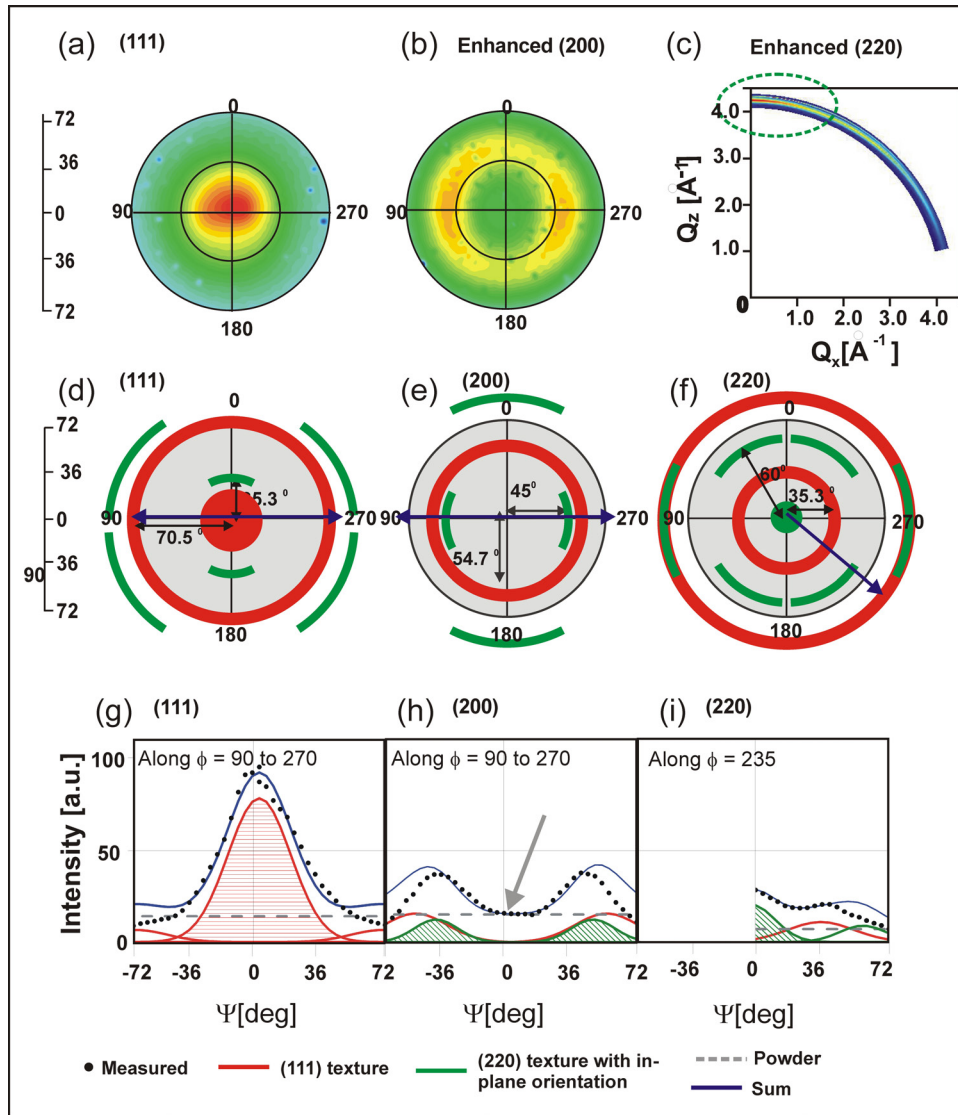


Figure 8.10: (a) (111) and (b) (200) pole figures, (c) (220) strain map, (d) to (f): schematic (111), (200) and (220) pole figures for a superposition of the (111) texture, the (220) texture, and the powder-like crystallites, (g) to (i): line scans and fittings of the (111), the (200) and the (220) reflections.

The intensity distribution of all reflections can only be explained by a superposition of the (111) texture, the (220) texture and the crystallites with a random, powder like distribution (see the gray arrow in Fig. 8.10 (h)). For the powder crystallites, the intensity of the (111), the (200) and the (220) reflections is calculated with PowderCell 2.3 software [71] assuming stoichiometric VC. The intensity ratio used for the fitting is $I_{111} : I_{200} : I_{220} = 93 : 100 : 52$.

Thus for this position, fitting of the line scans gives an additional information which is the presence of the powder crystallites. For all sample positions, the fit results for Ψ_{111} , Ψ_{220} , σ_{111} , and σ_{220} are given in Fig. 8.14 (b) and (c).

8.2.2 Texture Superposition for X = -6 mm

Figure 8.11 (a) to (c) present the (111) pole figure, the enhanced (200) pole figure and the enhanced (220) strain map for X = -6 mm. The (200) pole figure shows a superposition of the (200) ring expected for (111) texture without in-plane orientation and an intensity distribution with three-fold symmetry. This intensity distribution is expected for an in-plane oriented (111) texture. One peak of this three fold intensity distribution (at $\phi = 270^\circ$) is stronger than the other two peaks at $\phi = 150^\circ$ and at $\phi = 30^\circ$. This might be related to coexistence of other weak textures with in-plane orientation.

As for X = -18 mm, line scans of all reflections are fitted by calculating the peak position for cubic symmetry. The results are presented in Fig. 8.11 (g) to (i).

The line scan of the (200) pole figure shows two maxima at higher Ψ angle having different peak intensity. This is expected for a superposition of (111) texture with and without in-plane orientation.

The weak (200) peak close to $\Psi \approx 0^\circ$ is an indication of a weak (200) texture (brown shaded area in figure 8.11 (h)). Because this texture is weak, it does not contribute significantly to the other line scans.

The green shaded area in Fig. 8.11 (i) indicates a weak (220) texture. Since the (220) strain map was not measured for the entire Ψ range, fitted Ψ_{220} and σ_{220} have large error bars (see Fig. 8.14 (b) and (c)).

We have shown that the intensity distribution of the coating at X = -6 mm can only be explained by a superposition of the (111) texture with and without in-plane orientation, the (200) texture, the (220) textures and powder. Except the (111) texture, the other coexisting textures can only be verified from the line scans fitting. The schematic (111), (200) and (220) pole figures for a superposition of those textures are presented in Fig. 8.11 (d) to (f).

The in-plane oriented (220) texture and the powder are observed for X < 0 mm. Other coexisting textures are observed for X = -6 mm, which are in-plane oriented (111) and (200) textures.

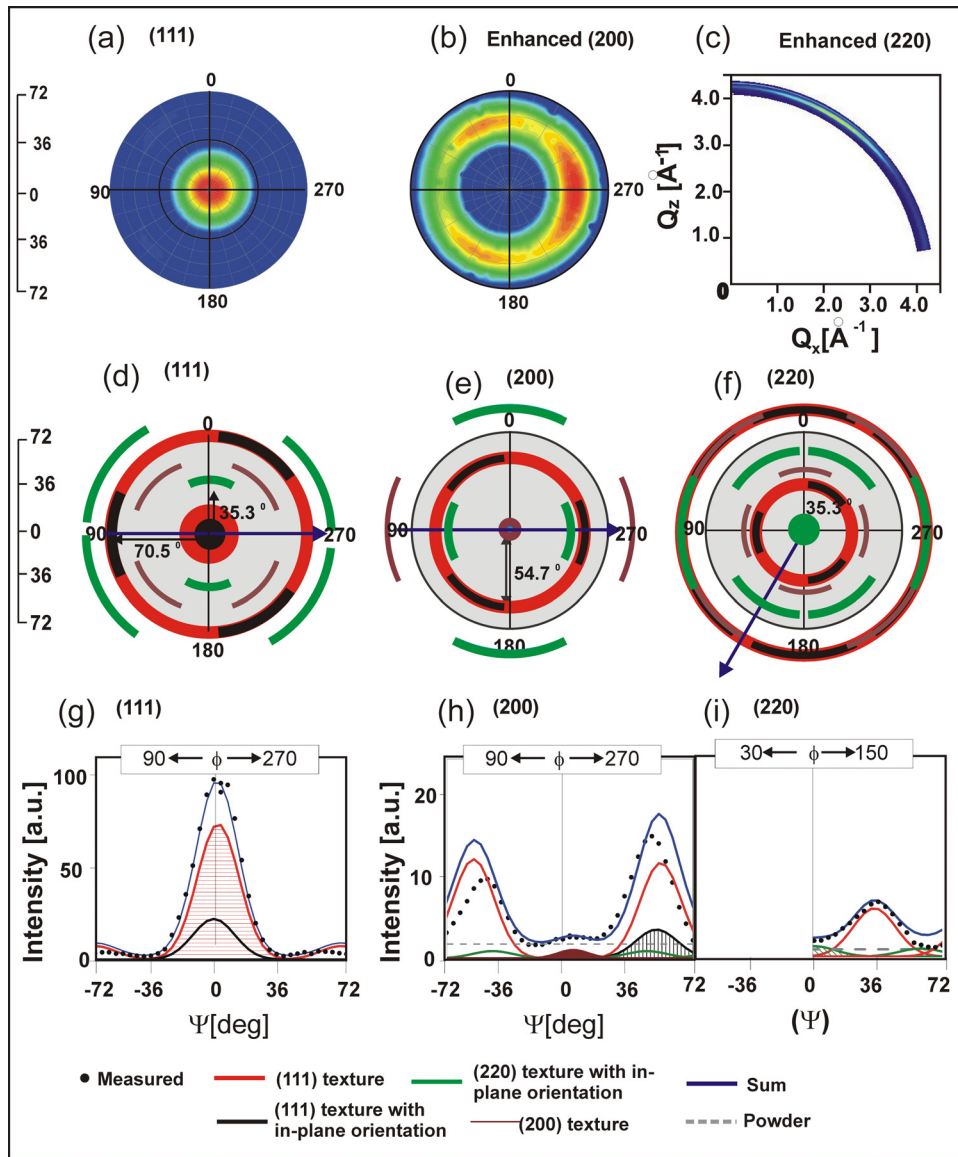


Figure 8.11: Measured (a) (111) pole figure, (b) enhance (200) pole figure and (c) enhanced (220) strain map. Schematic (d) (111), (e) (200) and (f) (220) pole figures for a superposition of (111), (200) and (220) textures. Line scans of (g) the (111), (h) the (200) and (i) the (220) reflections are fitted by calculating the peak positions for cubic symmetry.

8.2.3 Texture Superposition for X = 6 mm

Figure 8.12 (a) to (c) presents the (111) pole figure, the (200) pole figure and the (220) strain map. The peak of the (111) pole figure is tilted relative to the center of the pole figure which indicates a tilted (111) texture. Due to this tilting, the $(1\bar{1}1)$ ring is shifted towards this peak so that part of the $(1\bar{1}1)$ ring is out of the measurement range (the dashed red circle in Fig. 8.12 (a) corresponds to the expected $(1\bar{1}1)$ ring).

The dashed red circle in the (200) pole figure (Fig. 8.12 (b)) represents the expected (200) ring of the (111) texture without in-plane orientation. This ring is superimposed with another intensity distribution at $\phi = 270^\circ$. Possible explanations for this intensity distribution are discussed as follows.

If the intensity distribution at $\phi = 270^\circ$ is attributed to tilted (200) texture, then the (111) pole figure should have a peak along the dashed pink circle. This is not observed, therefore we conclude that this intensity distribution cannot be explained with the tilted (200) texture.

The in-plane oriented (111) texture has an intensity distribution with three fold symmetry. Therefore if this is exist, two peaks (along dashed black circles in Fig. 8.12 (b)) are expected and forms three-fold symmetry with the peak in $\phi = 270^\circ$ direction. If in-plane oriented (220) texture exist, a peak along the dashed white circle is expected. Both dashed black and white circles are at edge of our measurement range. Furthermore, the data is not corrected for geometry effect. This might be the reason why not all of the expected peaks are observed.

To determine all coexisting textures, line scans of all reflections are fitted. A superposition of the (111) texture with and without in-plane orientation is assumed. The schematic (111), (200) and (220) pole figures for this superposition are given in Fig. 8.12 (d) to (f). The cut directions of the line scans are indicated by blue arrows in the schematic pole figure.

The best fitting results of the (111), the (200) and the (220) reflections are given in Fig. 8.12 (g) to (i). For all reflections, the sum of the fitted intensity at $\Psi > 36^\circ$ is higher than the measured intensity to account for geometry effects.

The measured intensity of the (200) line scan in the range $24^\circ < \Psi < 36^\circ$ is larger than sum of the fitted intensities (see green arrow in Fig. 8.12 (h)). This discrepancy cannot be related to the geometry effect and cannot be minimized by adjusting height, position or FWHM of the fitted peaks. The line scans do not indicate other textures. Therefore the discrepancy might be related to a non-Gaussian orientation distribution function.

Thus for this position, the intensity distribution of all reflections can be explained by (111) texture with and without in-plane orientation. For $X = -6$ mm, Ψ_{111} of the (111) texture with and without in-plane orientation is close to the surface normal. For $X = 6$ mm, those textures are tilted.

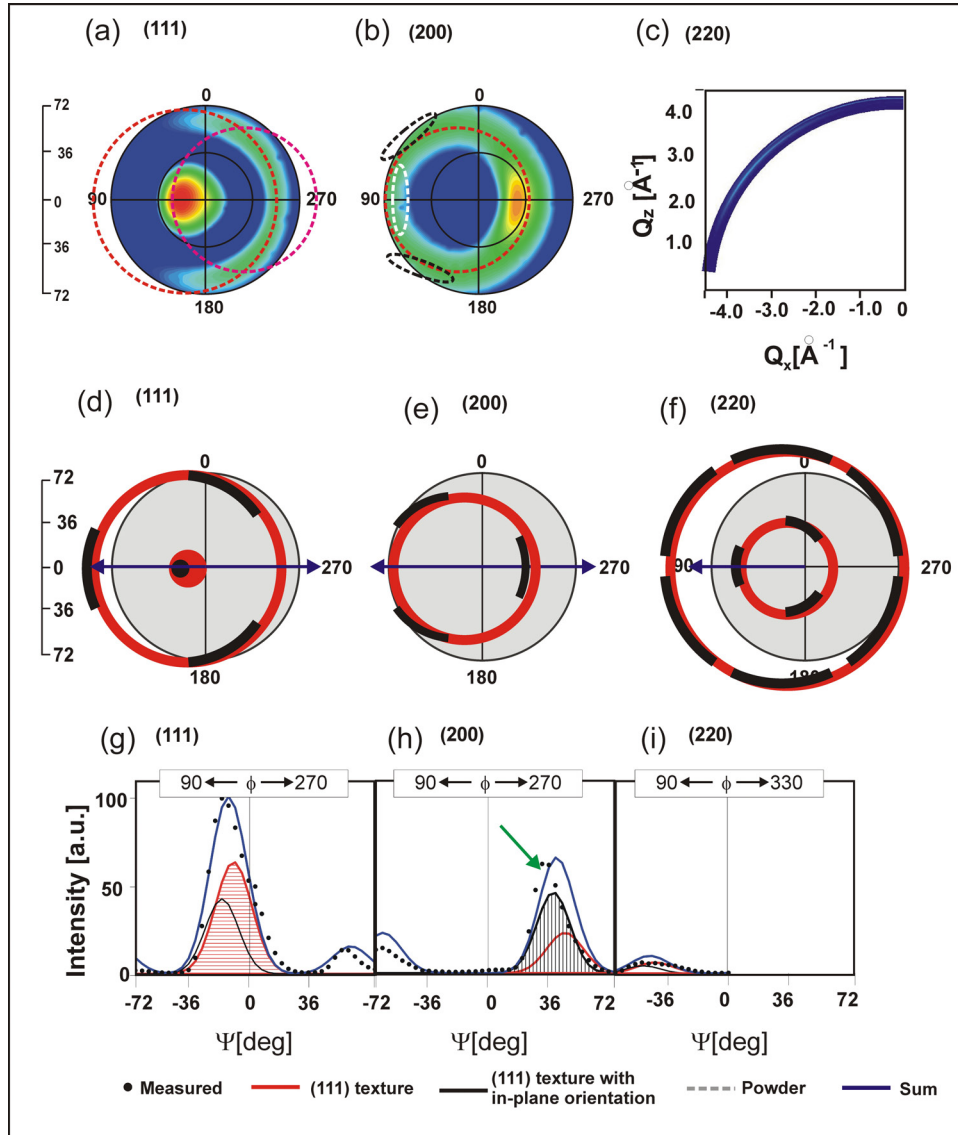


Figure 8.12: (a) (111) and (b) (200) pole figures, (c) (220) strain map, (d) to (f): schematic (111), (200) and (220) pole figures for a superposition of the isotropic and anisotropic (111) texture, (g) to (i): line scan and fitting of the (111), the (200) and the (220) reflections.

8.2.4 Texture Superposition for X = 18 mm

The (111) and (200) pole figures for X = 18 mm are shown in Fig. 8.13. They have the same features as the pole figures for X = 6 mm, which are (1): the peak of the (111) pole figure is tilted relative to $\Psi = 0^\circ$ and (2): the (200) ring is superimposed with a peak in $\phi = 270^\circ$ direction.

Since the (111) and the (200) pole figures for this position are similar to the pole figures for X = 6 mm, the line scans are fitted assuming a superposition between tilted (111) texture with and without in-plane orientation as for X = 6 mm. The best fitting results are presented in Fig. 8.13 (g) to (i).

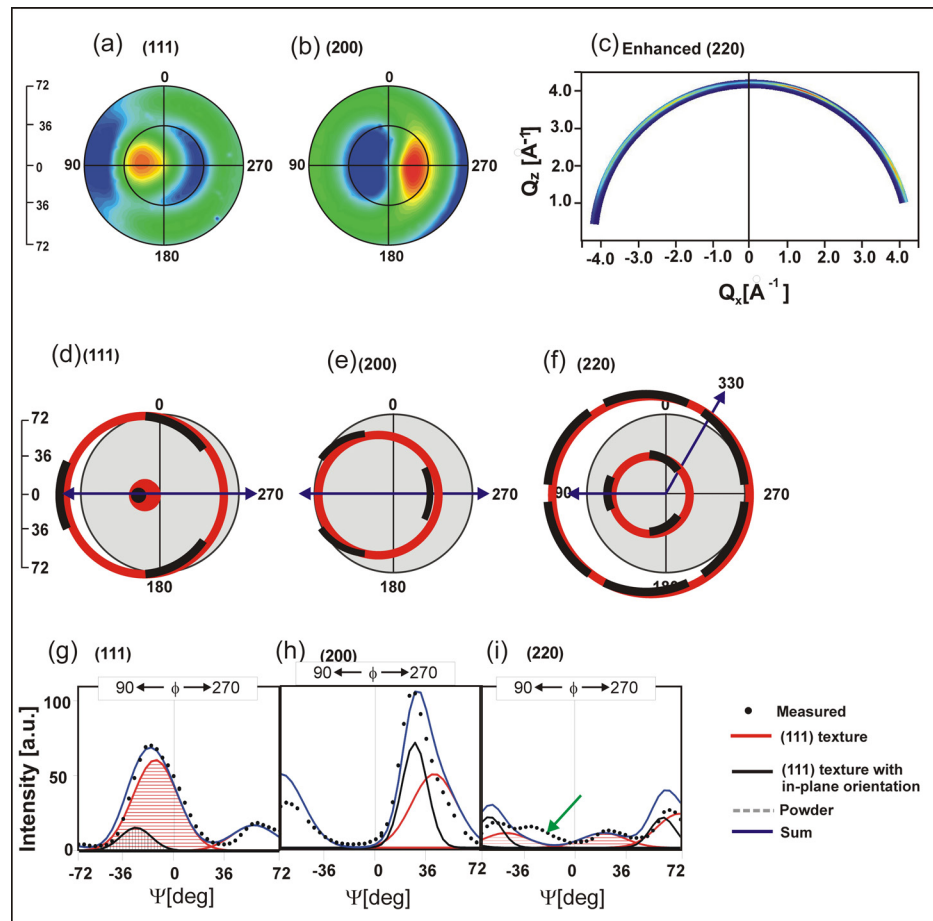


Figure 8.13: (a) (111) and (b) (200) pole figures, (c) (220) strain map, (d) to (f): schematic (111), (200) and (220) pole figures for a superposition of the isotropic and anisotropic (111) texture, (g) to (i): line scan and fitting of the (111), the (200) and the (220) reflections.

The green arrow in Fig. 8.13 (i) points out a weak peak in the (220) line scan which cannot be explained by a superposition of (111) texture with and without in-plane orientation only. This indicates the existence of another weak texture. The measurement of other pole figures such as the (220) pole figure is necessary to determine the type of this texture.

Because the texture which cannot be verified is weak, it does not contribute significantly to the intensity of the (111) and the (200) line scans. Therefore Ψ_{111} and σ_{111} can still be determined from fitting of the (111) and the (200) line scans in Fig. 8.13 (g) and (h).

8.2.5 Main Results

The texture analysis of the coatings in the range of $-24 \text{ mm} < X < 24 \text{ mm}$ has been performed using pole figures and strain map. The strong and dominant textures are visible from the pole figures and strain map. Weak textures can only be verified by fitting the line scans of pole figures and strain map.

The type of textures as a function of position are summarized in Fig. 8.14 (a) while the average orientation and the orientation distribution of the textures are given in Fig. 8.14 (b) and (c). The color symbols represent different type of textures as indicated in Fig. 8.14. The size of the spheres in Fig. 8.14 (a) represents qualitatively the fraction of each type of texture in each sample.

Independent of the position, all coatings have a dominant (111) texture without in-plane orientation. The average orientation Ψ_{111} and orientation distribution width σ_{111} varies as a function of position X. The largest Ψ is found for coatings below the AlN target, close to the center of target. At $X = 6 \text{ mm}$, the coating also has the narrowest σ_{111} .

The (111) and the (200) pole figures, and the (220) strain map indicate the coexistence of other textures. The in-plane oriented (111) texture is stronger for coatings below the AlN target (positive X) than for coatings below the VC target (negative X). The in-plane oriented (220) texture is observed for coatings at $X < 0 \text{ mm}$ while the (200) texture is only observed for $X = -6 \text{ mm}$. The line scan fitting for coating at $X = 18 \text{ mm}$ indicates the coexistence of another texture which cannot be verified without analyzing other pole figures such as the (220) pole figure.

The analysis of pole figure and strain map shows that texture superposition of the coatings on cemented carbide depends on the position below the target. It is shown in section 7.2 that the chemical composition varies as a function of X as well. The influence of the position below the target, the substrate type and the chemical composition on the tex-

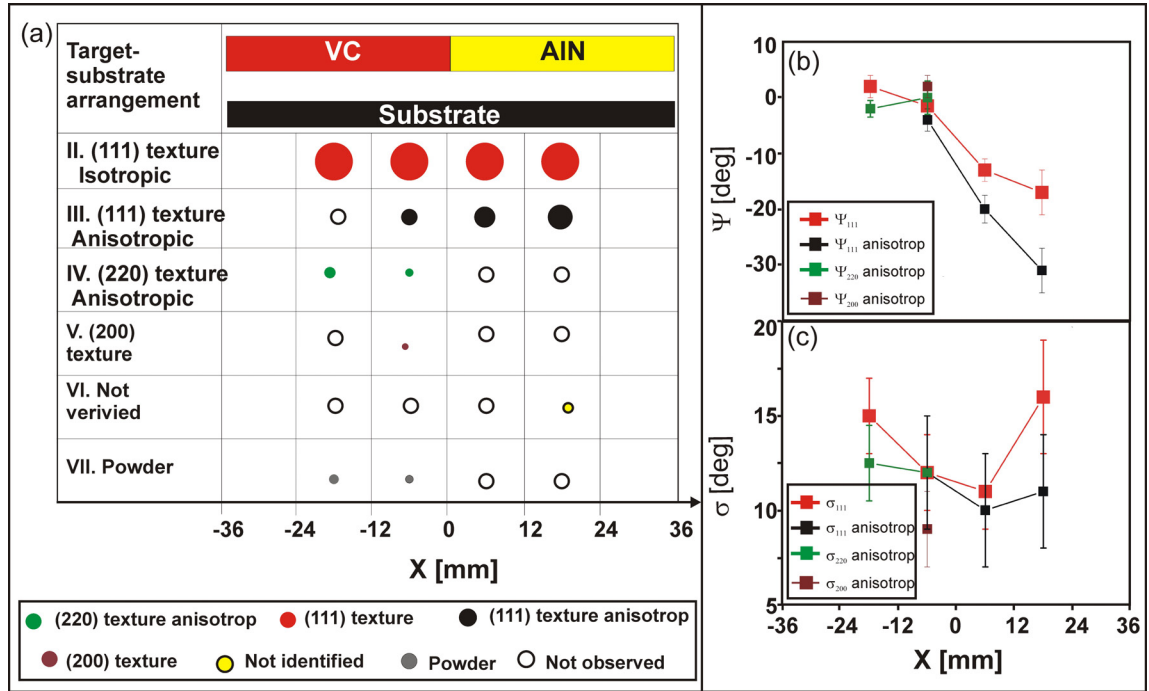


Figure 8.14: (a) Qualitative summary of the crystallographic orientation of the coatings as a function of position below the target (X), (b) fitted average orientation Ψ_{hkl} and (c) fitted orientation distribution σ_{hkl} of the textures.

ture will be discussed in chapter 12.

8.3 Influence of the Texture Superposition on d_{hkl}

The intensity distribution of the strain maps has been analyzed in order to investigate the texture superposition of the coatings. For all positions, the main texture is the (111) texture without in-plane orientation. Depending on the position, the coexisting textures are the in-plane oriented (111) texture, the (200) texture and the (220) texture.

The strain map does not only measure the intensity distribution, but also the radial peak position as a function of Ψ . The (111), the (200) and the (220) reflections of the strain map for all samples have been fitted using the Fityk software.

The lattice spacing was then calculated by inserting the fitted peak position into the Bragg equation. Figure 8.15 shows lattice spacing of the (111), the (200) and the (220) reflections as a function of the tilt angle Ψ for sample in the range of $-24 \text{ mm} < X <$

24 mm. Some of the coating peaks are too weak to be fitted. Therefore, their lattice spacing was not calculated (gray regions in Fig. 8.15 (h), (i), and (k)).

Independent of the sample positions, the lattice spacings do not always decrease monotonously as a function of Ψ . The extreme cases are found for (220) reflection in Fig. 8.15 (c) and (f) where the maximum d_{220} is found at $\Psi \approx 22^\circ$.

A monotonous decrease of the lattice spacing as a function of Ψ is expected for compressive lateral strain of a homogeneous coating. Because this is not observed in all of our coatings, the lattice spacing might be influenced by the texture superposition. In the following, the influence of the texture superposition on the lattice spacing as a function of Ψ is investigated.

The texture superposition for the sample at $X = -6$ mm as performed in section 8.2.2 is presented again in Fig. 8.16 (a) to (c). The corresponding lattice spacing is presented in Fig. 8.16 (d) to (f).

As shown in Fig. 8.16 (a), the measured intensity of the (111) line scan is dominated by the (111) texture and the powder. However, the intensity ratio between the (111) texture and the powder is varied as a function of Ψ . In the range of $32^\circ < \Psi < 48^\circ$ (see the zoom), the intensity attributed the powder is larger than intensity attributed to (111) texture. Outside this range, intensity attributed to the (111) texture is more dominant than intensity of the powder.

The intensity ratio variation of the (111) texture and the coexisting texture as a function of Ψ was also investigated for (200) and (220) line scans. The result is summarized as follows. The color background (red, gray or green) in Fig. 8.16 corresponds to the region where the measured intensity is mostly attributed to a specific type of texture (indicated in this figure). The white background corresponds to the region with no dominant texture or powder-like distribution .

Figure 8.16 (d) to (f) show the d_{hkl} vs. Ψ plots of all reflections. The d_{hkl} vs. Ψ in each plot can be divided into three linear regions having different gradients. The black line corresponds to a negative gradient while the green solid line corresponds to a positive gradient.

It is shown that if the isotropic (111) texture is dominant, the d_{hkl} decreases as a function of Ψ (black lines in all red regions). The negative gradient is also observed for region where the measured intensity is attributed to superposition of the coexisting textures only (gray background in Fig. 8.16 (e)) .

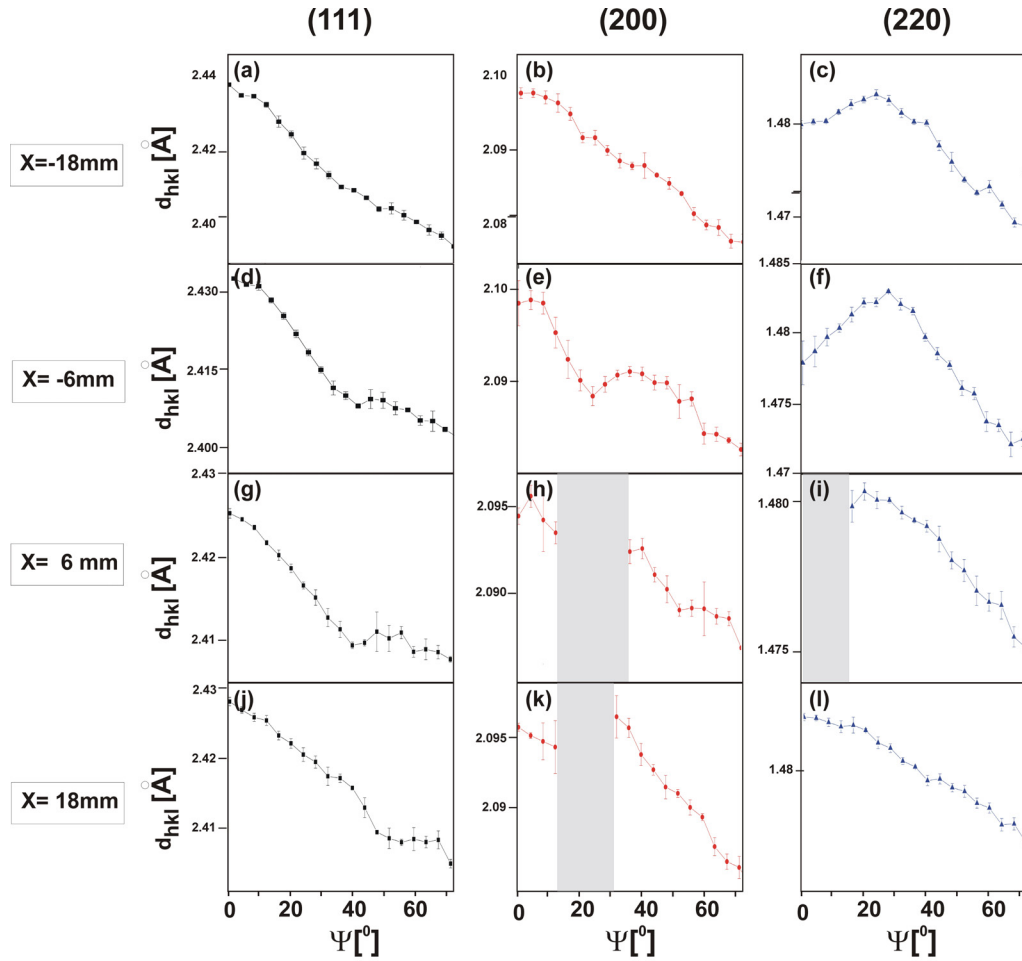


Figure 8.15: Columns: d_{hkl} vs Ψ plot for the (111), the (200) and the (220) reflections. Rows: d_{hkl} vs Ψ plot at different X.

The positive gradient (green lines) in the d_{111} , the d_{200} and the d_{220} vs. Ψ plots was observed at the region where the superposition of the (111) texture with other coexisting textures is in such a way that (1) the (111) texture in this region is not dominant, however (2) the intensity related to the (111) texture increase with increasing Ψ . This might indicates that the lattice spacing and strain of the different (hkl) crystallites are varied.

From the sample at $X = -6$ mm, we conclude that the lattice spacing as a function of Ψ is influenced by the compressive lateral stress, the lattice parameter of each type of texture and the texture superposition. This might explains why for all samples, some d_{hkl} do not decrease monotonously as a function of Ψ . For the same reflection at different sample

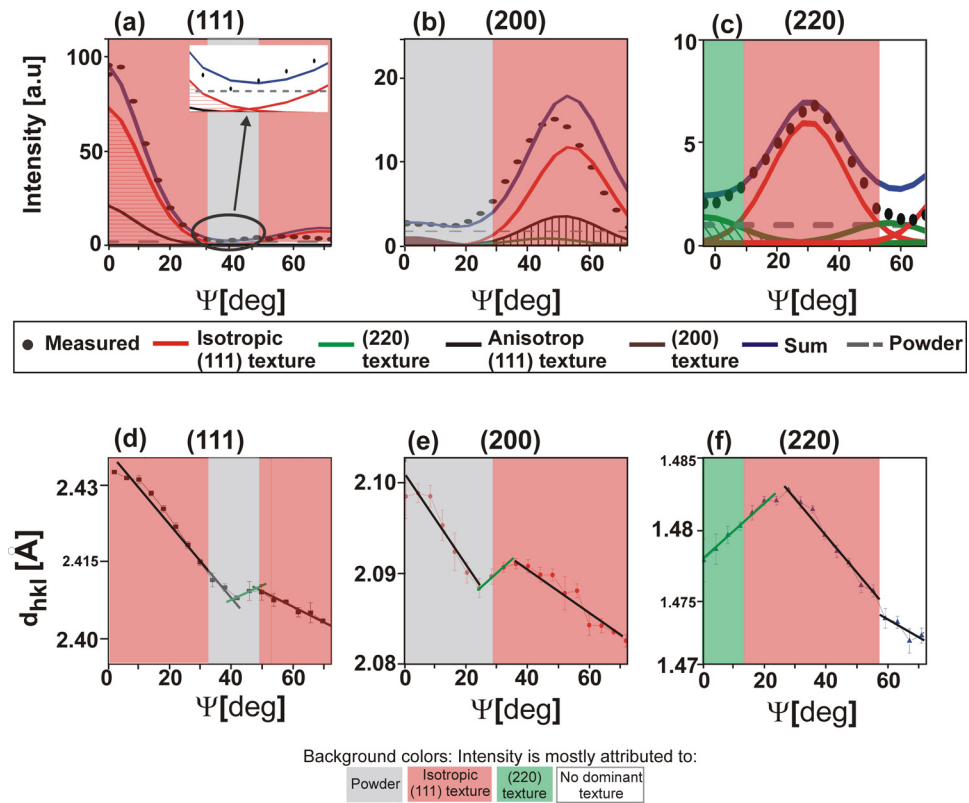


Figure 8.16: The texture superposition of (a) the (111), (b) the (200) and (c) the (220) reflection for the sample at $X = -6$ mm, and (d) to (f): their corresponding d_{hkl} vs Ψ plots.

positions, the feature of the d_{hkl} vs. Ψ plots vary depending on how the dominant (111) texture is superimposed by other textures.

9 X-Ray Diffraction Results of (V,Al)(C,N) Thin Films on Si

Similar X-Ray Diffraction measurements as for coatings on cemented carbide were performed for coatings on Si(001). Two rows of Si(001) substrates (six individual substrates at each row) were coated simultaneously during rf sputter deposition. The microstructure variation as a function of position at each row were analyzed. The microstructure variation between the first and the second row coatings were discussed. The crystal lattice, the grain size, and the strain distribution of coatings on cemented carbide and on Si are compared.

9.1 Sample Coordinate System

The second series of our coatings was deposited on Si(001) substrates. The bottom view projection of the sample positions relative to the target during deposition is shown in Fig. 9.1 (a). The sample positions relative to the target represents the deposition geometry. Twelve individual substrates were placed in two rows.

The fluorescence map and corresponding cartesian coordinate system are given in Fig. 9.1 (b). The abrupt intensity change of first row coating at $X = -15$ mm indicates that the coating at this position was not at the intended position during deposition (see the gray arrow). Because the position is not known, we exclude this coating from our investigation.

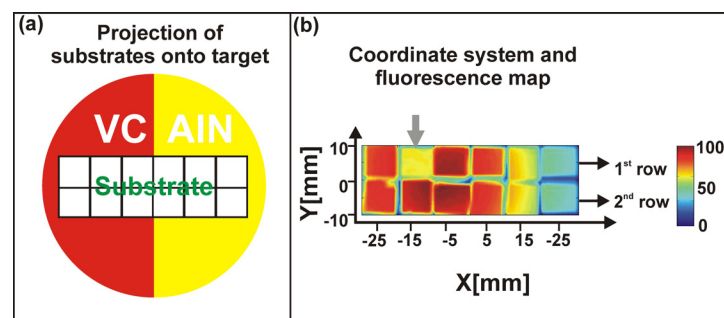


Figure 9.1: (a). Projection of the sample positions on the target, (b) fluorescence intensity map of the coatings on Si and the corresponding coordinate system.

9.2 Analysis of the Radial Scans

9.2.1 Coating Reflections

The radial scans of coatings in the range of $-30\text{mm} < X < 30\text{ mm}$ were measured at 9.5 keV. They were measured (1) not in the specular direction in order to avoid the strong (004) reflection of the Si substrate and (2) in the direction of the average orientation of the (111) texture (see section 9.3 for detailed texture analysis).

Figure 9.2 shows the radial scans of the samples where the black lines are diffraction profiles for the first row samples and the light magenta lines are for the second row samples. The intensity is given in logarithmic scale and the diffraction vector Q_r is in reciprocal Angströms.

At the used x-ray energy, the x-ray penetration depth is larger than the coating thickness and the substrate. Therefore, the diffraction profile of the sample is a superposition of the coating reflections, the Si substrate scattering and scattering of the sample holder.

For all coatings, the broad peak at $Q_r = 4.6278 \text{ \AA}$ is attributed to the diffuse scattering of Si(004) .

In order to identify the sample holder reflections, a radial scan of the sample holder was measured as well (the diffraction profile is not shown here). The holder is made of Aluminum and has a fcc structure with lattice constant 4.0500 \AA . The sharp peaks indicated by green dashed lines at $Q_r = 2.6821 \text{ \AA}$ and 3.0964 \AA are attributed to the (111) and (200) peak positions of the Al sample holder.

All reflections in Fig. 9.2 which cannot be attributed to the substrate and sample holder reflections are attributed to the coating reflections. For all samples, six coatings reflections are observed (indicated by the solid green lines). These reflections are equivalent to the coating reflections of the samples on cemented carbide substrate. We have shown in section 8.1 that those reflections are attributed to fcc lattice. The Miller indices are given on top of Fig. 9.2.

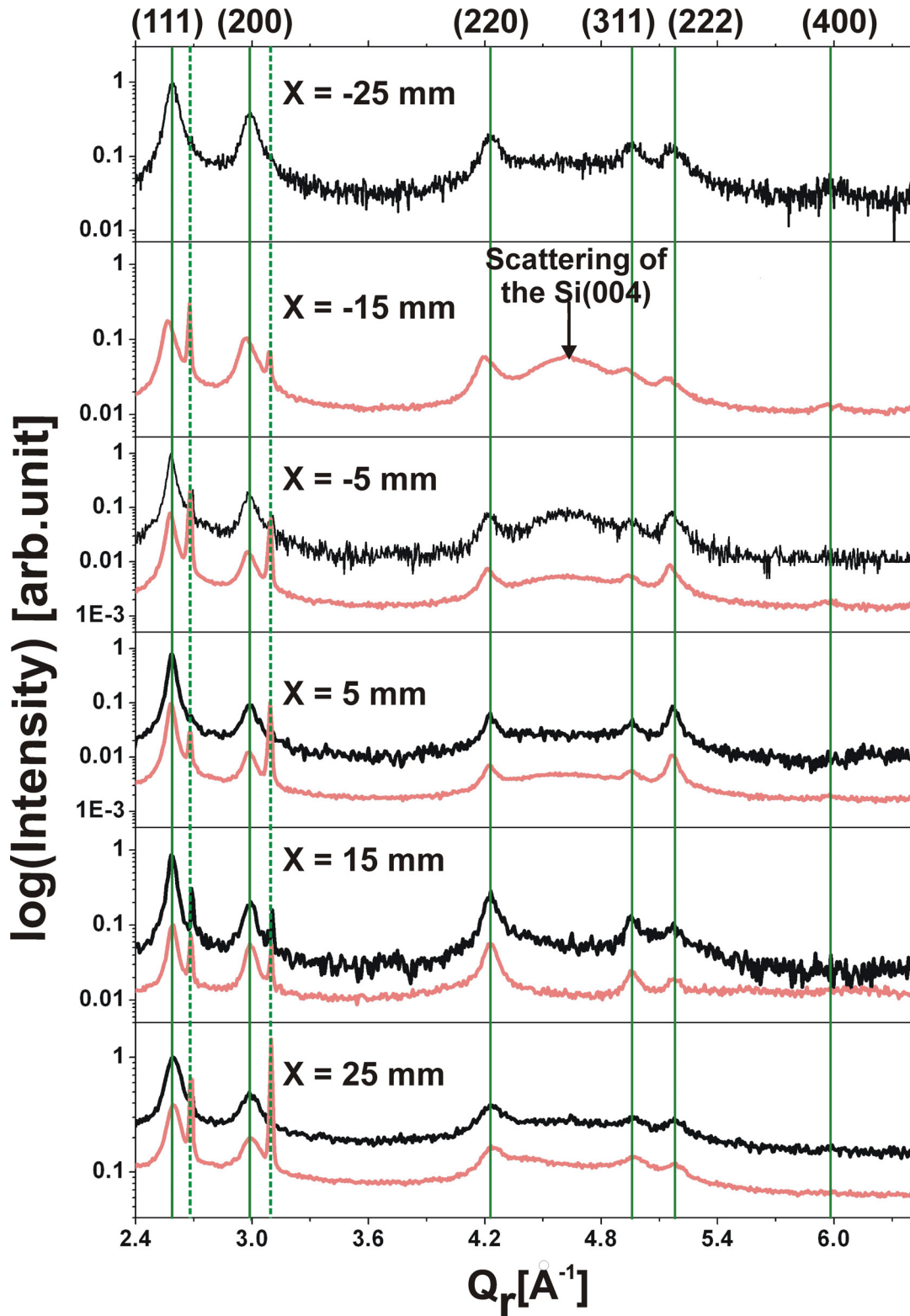


Figure 9.2: The diffraction profiles of the samples deposited on Si(001) substrates.

Independent of the position below the target, the strongest intensity is found for the (111) reflection and the weakest for the (400) reflection. This is also observed for all coatings on cemented carbide. The broad diffuse scattering of the Si(004) reflection is superimposed by the (220), the (311) and the (222) coating reflections.

For $X > -10$ mm, the radial scans of the first and second row coatings were measured. It is shown that at the same X , (1) the coating peak positions, (2) the FWHM and the relative intensity of the (hkl) reflections do not vary significantly for the first and second row samples. The coating reflections are then fitted using fityk software and presented in the next section.

9.2.2 Whole Pattern Fitting Method

The same fitting procedure as for coatings on cemented carbide was performed: the peaks are fitted by the pseudo voigt peak shape and the background is assumed as linear. Figure 9.3 presents the fit result of the radial scan for the second row coating at $X = -5$ mm. The intensity is in linear scale. The fitted peak position and the FWHM of the coating reflections are indicated.

The sample holder reflections are overlapping with the tail of the (111) and the (200) coating reflections so that the fitting errors are small. As seen in Fig. 9.3 (c), the diffuse scattering of the Si(004) reflection is broad and overlaps strongly with the (220), the (311) and the (222) coating peaks. For this reason, the fitting errors of these reflections are large.

The fitted peak positions and their errors are then used to calculate the lattice spacings and their error bars as shown in Fig. 9.4. The fitting errors are also represented as error bars in the fitted FWHM (see Fig. 9.6).

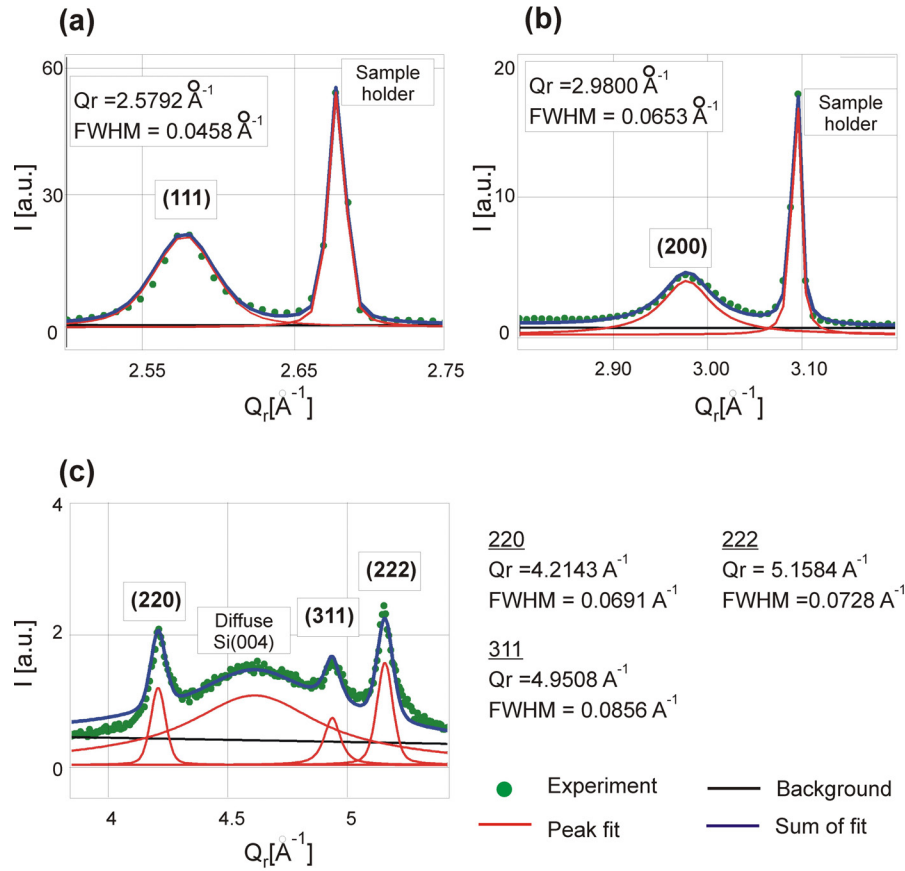


Figure 9.3: The Whole Pattern Fitting Method (WPFM) for $X = -5$ mm.

9.2.3 Lattice Spacing

Lattice spacing is calculated from the peak position using Bragg's law, $n\lambda = 2d\sin\theta$. Figure 9.4 (a) shows the lattice spacings of the first (black spheres) and second row (light magenta squares) coatings as a function of X . The lattice spacing of for the first row coating at $X = -15$ mm and the second row coating at $X = -25$ mm cannot be calculated because their radial scans were not measured. The red arrows on top of this figure indicates the direction of decreasing Vanadium concentration.

The lattice spacings of the first and the second row coatings are compared for $X > -10$ mm. It is shown that at the same X , the lattice spacing of all reflections does not vary significantly for the first and the second row coatings. For most of the reflections, the lattice spacings differences between the two rows are within the error bars. This is expected because the first and the second row coatings were deposited at symmetric position to each other with the X axis as a mirror axis.

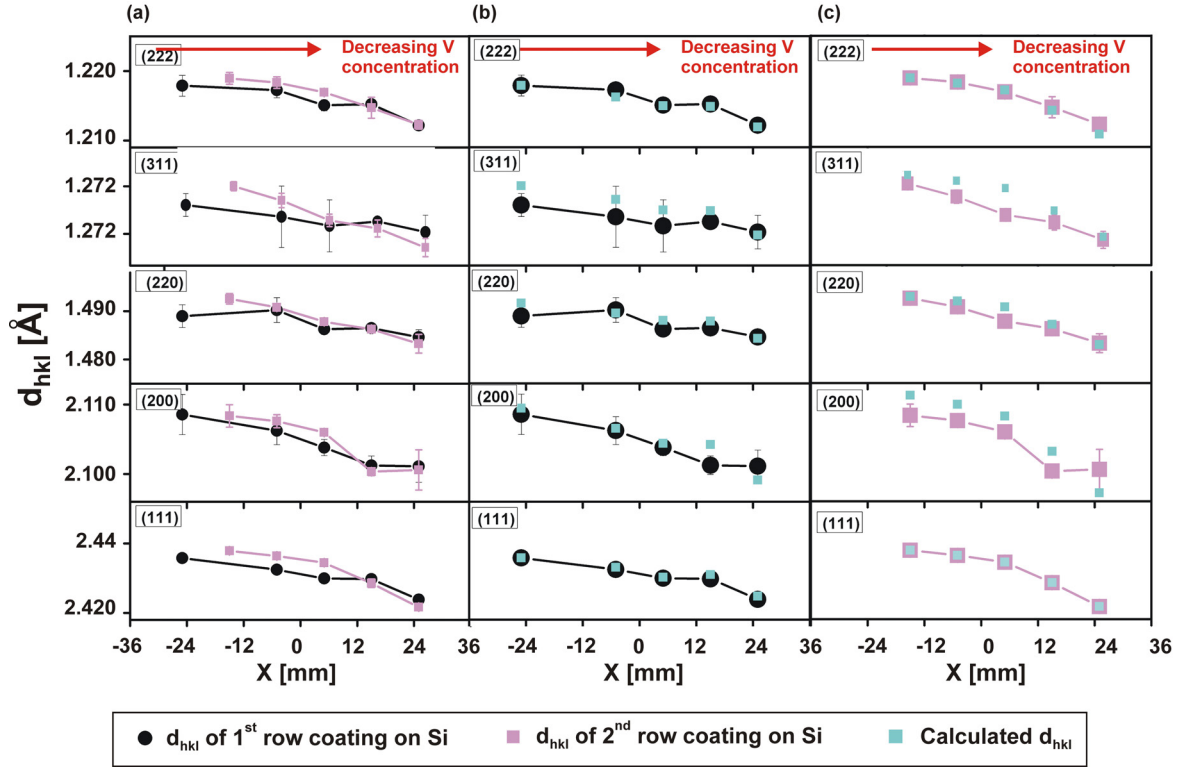


Figure 9.4: (a) Measured lattice spacings as a function of position for coatings on the first and second row coatings on Si. The measured and the calculated lattice spacing for (b) first row and (c) second row coatings on Si.

Except for the (220) reflection at $X = -25$ mm of the first row sample, the lattice spacing decreases with decreasing Vanadium concentration. This is expected for a homogeneous, unstrained mixed V-Al-C-N coating.

In order to analyze the behavior of different (hkl) reflections, the d_{hkl} of all reflections are calculated assuming a cubic, unstrained unit cell parameter with $a = a_{111}$. The calculated peak positions are represented as cyan squares in Fig. 9.4 (b) for the first row and (c) for the second row coatings. For all coatings, the measured and the calculated values of d_{111} and d_{222} are same as expected.

For the first row coatings ($Y = 5$ mm), the calculated d_{hkl} of all reflections are within the error bars of the measured lattice spacing, except for d_{200} at $X = 15$ mm (see Fig. 9.4 (b)). For the second row coatings ($Y = -5$ mm), small offset between calculated and measured d_{200} are observed. The small offset is also observed for the (311) reflection in the range of $-12 \text{ mm} < X < 12 \text{ mm}$.

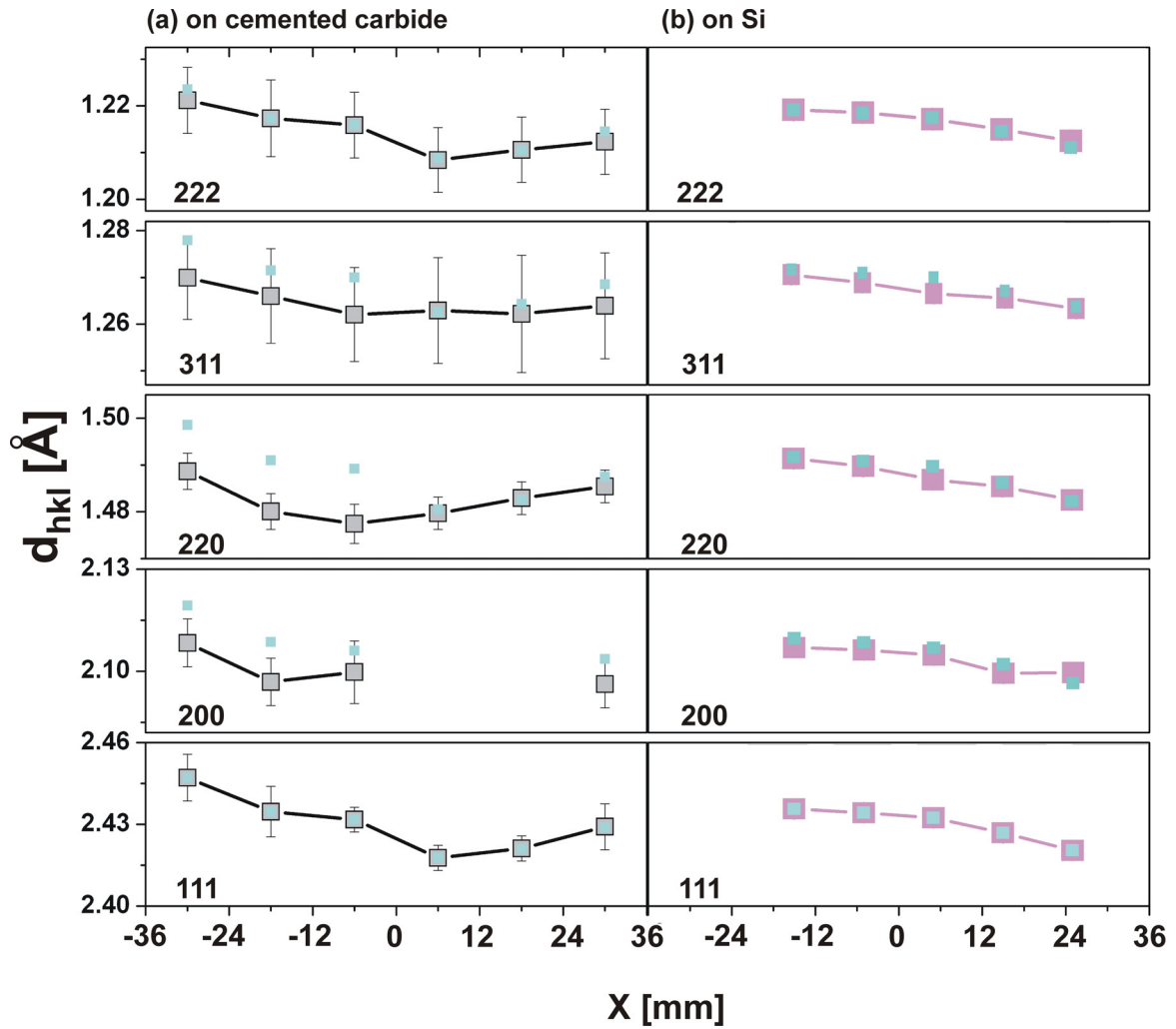


Figure 9.5: Measured and calculated lattice spacings of all reflections as a function of position for (a) coatings on cemented carbide and (b) second row coatings on Si.

Figure 9.5 presents the measured and the calculated lattice spacings of all reflections as a function of position for (a) coatings on cemented carbide and (b) second row coatings on Si. The scale in this figure is different from the scale used in Fig. 9.4.

The differences between both series of coatings are as follows: (1) For all reflections, d_{hkl} of the coatings on Si decreases with decreasing Vanadium concentration. For coatings on cemented carbide, the minimum lattice spacings of all reflections are not found for coating with minimum Vanadium concentration, and (2) for all reflections, the offset be-

tween the measured and the calculated lattice spacing is smaller for coatings on Si than for coatings on cemented carbide. This might be related to the microstructure differences between both series of coatings.

9.2.4 Peak Broadening

Figure 9.6 shows the FWHM in reciprocal Angström as a function of position below the target for (a) the first row and (b) the second row coatings. The fitting error is indicated. The red dashed line connects FWHM of the (111) and the (222) reflections. For all samples, FWHM of all other reflections are located close to this line.

The size and strain broadening of the coatings on Si is evaluated with the same procedure as for coatings on cemented carbide (see section 8.1.5), i.e. by calculating the ratio of FWHM_{222} and FWHM_{111} . The results are presented in Fig. 9.6 (c).

For all coatings, the $\text{FWHM}_{222}/\text{FWHM}_{111}$ ratio is close to two. This indicates that the FWHM for all coatings are dominated by the strain broadening.

The differences of the peak broadening behavior between coatings on Si and on cemented carbide (see section 8.1.5) are as follows. Relative to the line which links the FWHM_{111} and the FWHM_{222} , all other reflections of coatings on Si are located close to this line while all other reflections of coatings on cemented carbide are located above this line. This indicates that the size and strain distribution of (111) crystallites of coatings on cemented carbide are different from the size and strain distributions for other crystallites.

From the $\text{FWHM}_{222}/\text{FWHM}_{111}$ ratio it is found that the peak broadening of all coatings on Si is dominated by the strain broadening while for samples on cemented carbide the size broadening cannot be neglected for coatings in the range of $0 \text{ mm} < X < 24 \text{ mm}$.

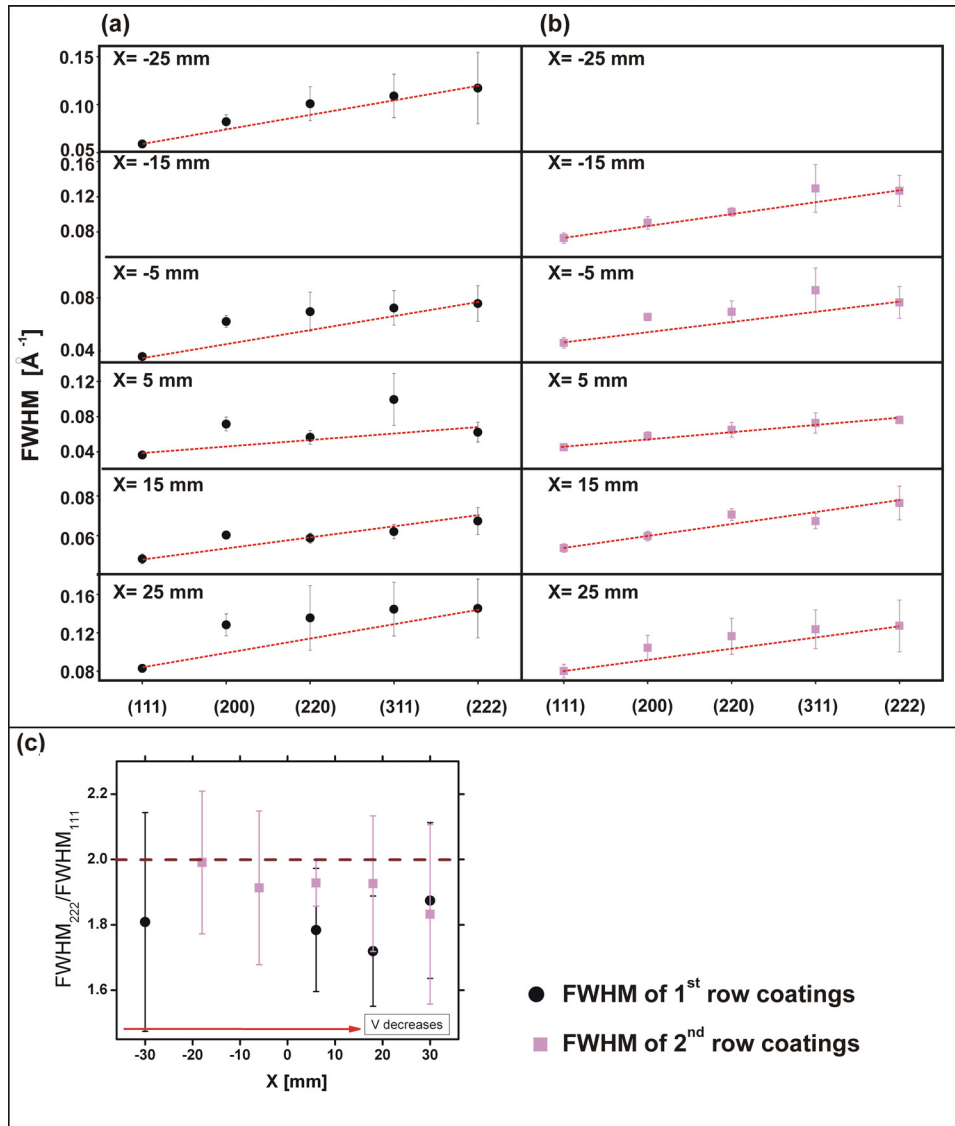


Figure 9.6: The FWHM as a function of coating reflections for different X at (a) the first row and (b) the second row coatings on Si. (c) The FWHM₂₂₂/FWHM₁₁₁ ratio.

9.2.5 Main Results

Radial scans for selected positions on Si(001) below the target have been measured. They consist of coating, substrate and Aluminum sample holder reflections. Both substrate and sample holder reflections are well identified.

The samples on Si were deposited in two rows simultaneously. The peak position, the

relative intensity and the FWHM of the first and the second row coatings are similar. This is expected because the first and second rows were deposited at position symmetric to each other with the X axis as mirror axis.

Independent of position, all coatings on Si have same type of coating reflections as found for coatings on cemented carbide. They are all attributed to the fcc lattice. However, the lattice spacing and FWHM variation as a function of X of coatings on Si and on cemented carbide are not the same.

The lattice spacings of coatings on Si decreases monotonously with decreasing Vanadium concentration while for coatings on cemented carbide the minimum lattice spacing is found in the range of $-20 \text{ mm} < X < 10 \text{ mm}$ depending on the (hkl) reflections.

For (111) crystallites, the size broadening of all coatings on Si can be neglected. For coatings on cemented carbide, the size broadening cannot be neglected in the $0 \text{ mm} < X < 24 \text{ mm}$ range.

9.3 Textures Analysis

The strain maps as well as the (111) and the (200) pole figures were measured for the first ($Y = 5 \text{ mm}$) and the second ($Y = -5 \text{ mm}$) row coatings. They are presented in this section without absorption corrections because the coating thickness was not measured (relation between thickness and absorption correction is given in Eq. 4.29). However it is found for coatings on cemented carbide that the main features of the strain maps and the pole figures do not change significantly with and without absorption correction.

Figure 9.7 shows strain maps of coatings on Si as a function of position for $X > -10 \text{ mm}$. The intensity is normalized to the maximum intensity of the (111) reflection. The strain maps cover the (111), the (200) and the (220) reflections, except for the first row coatings at $X = -5 \text{ mm}$ and $X = 15 \text{ mm}$.

Independent of the position, the intensity of all coating reflections is not homogeneously distributed along a powder ring, indicating that all coatings are textured.

The (111) and (200) pole figures of the coatings are presented in Fig. 9.8 and Fig. 9.9. Their intensity is normalized to the maximum intensity of the (111) peak at each position.

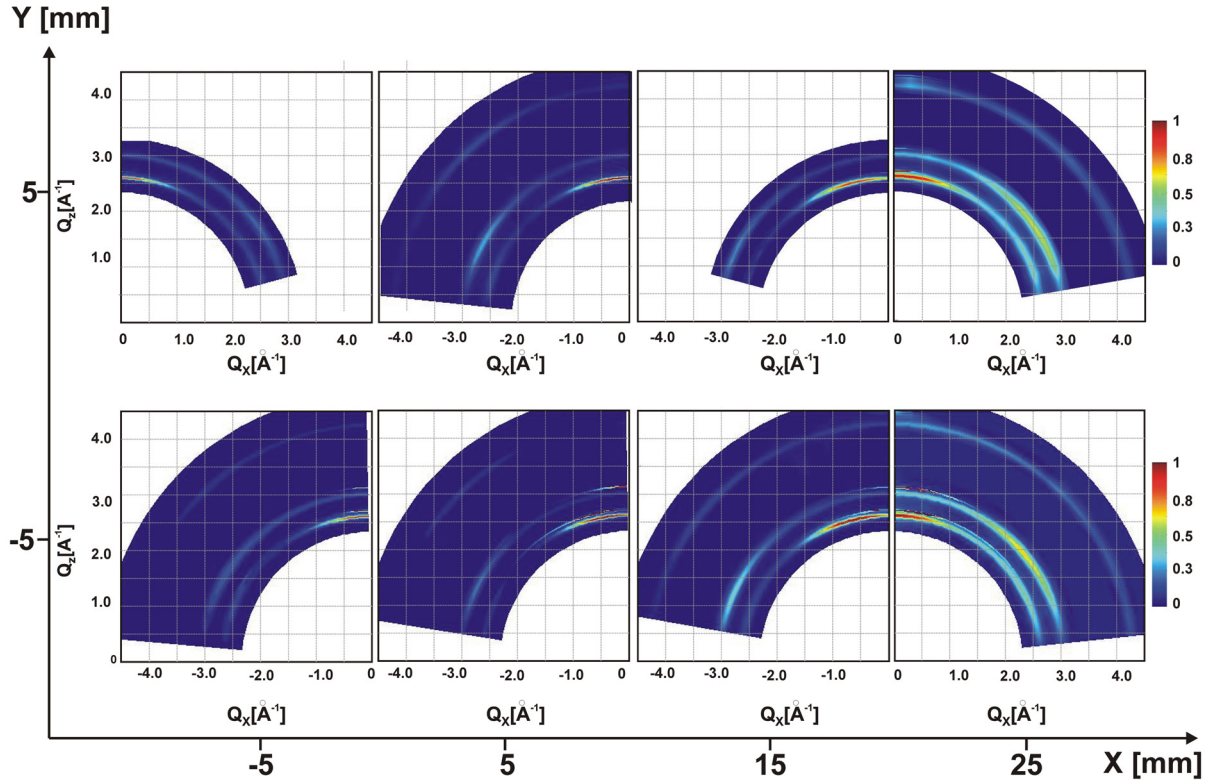


Figure 9.7: Strain map of coatings on Si as a function of position below the target.

As shown in Fig. 9.8, the (111) pole figures of all coatings have a (111) peak attributed to the (111) texture. The (111) peak intensity for coatings at $X < -10$ mm is not distributed symmetrically.

The FWHM of the (111) peak is related to the orientation distribution of the (111) texture. FWHM of the (111) peak is narrower in the range of $-10 \text{ mm} < X < 20 \text{ mm}$ than for the other positions.

The (200) pole figures as a function of position are shown in Fig. 9.9. The expected (200) ring of the isotropic (111) texture is indicated as white dashed circle.

For $X < -10$ mm, the intensity is not distributed homogeneously along the (200) ring. This is consistent with asymmetric intensity distribution of the (111) peak. The (200) ring for $X = -5$ mm is only visible at an enhance intensity scale as shown in Fig. 9.10 (b). In the range of $0 < X < 20$ mm, the (200) ring is only observed partially because (1) part of the (200) ring is not in our measurement range and (2) the intensity is not corrected for geometry effects. For $X = 25$ mm, a broad (200) ring is observed. This is

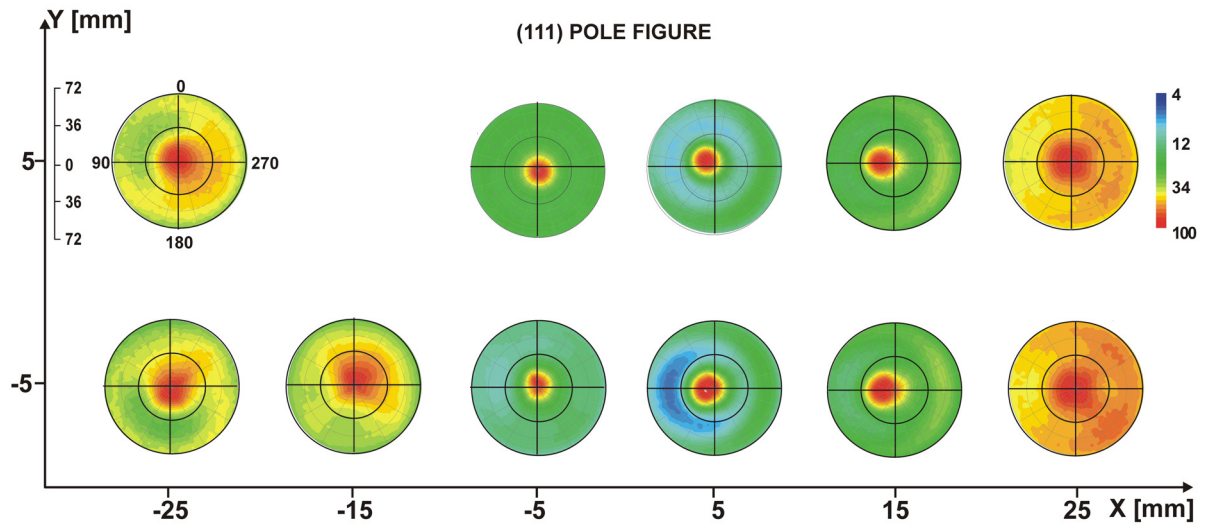


Figure 9.8: (111) Pole figures of coatings on Si as a function of position below the target.

consistent with the broad (111) peak in the corresponding (111) pole figure.

Figures 9.7, 9.8 and 9.9 show that the strain maps and the pole figures of the first and the second row coatings have a similar intensity distribution. Their correspond radial scans show the same tendency: the peak positions, the relative intensities and the FWHM of the first and the second row coatings are similar (see section 9.2).

The strain map and the pole figures analysis indicates that all coatings on Si have the isotropic (111) texture. However, the radial scan also indicates existence of other types of textures. In order to investigate the texture superposition and to determine the average texture direction, the same fitting procedures were performed for coatings on Si as for coatings on cemented carbide.

Because the strain maps and pole figures of the first and the second row coatings are identical, the texture superposition of the coatings is described for the second row coatings only. The FWHM of the (111) peaks for $X < -10$ mm varies as a function of ϕ . This means the fitting should be performed for all ϕ directions. For this fitting complexity and because the strain maps were not measured for $X < -10$ mm, the fitting was only performed for $X > -10$ mm (it is shown in the next section that (220) coexisting texture can only be identified from the (220) strain map).

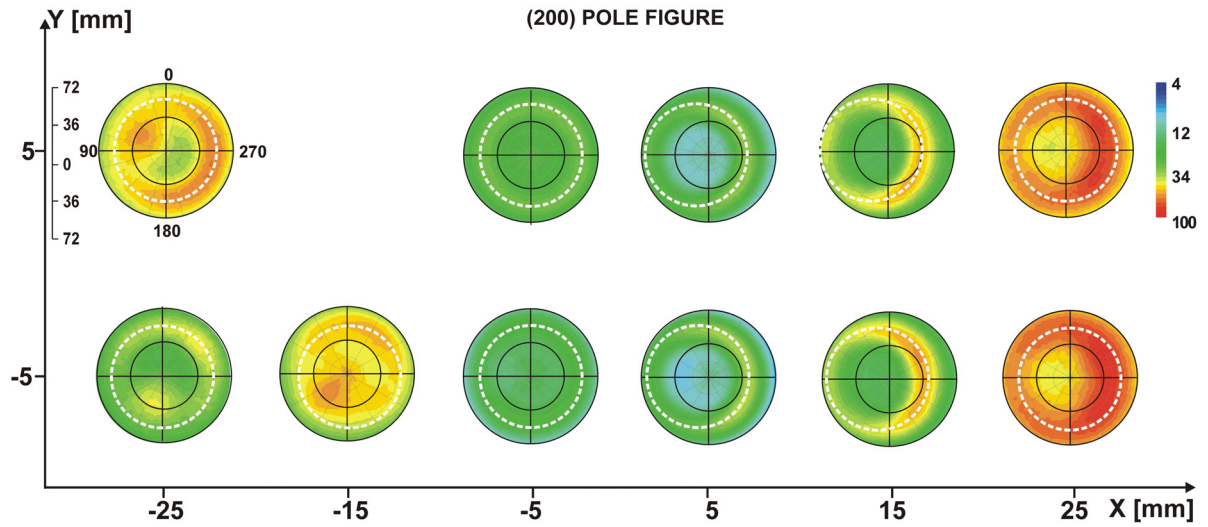


Figure 9.9: (200) Pole figures of coatings on Si as a function of position below the target.

9.3.1 Texture Superposition for $X = -5$ mm

The (111) pole figure, the enhanced (200) pole figure and the enhanced (220) strain map are presented in Fig. 9.10 (a) to (c). The enhanced (200) pole figure shows that the intensity of the (200) ring attributed to the (111) texture is inhomogeneously distributed. The gray circle indicates the section of the (200) ring which has a weaker intensity. However because it does not indicate a three-fold intensity distribution, we conclude that this inhomogeneous intensity distribution is not attributed to the in-plane orientation of the (111) texture. A small missalignment of the sample during the measurement might explain this inhomogeneous intensity distribution of the (200) ring.

Coexistence textures which contribute to the pole figures are: (1) the peak close to $\Psi \approx 0^\circ$ of the (200) pole figure indicates the (200) texture, and (2) the peak close to $\Psi \approx 0^\circ$ of the (220) strain map (guided by dashed green circle) is attributed to the (220) texture.

Thus for coating at this position, the (111) texture is superimposed with the (200) and the (220) textures. The schematic (111), (200) and (220) pole figures for this texture superposition are given in Fig. 9.10 (d) to (f). The red, brown and green lines represent the intensity distribution of the (111), the (200) and the (220) textures respectively.

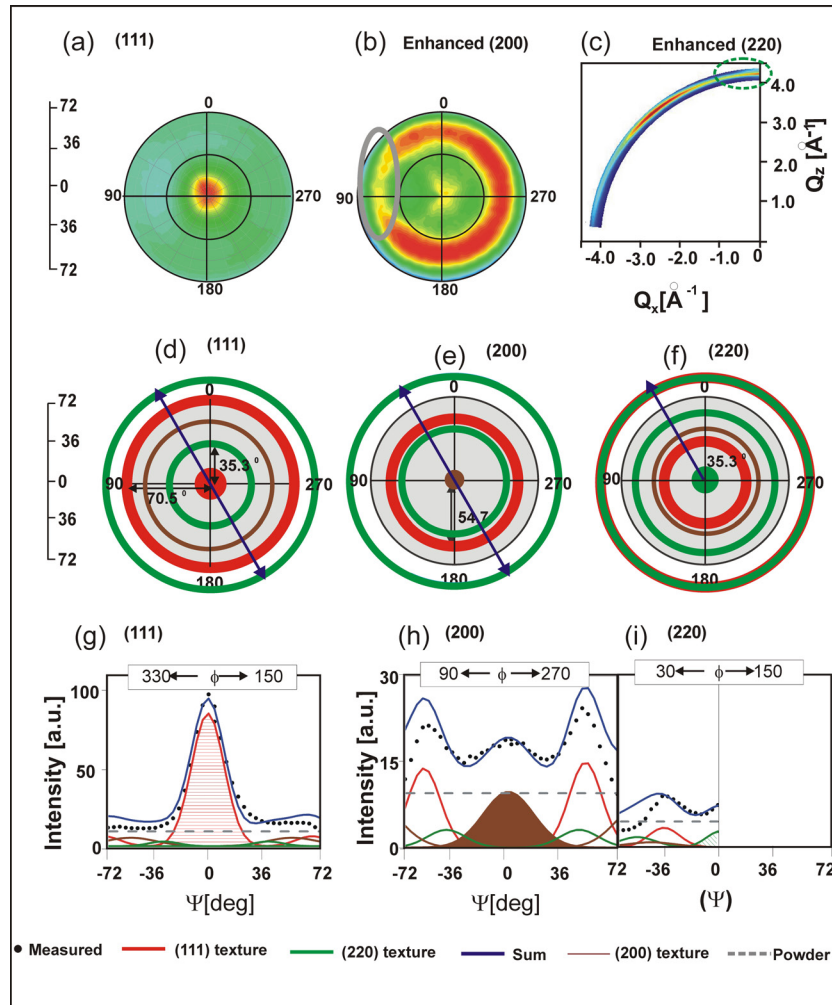


Figure 9.10: Measured (a) (111) pole figure, (b) enhanced (200) pole figure and (c) enhanced (220) strain map. Schematic (d) (111), (e) (200) and (f) (220) pole figures for a superposition of (111), (200) and (220) textures. The (g) (111), (h) the (200), and (i) the (220) line scans are fitted by calculated peak positions assuming cubic symmetry and texture superposition.

For confirmation of the texture superposition, the line scans of the (111) pole figure, the (200) pole figure and the (220) strain map are then fitted with the calculated peak positions for three textures assuming a cubic symmetry. The blue arrows in Fig. 9.10 (d) to (f) are the cut directions of the line scans. The fit results are presented in Fig. 9.10 (g) to (i). The sum of the fitted peaks (blue lines) at lower Ψ is adjusted to the measured intensity while at higher Ψ the sum is adjusted larger than measured intensity to account for geometry and absorption effects.

We found that the intensity distribution can only be fitted by a superposition of the (111), the (200), the (220) textures and additionally crystallites with random, powder-like distribution (gray dashed line).

The average orientation and the distribution of each type of texture are determined from the region where (1) the indication of a specific type of texture is strong and (2) the superposition of this specific texture and other textures only weak. The red, brown and green areas in Fig. 9.10 (g) to (i) were used to determine Ψ_{111} , Ψ_{200} , Ψ_{220} and σ_{111} , σ_{200} , σ_{220} .

Ψ_{220} and σ_{220} are determined from the strain map which was not measured in the complete range of Ψ and covers the peak only partially. Therefore, their fitting error is larger than for other textures. For all textures, the fitted values of Ψ_{hkl} and σ_{hkl} are shown in Fig. 9.14 (b) and (c).

9.3.2 Texture Superposition for $X = 5$ mm

The (111) and the (200) pole figures and the enhanced (220) strain map of the coating at $X = 5$ mm are presented in Fig. 9.11 (a) to (c). It is shown that the (111) peak attributed to the (111) texture is tilted relative to center of the pole (see Fig. 9.11 (a)). Therefore the (200) ring is shifted toward this (111) tilt angle. The red dashed line in Fig. 9.11 (b) corresponds to the expected (200) ring of the (111) texture. Because the data is not corrected for the geometry and the absorption effects, one half of the tilted (200) ring has stronger intensity than the other half ring.

The existence of the (220) texture is indicated by the intensity at $\Psi \approx 0^\circ$ of the (220) strain map (green dashed line in Fig. 9.11 (c)).

The (200) line scan shows a weak peak close to $\Psi \approx 0^\circ$ (see Fig. 9.11 (h)). This peak is attributed to the (200) texture. The line scan of all reflections can only be fitted with a superposition of the (111), the (200) and the (220) textures as well as powder crystallites. Type of texture of this coating is same as for $X = -5$ mm, but their Ψ_{111} are different (see Fig. 9.14 (b)).

The schematic (111), (200) and (220) pole figures due to a superposition of the tilted (111), the (200) and the (220) textures are given in Fig. 9.11 (d) to (f).

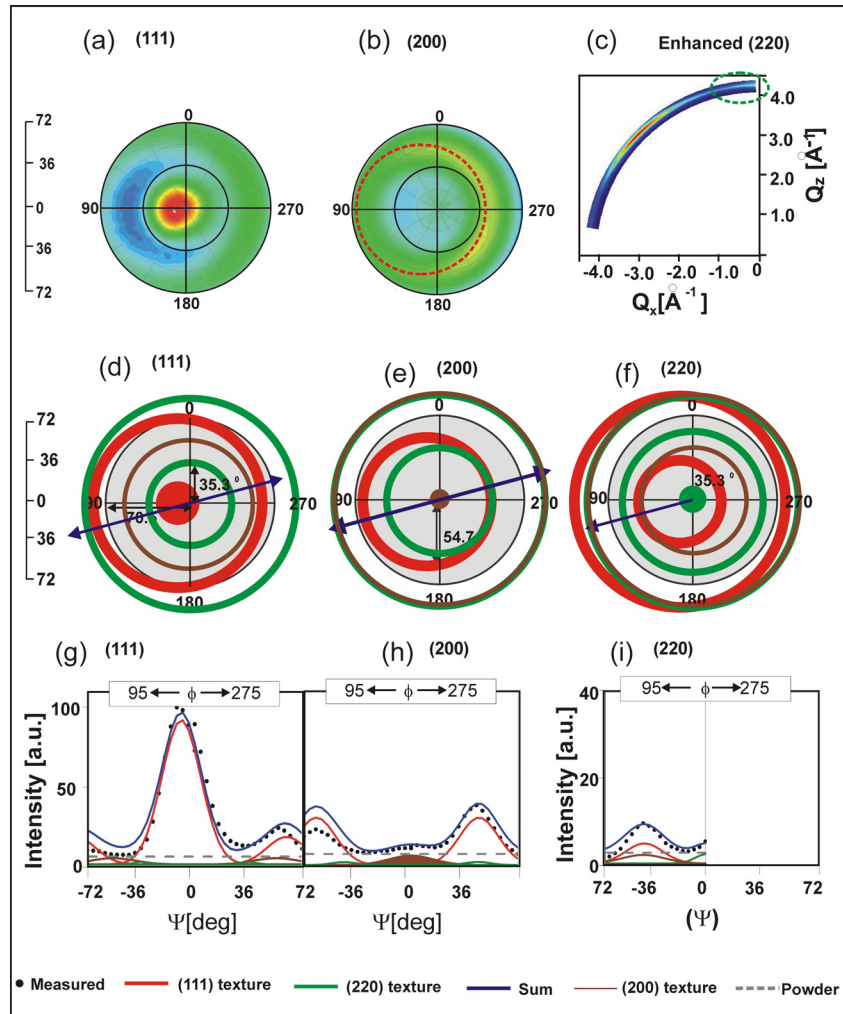


Figure 9.11: Measured (a) (111) pole figure, (b) (200) pole figure and (c) enhanced (220) strain map for $X = 5$ mm. Schematic (d) (111), (e) (200) and (f) (220) pole figures for a superposition of the (111), the (200) and the (220) textures. The (g) (111), (h) the (200), and (i) the (220) line scans are fitted by calculated peak positions assuming cubic symmetry and texture superposition.

9.3.3 Texture Superposition for $X = 15$ mm

The (111) and the (200) pole figures and the enhanced (220) strain map of the coating at $X = 15$ mm are presented in Fig. 9.12 (a) to (c). The main features of the pole figures and the strain map are (1) the tilted (111) peak in the (111) pole figure is attributed to the tilted (111) texture, (2) a segment of the (200) ring has a weaker intensity than the remaining ring because the data is not corrected for geometry and the absorption effects.

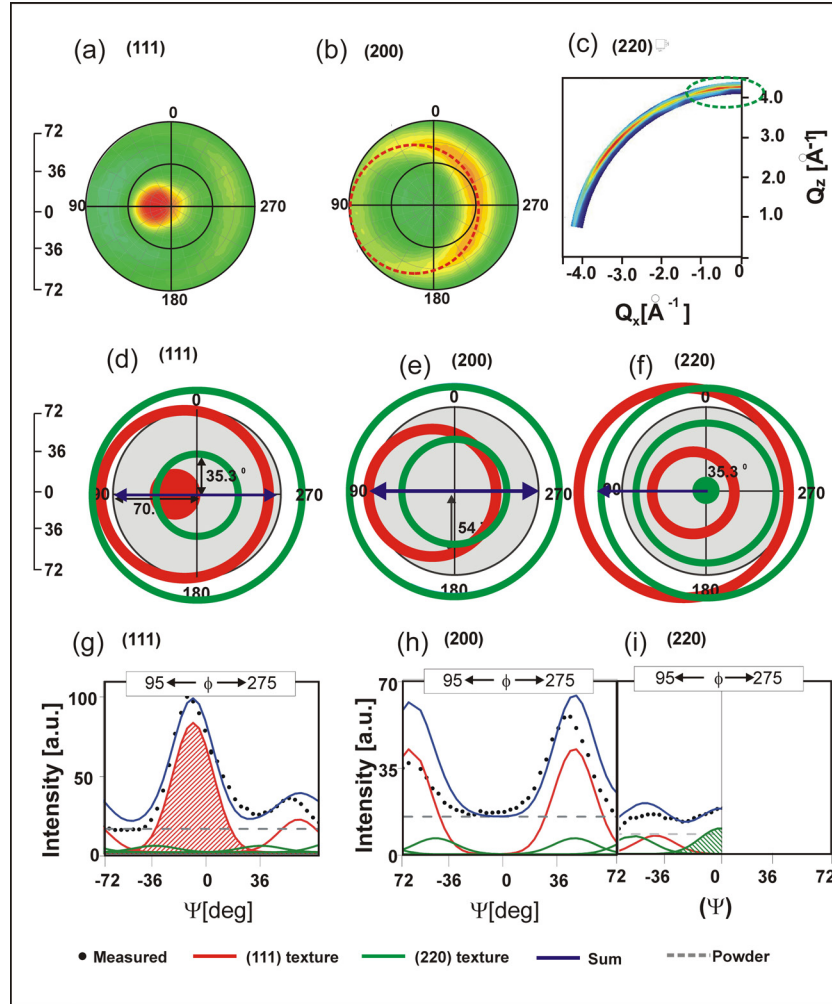


Figure 9.12: Measured (a) (111) pole figure, (b) (200) pole figure and (c) enhanced (220) strain map for $X = 15$ mm. Schematic (d) (111), (e) (200) and (f) (220) pole figures for a superposition of the (111) and the (220) textures. The (g) (111), (h) the (200), and (i) the (220) line scans are fitted by calculated peak positions assuming cubic symmetry and texture superposition.

Also part of the ring is expected to be outside of our measurement range and (3) the intensity distribution of the (220) strain map at $\Psi \approx 0^\circ$ indicates coexistence (220) texture.

The line scan of all reflections can only be fitted with a superposition of the (111) and (220) textures as well as powder crystallites. The (200) texture is not found for this coating as it was found for coatings at $X < 10$ mm. The line scans indicate that the con-

tribution of random, powder-like distribution is stronger in this coating than for coatings at $X < 10$ mm.

Figure 9.12 (d) to (f) present the expected (111), (200) and (220) pole figures for a superposition of the tilted (111) and the (220) texture.

9.3.4 Texture Superposition for $X = 25$ mm

The (111) and the (200) pole figures and the enhanced (220) strain map of coating at $X = 25$ mm are presented in Fig. 9.13 (a) to (c). The (111) pole figure has a broad peak close to $\Psi \approx 0^\circ$, and the intensity as a function of Ψ does not decrease as fast as the intensity of the (111) pole figure at other positions. This might indicate that powder contribution in this coating is more significant than for the other coatings.

The intensity distribution close to $\Psi \approx 0^\circ$ of the (220) strain map (green dashed circle in Fig. 9.13 (c)) is attributed to the (220) texture. The schematic pole figures and the fitting results of the line scan of all reflections are presented in Fig. 9.13 (d) to (f).

The coating at this position has a similar feature as for the coating at $X = 15$ mm, which is: the intensity distribution can be explained by a superposition of the (111) texture, the (220) texture and the powder contribution. The main differences between them are their Ψ_{111} and σ_{111} (see next section).

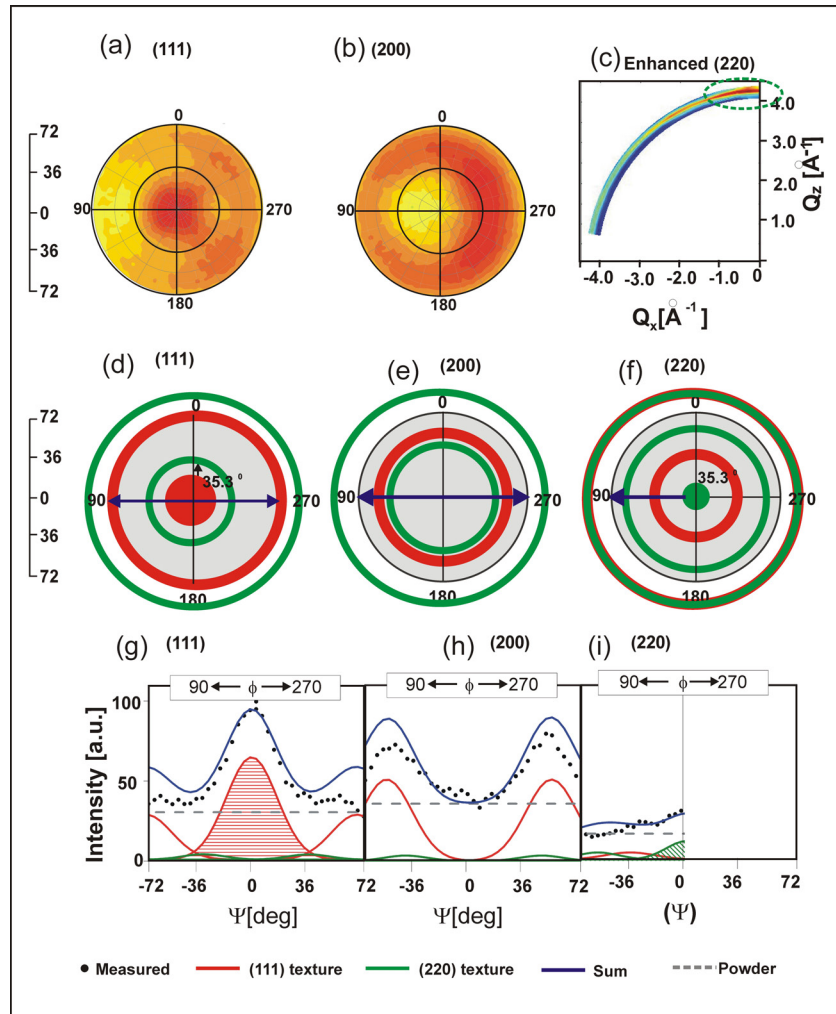


Figure 9.13: Measured (a) (111) and (b) (200) pole figures and (c) enhanced (220) strain map for $X = 25$ mm. Schematic (d) (111), (e) (200) and (f) (220) pole figures for a superposition of the (111) and the (220) textures. The (g) (111), (h) the (200), and (i) the (220) line scans are fitted by calculated peak positions assuming cubic symmetry and texture superposition.

9.3.5 Main Results

The texture of the coatings on Si at selected sample positions have been analyzed from pole figures and strain maps. The intensity distribution of strain maps and pole figures for the first and the second row coatings are similar. This is consistent with our observation for the radial scans. The fitting of the (111), the (200) and the (220) line scans was performed for the second row coatings.

Qualitatively, the texture evolution as a function of sample position is summarized in Fig. 9.14 (a). The colors of the spheres indicate different types of intensity distribution: red, green, brown and gray represent the (111), the (220), the (200) textures and the powder crystallites. The sphere size represents qualitatively the intensity ratio of different textures.

All coatings have the dominant (111) texture which is superimposed with the (220) texture and powder crystallites. The (220) texture and powder contributions are stronger at higher X, i.e. in direction of decreasing Vanadium and Carbon concentration. For coatings at $X < 10$ mm, the (111) texture is additionally superimposed by the (200) textures.

The average orientation Ψ_{hkl} as a function of position is shown in Fig. 9.14 (b). The negative values correspond to the direction of the VC target. For coatings in the range of $-10 \text{ mm} < X < 20 \text{ mm}$, Ψ_{111} is tilted in direction of the VC target. For $X = 25 \text{ mm}$, Ψ_{111} is close to 0° . This position corresponds to the position below the erosion area of the AlN target. For all coatings, Ψ_{200} and Ψ_{220} are close to $\Psi = 0^\circ$. The relation between the average orientation and the position below the target will be discussed in section 12.

σ_{111} increase with increasing X, in direction of the AlN target. For other textures, the variation of σ_{200} and σ_{220} as a function of position can be explained by the fitting error.

The radial scans as described in section 9.2 indicate the (111) texture. However, it is shown in this section that it is not enough to conclude on the texture of the coatings from the radial scans only: (1) the texture superposition cannot be analysed in detailed from the radial scan, (2) the Ψ_{hkl} and σ_{hkl} cannot be determined from the radial scan, and (3) depending on the Ψ_{hkl} , σ_{hkl} and Q_r direction, the wrong conclusions might be made.

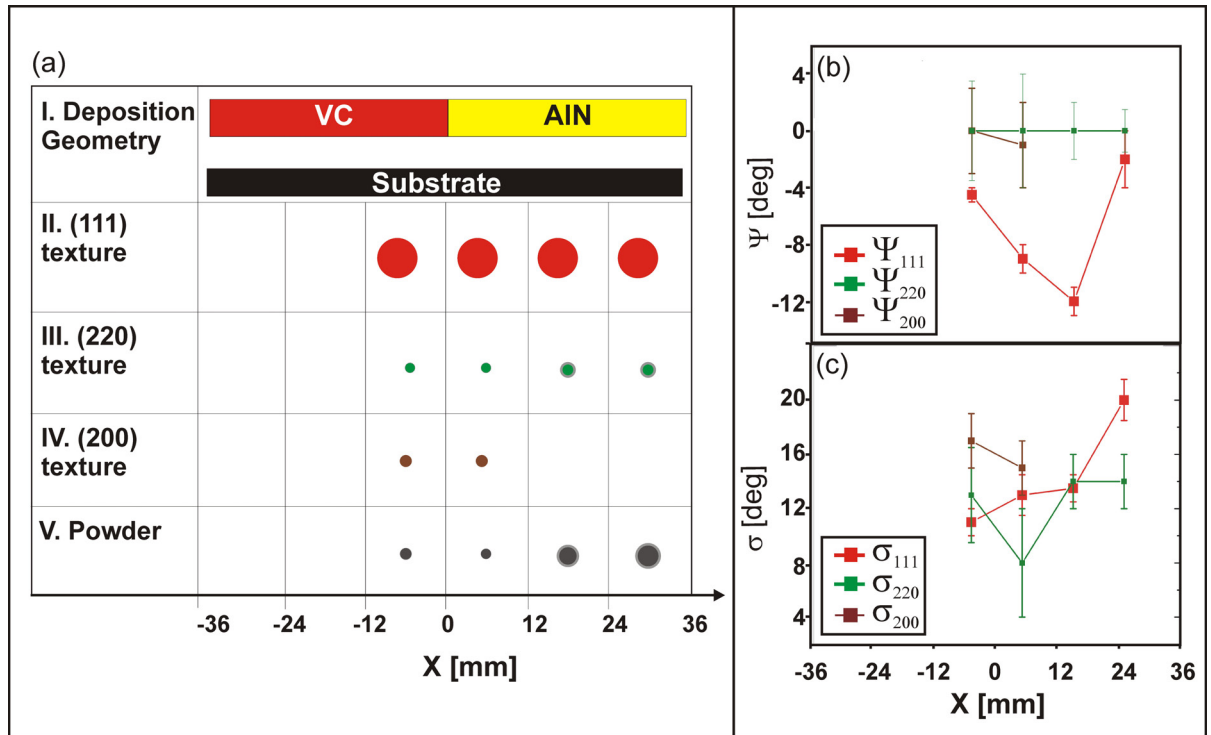


Figure 9.14: (a) Qualitative summary of crystallographic orientation of the coatings as a function of position below the target X, fitted (b) average orientation Ψ_{hkl} and (c) distribution σ_{hkl} of each type of texture.

9.4 Influence of Texture Superposition on d_{hkl}

The strain map measures not only the intensity distribution but also the peak shift as a function of Ψ . The radial peak positions of the (111), the (200), and the (220) reflections as a function of Ψ have been fitted by the Fityk software. The lattice spacing is then calculated by inserting the fitted peak position into the Bragg's law.

Figure 9.15 shows evolution of d_{111} , d_{200} and d_{220} as a function of Ψ for the second row coatings ($Y = -5$ mm). Independent of the coating positions, d_{hkl} of all reflections decrease monotonously with increasing Ψ . This tendency is different from what is found for coatings on cemented carbide (see Fig. 8.15 and Fig. 8.16).

For coatings on cemented carbide, the non-monotonous decrease of the lattice spacing as a function of Ψ might indicate that the lattice constant of the (111) texture crystallites is different from the lattice constant of other type of textures (see section 8.3). Thus depending on how each type of texture is superimposed with other coexisting textures,

d_{hkl} of the coatings on cemented carbide is not decrease monotonously. The monotonous decrease of d_{hkl} as a function of Ψ for coatings on Si might indicate that strain of all type of crystallites of this series of coatings is similar.

In the following, the influence of the texture superposition on the d_{hkl} vs Ψ plot is analyzed for the coating on Si at $X = 15$. Figure 9.16 (a) to (c) shows the analysis of the texture superposition as performed in section 9.3.3. The corresponding lattice spacing is shown in Fig. 9.16 (d) to (f).

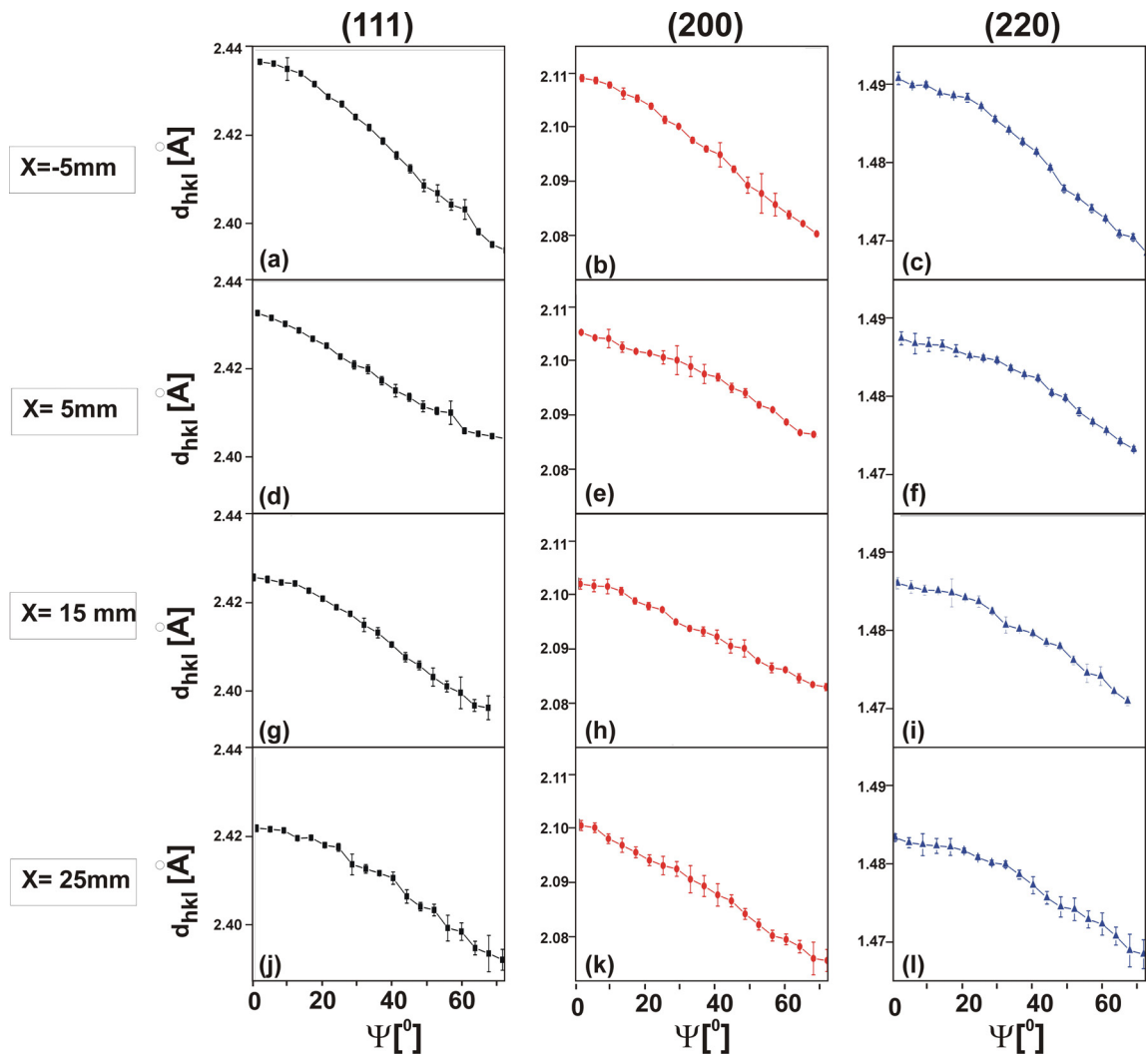


Figure 9.15: d_{hkl} vs Ψ plot for the (111), the (200) and the (220) rings at selected coating positions.

The intensity distribution of pole figures and strain map for this position can be explained by a superposition of the (111) texture, the (220) texture and powder. For the (111) reflection up to $\Psi \approx 36^\circ$, the measured intensity attributed to the (111) texture is dominant. Above $\Psi = 36^\circ$, the intensity attributed to the powder crystallites is dominant.

The same procedures were performed for the (200) and the (220) textures. The results are presented in Fig. 9.16 (b) and (c). As indicated in the figure, the background color corresponds to a specific type of texture which dominating the measured intensity. The white regions in the (200) and (220) reflections indicate that the measured intensity is most likely attributed to the average contribution of all textures and powder.

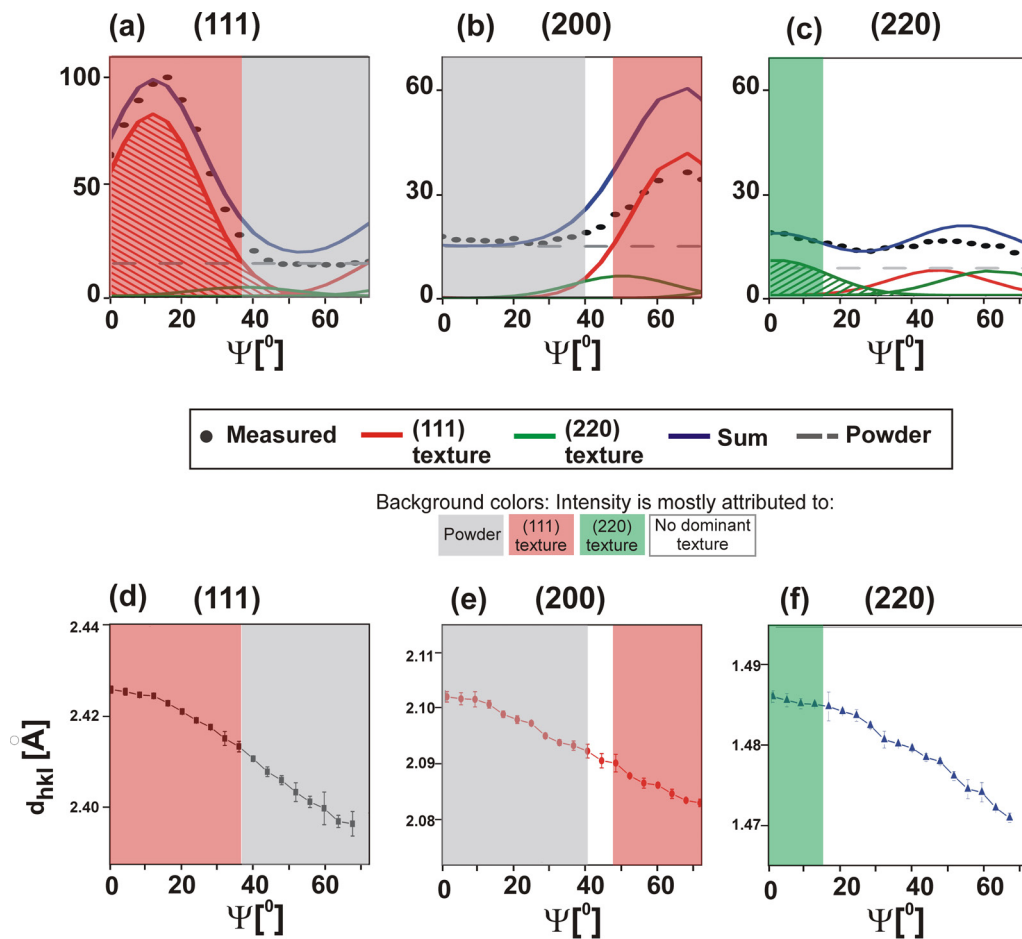


Figure 9.16: Texture superposition of (a) the (111), (b) the (200) and (c) the (220) reflection for sample at $X = 15$ mm. (d) to (f): Corresponding d_{hkl} vs Ψ plots.

Figure 9.16 (a) shows that there is no abrupt change of the lattice spacings from regions dominated by the (111) texture (red background) to the region dominated by the powder crystallites (gray background). The same observation is found for all reflections of all coatings. This is expected if the strain of all crystallites is similar.

10 XAFS Result of the (V,Al)(C,N) Coatings at Vanadium K-edge

The calculated phase diagram shows that depending on the chemical composition, the expected structure of V-Al-C-N coating is face center cubic or hexagonal structure (see section 2.2). The X-Ray Diffraction profile reveals that all coatings have fcc structure (section 8 and 9). However, since all coatings are textured, it is difficult to determine from their relative intensity whether this fcc structure is attributed to fcc-VC or fcc (V,Al)(C,N). Moreover, the XRD is not very sensitive to amorphous material or to very small hexagonal crystallites.

X-Ray Absorption Fine Structure Spectroscopy (XAFS) is sensitive to the local environment of an absorbing atom for both crystalline and amorphous samples. The XAFS spectra of selected coatings at the Vanadium K-edge have been measured at ANKA. The aims of this measurement are to: (1) investigate the local environment of Vanadium, (2) determine the atomic distance of Vanadium and neighboring atoms, and (3) investigate the existence of a very small hexagonal crystallites. The results are presented below.

10.1 XANES at the Vanadium K-edge

Both series of V-Al-C-N coatings deposited on cemented carbide and on Si(001) exhibit chemical composition and thickness variations as a function of position below the target. In order to investigate the influence of local Vanadium environment and sample thickness on the XANES spectra, three reference spectra were measured, i.e. VC thin coating, VN thin coating and VC target. These reference spectra are used in order to understand the XANES spectra of the V-Al-C-N coatings.

Figure 10.1 presents the XANES of: (a) the VC and VN coatings, (b) the VC coating and VC target, (c) the V-Al-C-N coatings on cemented carbide and (d) two V-Al-C-N coatings on Si(001).

Figure 10.1 (a) shows the XANES regions of the VC and the VN thin coatings (both have thickness in μm range). The XANES spectra of both compounds have a similar feature, i.e. the weak pre-edge peaks are observed at ≈ 5470 eV (see the gray line). The

same observation was reported by J. Wong et al., i.e. the pre-edge peak of VC is located at 5470.4 eV and the pre-edge peak of VN is located at 5469.8 eV [58]. The similar feature of VC and VN are related to the fact that both compounds have fcc structure where Vanadium has an octahedral coordination with Carbon (or Nitrogen).

The height of the pre-edge peak for VC coating is higher than for VN coating. The minimum of the pre-edge peak of VC coating is located at higher energy than minimum of the pre-edge peak of VN coating (see the green line A). A characteristic feature of VN is a weak shoulder (see the gray dashed circle in this figure) which is not observed in VC thin coating (as also reported by J. Wong et al.). These differences might be attributed to the differences in their structure parameters e.g. the atomic distance, the electronegativity and the formal charge differences.

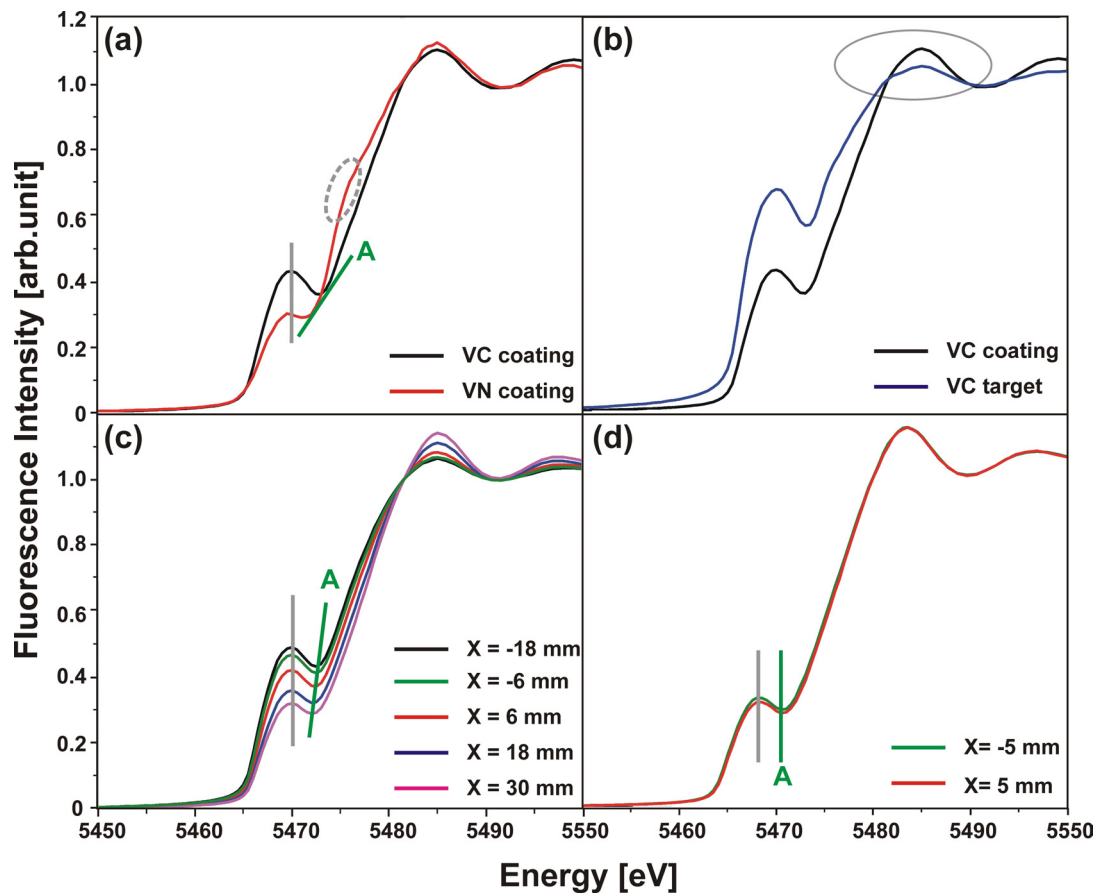


Figure 10.1: XANES spectra of (a) VC and VN coatings, (b) VC coating and VC target, (c) V-Al-C-N coatings on cemented carbide, and (d) two V-Al-C-N coatings on Si(001).

In order to study the influence of the thickness, the XANES of VC compound at different thickness were measured. The spectra are presented in Fig. 10.1 (b). The pre-edge intensity of the VC target (mm thick) is stronger than the pre-edge intensity of the VC coating (μm thick). The reverse effect is observed for the first peak after the edge (see the gray circle in this figure): the intensity of this peak is higher for the VC coating than for the VC target. We have shown here that the peak intensity might not only be related to the local structure [58], but also to the thickness.

Figure 10.1 (c) and (d) present the XANES spectra of the V-Al-C-N coatings on cemented carbide and on Si at selected positions. The weak pre-edge peak are observed in all coatings. This is a strong indication that Vanadium has an octahedral environment such as in fcc structure. For a similar compound as our material i.e. TiAlN, the existence of Ti in a distorted four-fold coordination e.g. in hexagonal wurtzite structure increases the pre-edge intensity [72, 73]. Thus within the detection limit of the measurement (500 ppm), the pre-edge intensity indicates that all coatings have fcc structure. The hexagonal structure does not seem to be coexisting.

The pre-edge peak of the coatings on cemented carbide is found at $E \approx 5470$ eV while for coatings on Si, the pre-edge is found at $E \approx 5469.5$ eV (see the gray lines in the figure). This difference is smaller than the energy resolution of the XAS beamline ($\Delta E/E$ is 1.8 eV at 9 keV). These measured pre-edge positions are located close to expected VC or VN pre-edge peak in fcc structure.

For coatings on cemented carbide, the position of the minimum of the pre-edge peak (line A in Fig. 10.1 (c)) is slightly shifted to lower energy with increasing nitrogen concentration (from $X = -18$ mm to $X = 30$ mm). This might indicate existence of both V-C and V-N bonds in the coatings.

At selected position of coatings on Si, the shifting of the minimum of the pre-edge peak (line A in Fig. 10.1 (d)) is not observed. This might be related to the fact that for the selected positions ($X = -5$ mm and $X = 5$ mm), the difference in chemical composition and thickness variation is very small.

10.2 Atomic Distance

The Fourier transformation of the EXAFS region of coatings on cemented carbide is shown in Fig. 10.2 (a). The spectra are presented without phase shift correction. In this figure, two peaks attributed to the atomic distance of the first and the second shell are observed.

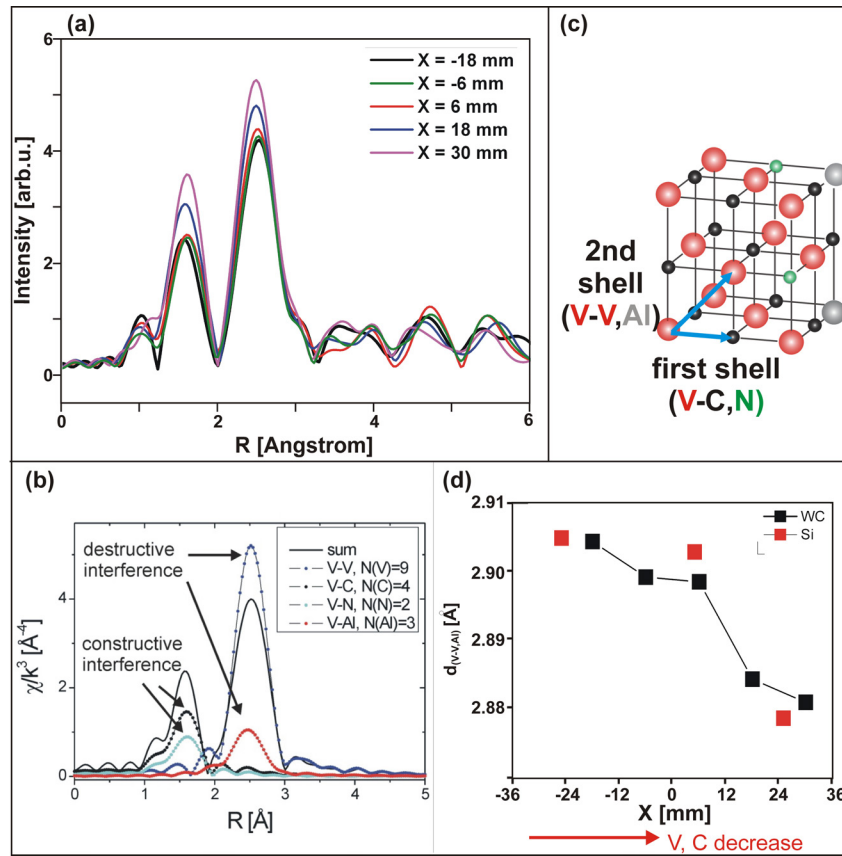


Figure 10.2: (a) Fourier transformation of EXAFS spectra for coatings on cemented carbide (spectra are presented without phase shift correction), (b) calculated EXAFS amplitude assuming fcc (V,Al)(C,N) (c) a mixed (V,Al)(C,N) in fcc structure, and (d) atomic distance of V-(V,Al).

The spectra were fitted with three models by Dr. Stefan Mangold and Dr. Baerbel Krause from ANKA which are: (1) a mixed fcc V-Al-C-N crystal, (2) hexagonal close packed structure, and (3) a mixed fcc structure with interstitial carbon. It is found that the spectra fit best with a mixed fcc crystal. They cannot be fitted by the other two models.

Figure 10.2 (b) shows the calculated EXAFS amplitude of fcc (V,Al)(C,N) where the first peak corresponds to the first shell of the unit cell, i.e. Vanadium in octahedral coordination with 4 Carbon (see the black dotted line) and 2 Nitrogen (see the light blue dotted line). The second peak corresponds to the second shell in the unit cell, i.e. average distance of nine V-V (see the dark blue dotted line) and three V-Al (see the red dotted

line). The first and second shell of the fcc (V,Al)(C,N) crystal are indicated in Fig. 10.2 (c).

It is shown in the calculated EXAFS amplitude that the amplitude of the first and second peaks is influenced by the chemical composition. The substitution of Carbon atom by Nitrogen increases EXAFS amplitude (constructive interference) while the substitution of Vanadium by Aluminum decreases slightly the EXAFS amplitude (destructive interference).

For all coatings, the amplitude of the EXAFS spectra can only be fitted assuming some of the Vanadium is replaced by the Aluminum. This indicates that the fcc structure might be attributed to the fcc-(V,Al)(C,N) and not to the fcc-VC.

The fitted atomic distance of V-(V,Al) for coating on cemented carbide and on Si are presented in Fig. 10.2 (d). It is shown that independent of the substrate, the atomic distance decreases with increasing Al and N concentration as expected for a mixed crystal.

10.3 Main Results

The XANES and EXAFS spectra of selected coatings have been analyzed. The intensity of the pre-edge of the XANES spectra of all coatings indicates (a) the Vanadium is in octahedral coordination and (2) within the detection limit, no hcp is observed. These results are consistent with the XRD analysis which reveals that all coatings have fcc structure. The direct V-C and V-N bonds are also indicated from the XANES.

The Fourier transformation of the EXAFS spectra fits best with fcc (V,Al)(C,N) model. The fitted atomic distance decreases with increasing Al content.

11 In-Plane Compressive Stress of the V-Al-C-N Hard Coatings

The radial peak positions as a function of Ψ measured in the strain map geometry have been fitted for both series of the coatings. Independent of the (hkl) reflections, the lattice spacings decrease with increasing tilt angle Ψ (see section 8.3 and 9.4). This indicates that all coatings are compressed laterally.

In this chapter, we present our analysis results of: (1) the influence of the in-plane stress on the fcc unit cell and (2) the residual stress determination using the $\sin^2\Psi$ method.

11.1 Distorted fcc Unit Cell

It was found that the dominant texture of all coatings is the (111) texture without in-plane orientation. The coexistence textures are much weaker than the (111) texture. Therefore in this section the lattice parameters are only fitted for the (111) crystallites without in-plane orientation. The lattice parameter is determined from the peak position of the (111), the (200) and the (220) reflections attributed to this texture as described in the following.

Figure 11.1 (a) shows a strain map covering the $\{111\}$, $\{200\}$ and $\{220\}$ reflections for a coating on cemented carbide at $X = 6$ mm. The radial peak positions of the (111) reflection is taken at Ψ_{111} corresponding to the average orientation of the (111) texture without in-plane orientation. The radial peak positions of the other two reflections are taken at Ψ determined from cubic symmetry (see section 4). The peak positions are then fitted using two models: (1) the perfect fcc unit cell and (2) the distorted fcc unit cell.

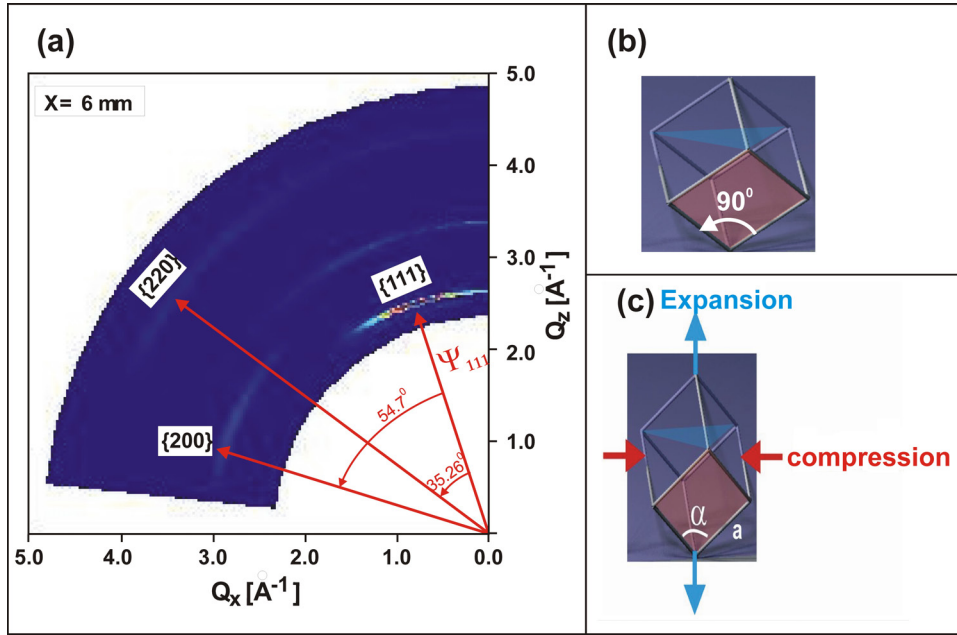


Figure 11.1: (a) Strain map for coatings on cemented carbide at $X = 6 \text{ mm}$, (b) schematic (111) cubic unit cell, and (c) schematic distorted (111) oriented cubic unit cell.

A schematic of the perfect (111) cubic unit cell is presented in Fig. 11.1 (b). For perfect cubic model, the lattice parameter a is calculated by inserting d_{111} into Eq. 4.12. The peak positions of the other reflections are then calculated using this lattice parameter. In order to evaluate if the perfect fcc unit cell model can explain the peak position of all reflections or not, the measured peaks are compared to the calculated peaks.

As an example, Fig. 11.2 (a) to (c) show the measured and calculated (111), (200) and (220) reflections on cemented carbide at $X = 18 \text{ mm}$ assuming perfect cubic unit cell. The lattice parameter determined from the (111) reflection is 4.192 Angström. The measured (111) peak position fits well with the calculated peak position as expected. The measured peak positions of other two reflections are located at higher 2θ angle relative to the calculated peak positions. This indicates that the peak positions cannot be explained by a perfect cubic unit cell model.

Assuming isotropic lateral compressive stress, the (111) oriented fcc unit cell is distorted to the rhombohedral unit cell (see Fig. 11.1 (c)). In this distorted unit cell, the angle α is compressed to less than 90° and all edges of the unit cell have the same length a .

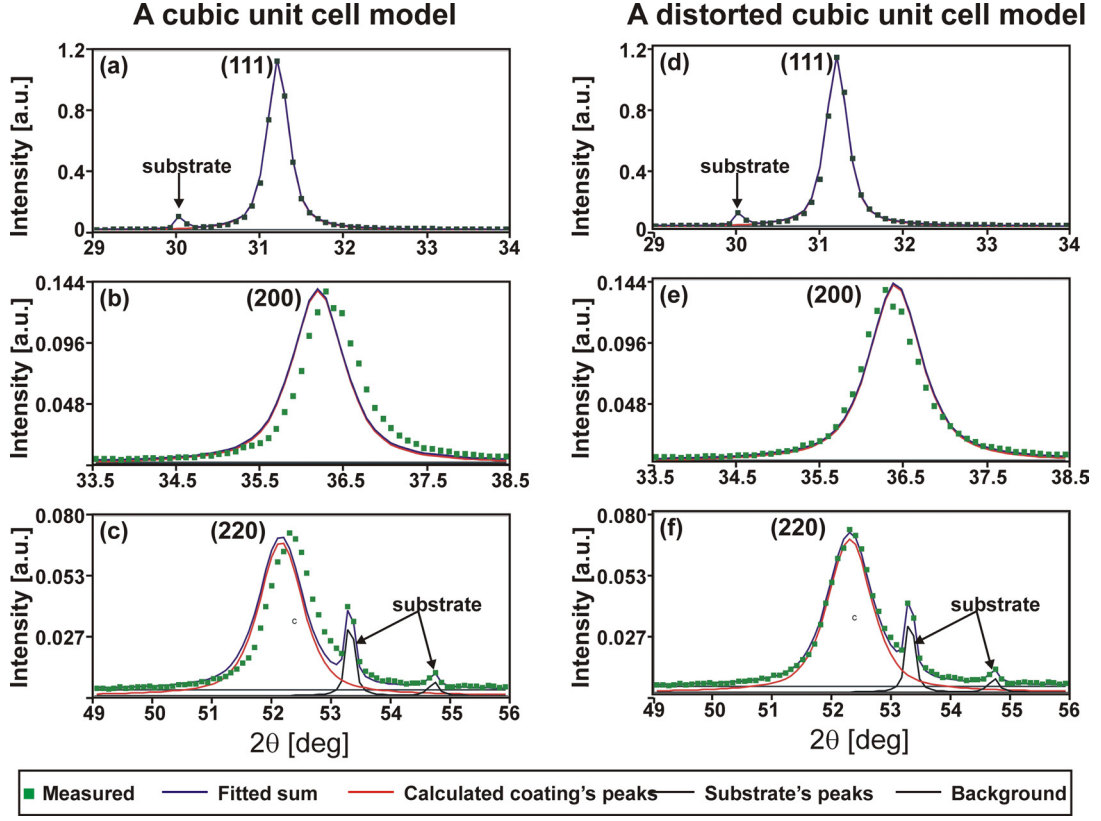


Figure 11.2: Fitting of the coating reflections on cemented carbide at $X = 18$ mm assuming (a) to (c): a cubic unit cell and (d) to (f): a distorted cubic unit cell.

The relation between lattice spacing, lattice parameter and α of a rhombohedral unit cell is given in Eq. 4.9. The calculated and measured reflections for a coating on cemented carbide at $X = 18$ mm assuming a rhombohedral unit cell are presented in Fig. 11.2 (d) to (f). The difference between calculated and measured reflections for this sample are within the experimental error.

All other coatings both on cemented carbide and on Si show the same tendency as observed for the coating on cemented carbide at $X = 18$ mm. Their peak positions can be explained better with a distorted fcc unit cell than a perfect cubic unit cell model. As an example, the calculated and measured reflections of a coating on Si at $X = 15$ mm are presented in Fig. 11.3 (a) to (c) for a cubic model and (d) to (f) for a distorted cubic model.

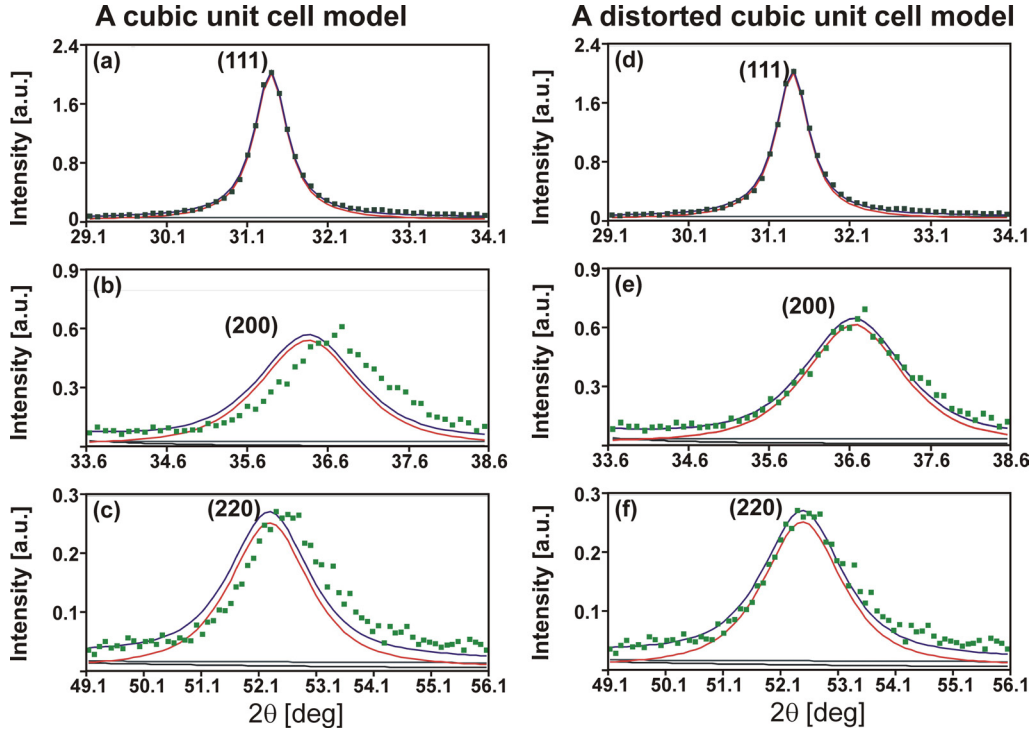


Figure 11.3: Fitting of the coating reflections on Si at $X = 15$ mm assuming (a) to (c): a cubic unit cell, and (d) to (f): a distorted cubic unit cell.

11.1.1 Main Results

Independent of the sample position and the types of substrate, the peak positions of all coating reflections can be fitted by a distorted fcc unit cell. The lattice parameter, the angle α and the unit cell volume of the coatings as a function of position are given in Fig. 11.4 (c) to (e).

As a reminder, the projection of the cemented carbide and Si substrate on the target and their coordinate systems are shown in Fig. 11.4 (a) and (b).

The coatings on Si were deposited in two rows at $Y = 5$ mm and $Y = -5$ mm (see Fig. 11.4 (b)). At the same X , the lattice constant a , the distortion angle α and the unit cell volume V of coatings at both rows are comparable (see Fig. 11.4 (c) to (f)).

Independent of the substrates, the lattice parameter and the unit cell volume of the coatings are smaller with decreasing V content (increasing X).

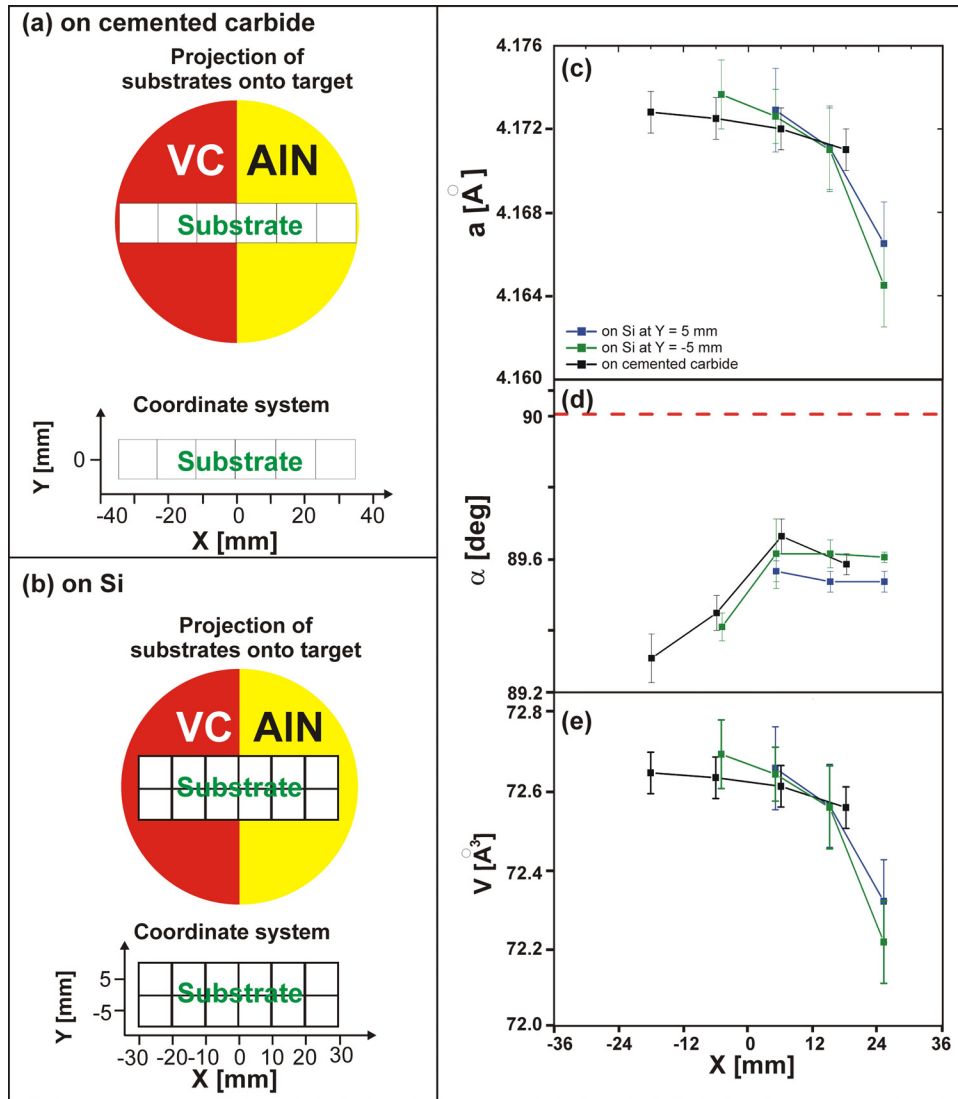


Figure 11.4: Projection of the substrate on the target and coordinate system of the coatings on (a) cemented carbide and (b) Si(001). Variation of the (c) lattice parameter, (d) distorting angle α and (e) volume of the unit cell of coatings on cemented carbide and on Si as a function of position. A red dashed line in (d) at $\alpha = 90^\circ$ corresponds to the α of a perfect cubic unit cell.

The maximum α corresponds to the minimum cubic distortion. The maximum α for coatings on cemented carbide is found at $X = 6$ mm. For coatings on Si, α is constant above $X > 6$.

11.2 Residual Stress as a Function of Position

The residual stress of the coatings is determined by the $\sin^2\Psi$ method (see section 4.7). To determine the residual stress by this method, the coating peak positions have to be measured in a wide Ψ range.

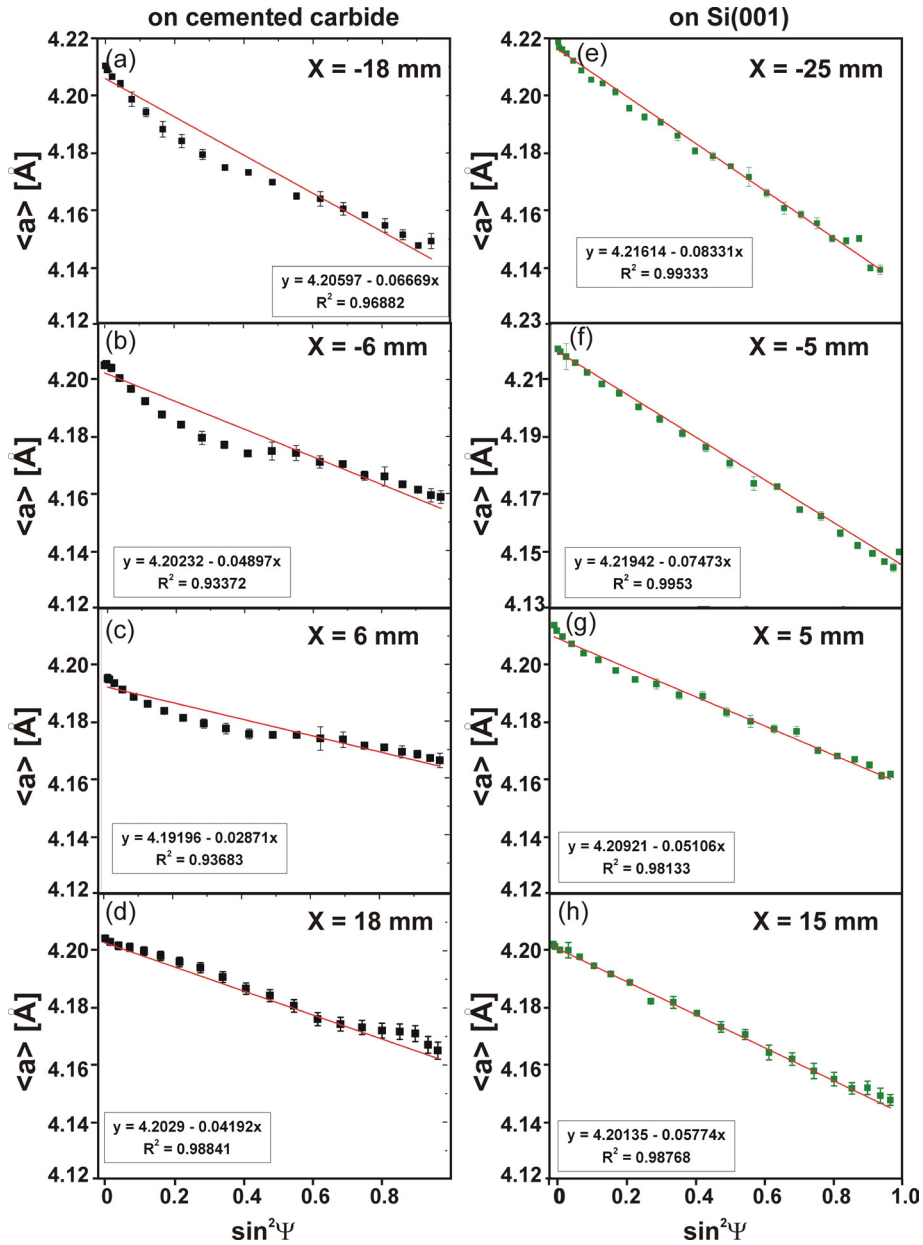


Figure 11.5: $\langle a \rangle$ versus $\sin^2\Psi$ plot of coating on cemented carbide and on Si(001).

Independent of the substrate, all coatings have texture superposition in such a way that it is not possible to attribute the measured peak to one type of texture in the wide range of Ψ . Therefore the residual stress is calculated assuming a weak texture model using Eq. 4.37 (given again below:)

$$\langle a \rangle (\Psi) = a_0 \frac{1 + \nu}{E} \sigma_{\parallel} \sin^2 \Psi - 2a_0 \frac{\nu}{E} \sigma_{\parallel} + a_0$$

where $\langle a \rangle$ is the average lattice spacing of the (111), the (200) and the (220) reflections (calculated using Eq. 4.36), ν is the Poisson ratio, E is the Young modulus and a_0 is the strained-free lattice parameter (see section 4.7.1 to calculate a_0).

Figure 11.5 shows the $\langle a \rangle$ vs. $\sin^2 \Psi$ plots of selected coatings (a) to (d) on cemented carbide and (e) to (h) on Si. The linear fits are presented as red lines. The fitting parameters of each plot are indicated.

For coatings on Si, the average lattice parameter as a function of Ψ follows the linear fit. A deviation of the measured lattice parameter from the linear fit is observed for all coatings on cemented carbide. This deviation might be due to the the (111) crystallites have different lattice parameter from other (hkl) crystallites (see section 8.3). To reduce the deviation from the linear fit, it is necessary to include more reflections when averaging the lattice parameter.

The residual stress is calculated from the gradient or intercept of the $\langle a \rangle$ vs $\sin^2 \Psi$ plot by inserting the Young modulus and the Poisson ratio into Eq. 4.38.

The researchers at IAM-AWP have determined the reduced Young modulus $E/(1-\nu^2)$ of coatings on cemented carbide from the hardness measurement. The measured $E/(1-\nu^2)$ as a function of position is presented in Fig. 11.6 (a).

The typical range of the Poisson ratio for hard metallic coatings is $0.2 < \nu < 0.25$ [74]. Therefore the E was calculated from the reduced Young modulus for this ν range. The calculated residual stress of the coatings on cemented carbide is shown in Fig. 11.6 (b) as a function of X .

The calculated residual stress of the coatings on cemented carbide is in the range of 2-6 GPa. This value is within the typical range of the compressive residual stress for hard coatings [27].

The minimum residual stress of the coatings on cemented carbide is found for $0 \text{ mm} < X < 12 \text{ mm}$. Due to the large fitting error of the $\langle a \rangle$ vs. $\sin^2 \Psi$ plot as shown in Fig. 11.5 (a)

to (d)), the calculated residual stress might not represent the absolute value. However since all coatings have a similar fitting error, the tendency of the position-dependent $\sigma_{||}$ should be valid.

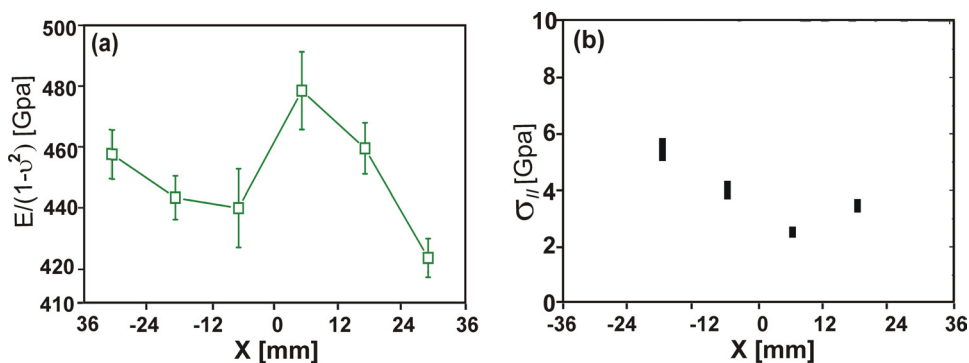


Figure 11.6: (a) Measured reduced Young modulus, and (b) calculated residual stress.

At the same X, the thickness of the coating on Si is roughly 0.3 times thickness of the coating on cemented carbide. Thus the elastic constant E and ν of coatings on Si might not be the same as the E and ν of coatings on cemented carbide. Therefore, the residual stress of coatings on Si will be calculated in future, when E and ν for this series of coatings will have been determined.

11.3 Main Results

The radial peak positions of all coatings can be fitted well by the distorted fcc unit cell model. In this model, the perfect cubic unit cell is deformed to a rhombohedral unit cell. The distortion is due to the lateral compressive stress as indicated from decreasing lattice spacings with increasing Ψ as shown in Fig. 8.16 and Fig. 9.15.

The residual stress of the coatings on cemented carbide was calculated. The calculated values is comparable to typical residual stress of the hard coatings, i.e. 2 - 6 GPa. The minimum stress is found for the coating at $X = 6$ mm. This position corresponds to the position close to the center of the target below the AlN part.

The interplay between residual stress, chemical composition, thickness and micro structure will be discussed in chapter 12.

12 Discussion

The desired properties of a new hard coating material should combine: (1) high hardness, (2) good toughness, (3) good adhesion and (4) low friction coefficient. The thermodynamic calculation shows that a promising candidate which fulfills all requirements is the material system V-Al-C-N (see section 2).

The V-Al-C-N coatings were deposited using rf magnetron sputtering from a segmented target. The chemical composition, the morphology and the microstructure of the coatings were determined. They are reported in chapter 7 until chapter 11.

In this chapter, we will discuss: the crystal phase of the V-Al-C-N coatings (section 12.1), the development of the texture of the V-Al-C-N coatings (section 12.2), the difference between coatings deposited on cemented carbide and on Si(001) (section 12.3), and the influence of the chemical composition and the microstructure on the hardness (section 12.4).

12.1 Crystalline Phase of V-Al-C-N Coating

One of the important factors which influence the mechanical properties of the coating is the crystalline phase. X-ray diffraction and x-ray absorption fine structure spectroscopy measurements were performed to determine the crystal phase of our coatings.

For all samples, all observed coating reflections in the radial geometry can be attributed to the fcc structure. However, this observation cannot exclude the existence of other phases e.g. an amorphous phase or very small crystallites of a hcp phase (hcp is one of the expected phases in the thermodynamic calculation described in section 2.3). If these other phases would exist, their scattering intensity might be integrated into the background. The background intensity contains e.g. the air scattering and the scattering from the domains of the samples which have short range ordering (e.g. amorphous phases). Due to this superposition, it is difficult to exclude the existence of amorphous or very small crystallites of a hcp phase from x-ray diffraction. Therefore, we performed XAFS measurements which have a better detection limit for an amorphous phases compared to the x-ray diffraction.

The XAFS was measured at the Vanadium K-edge for selected coatings covering the XANES and EXAFS regions. Their spectrum is influenced by the local environment of Vanadium, e.g. the type and number of the neighboring atoms.

The thermodynamically stable phases of the quasi binary system VC-AlN are fcc or hcp. The local environment of Vanadium in the fcc and in the hcp lattice is different: Vanadium in the fcc lattice has six nearest neighbor atoms while Vanadium in the mixed hcp V-Al-C-N phase has four nearest neighbor atoms (tetrahedral environment) [72, 73]. This leads to the XANES spectra differences for both phases, e.g. intensity of the expected pre-edge peak for fcc structure is weaker than for hcp structure.

The fcc structure of our coating is observed from both XRD and XANES spectra: (1) all coating reflections observed in the XRD profile of all coatings are attributed to the fcc structure and (2) the weak pre-edge peak observed in the XANES spectra of all coatings is a characteristic feature of fcc structure.

The chemical composition of the fcc phase cannot be determined from the relative intensity of the coating reflection in the radial geometry because of the texture. Thus XRD analysis cannot be used to conclude if the crystalline phase of the coating is fcc-VC or fcc-(V,Al)(C,N). The shifting of the minimum pre-edge peak to lower energy with increasing Nitrogen concentration might indicate the existence of direct bond of V-C and V-N (see detailed description in section 10.1).

Another XAFS region which we analyzed is the EXAFS region (see section 10.2). Two peaks related to the first and the second shell distances are observed in the Fourier transformation of the EXAFS spectra. These spectra were then fitted assuming two models, i.e. fcc and hcp. The positions and the relative intensity of the first and the second peaks fit best with the fcc model assuming some Al substitutes V atoms. Due to the similar absorption properties of C and N, the V-C and V-N cannot be distinguished well from EXAFS region. Thus fitting of the EXAFS spectra and the interpretation of the pre-edge shape in the XANES region confirm a mixed fcc-(V,Al)(C,N), which cannot be concluded from diffraction analysis.

The EXAFS spectra might be fitted with and without assuming existence of excess of Carbon within the fcc structure. However, the elemental analysis result (by EPMA) indicates that all coatings have excess of Carbon. The excess of Carbon in an amorphous phase is desired for the hard coating application in order to decrease the friction coefficient. If amorphous carbon exists, the scattering of this phase would be integrated in the background of the diffraction profile. High resolution transmission electron microscopy (HRTEM), x-ray photoelectron spectroscopy or raman spectroscopy might help to investigate the excess carbon [75].

12.1.1 Atomic Distance as a Function of Chemical Composition

The mixed fcc-(V,Al)(C,N) phase as indicated by the XAS spectra is presented in Fig. 12.1 (a). In this phase, some Aluminum replaces Vanadium, and some Nitrogen substitutes Carbon. The influence of the chemical composition on the atomic distance is discussed in the following.

The atomic distances of V-(C,N) and V-(Al,V) were determined using two methods: (1) by fitting the Fourier transformation of the EXAFS spectra and (2) from the distorted unit cell of the (111) texture. Figure 12.1 (a) shows a distorted (111) cubic unit cell. Due to the lateral compression of this unit cell, the angle α is smaller than 90° . As indicated in the figure, there are two values for the nearest distances of the V-(V,Al) which depend on the angle α . The atomic distances determined from the distorted unit cell are:

$$R_{V-(V,Al)} = \cos(0.5\alpha) \times a \quad (12.1)$$

$$R_{V-(V,Al)} = \cos(90 - 0.5\alpha) \times a \quad (12.2)$$

$$R_{V-(C,N)} = 0.5 \times a \quad (12.3)$$

where $R_{V-(V,Al)}$ is the average atomic distance of V-V and V-Al, and $R_{V-(C,N)}$ is the average atomic distance of V-C and V-N in the mixed fcc of V-Al-C-N phase.

Figure 12.1 (b) shows the atomic distance of V-(C,N) for coatings on cemented carbide as a function of X which were (1) calculated from the distorted unit cell of (111) texture (red spheres) and (2) determined from EXAFS (black spheres). The direction of increasing Aluminum and Nitrogen concentration is indicated on top of the figure.

We observe: (1) independent of how it is determined, the atomic distance decreases with increasing Al and N concentration and (2) for all coatings, the atomic distance determined from XAFS is smaller than the atomic distance determined from XRD. These observations are discussed as follows.

The relation between the lattice parameter and the chemical concentration is typically estimated by Vegard's law. This law predicts that the lattice parameter of an ideal solid solution varies linearly with the chemical composition. The assumptions for an ideal solid solution are: (1) the nature of bonding of the constituent phases is similar, (2) the substituting atoms are randomly distributed, (3) the lattice parameters of the constituents (in our case VC and AlN) differ by less than 5%. According to this law, the unit cell volume is a linear function of the concentration [76].

All of our coatings are laterally stressed. Therefore we could not compare directly the measured atomic distance to the relaxed atomic distance expected from the Vegard's law. Assuming that the unit cell volume does not change with compression, we should compare the measured unit cell volume to the expected relaxed unit cell volume as a function of concentration.

Figure 12.1 (c) shows the unit cell volume of the (111) texture crystallites as a function of the Al to (Al+V) ratio (black squares). In our case it is difficult to compare the measured and the expected values from Vegard's law because the relaxed unit cell parameter of stoichiometric VC is not available (this phase is not stable). The reported unit cell parameters (measured and calculated) of VC_y are in the range of $4.1 < a < 4.22$ Å [77, 78, 79]. Therefore depending on the unit cell parameter which we consider, the expected unit cell volume as a function of Al concentration might be different.

The red line in Fig. 12.1 (c) is the expected unit cell volume as a function Al/(Al+V) ratio assuming $a_{VC} = 4.165$ Å and $a_{AlN} = 4.12$ Å [80] (in other references, the reported $a_{AlN} < 4.12$ Å [81, 82]). The offset between the measured values and the red line is observed.

The value $a_{VC} = 4.165$ Angström is related to the relaxed unit cell of non-stoichiometric V_8C_7 [83]. Assuming the linear increase of the lattice constant with the Carbon concentration, the expected stoichiometric VC is larger than 4.165 Å and hence the red line in Fig. 12.1 (c) is expected to shift in the direction of the measured data.

The red line is calculated assuming the same Al and N concentration in the fcc-VC structure. However, the elemental analysis of the coatings shows that the concentration of Nitrogen is smaller than the concentration of Aluminum. This might be another reason why the measured unit cell volume deviates from the expected unit cell volume assuming the validity of Vegard's law (red line in Fig. 12.1 (c)).

Furthermore, even in case the relaxed unit cell data would be available, in some cases a deviation from Vegard's law is theoretically expected and experimentally observed. The deviation is more pronounced if the atomic constituents have a large atomic size difference. Thermodynamically the difference is related to the excess Gibbs energy of the solid solution relative to the Gibbs energy of the pure components of the solid solution [76, 84, 85].

Despite the offset between the Vegard's law and the measured values, the decreasing of the unit cell volume with increasing Al concentration is expected for a VC-AlN mixture.

Another interesting point to discuss is the offset which is observed between the atomic

distance determined from the EXAFS and from the XRD as shown in Fig. 12.1 (b). A similar offset of atomic distance determined by XRD and XAS is also reported in reference [72] for a TiN coating (in this case, the offset is $\sim 0.025 \text{ \AA}$).

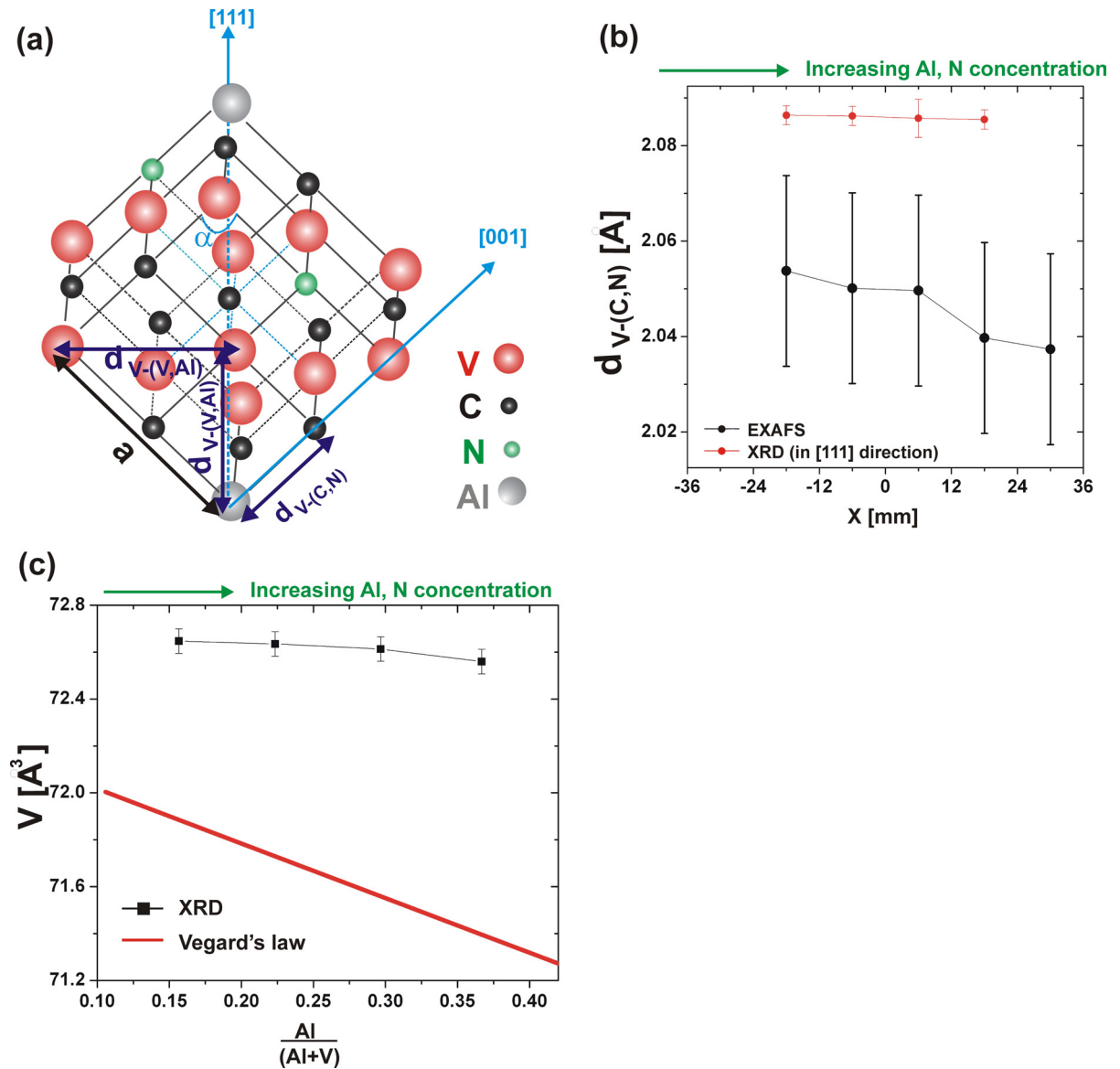


Figure 12.1: (a) A (111) oriented cubic unit cell of a mixed fcc-(V,Al)(C,N), (b) atomic distance of V-(C,N) as a function of position and (c) the unit cell volume of the (111) texture as a function of the Al/(Al+V) ratio.

EXAFS measures the average interatomic distance of all types of textures or powder

present in the coating while $R_{V-(V,C)}$ determined from XRD is calculated from the distorted unit cell of the isotropic (111) texture only. This might be one explanation for the offset of the atomic distance determined by XRD and EXAFS.

The offset of the interatomic distance determined from the XRD and XAFS is not fully understood so that the fitted values cannot be taken as absolute values. However, the tendency of decreasing interatomic distance with increasing Al content is valid and this is as expected for a mixed fcc-(V,Al)(C,N).

12.1.2 Solubility Limit of AlN in fcc-VC Structure

The hardness of the coating is expected to increase with increasing the covalent hard material concentration, i.e. AlN in our case. The results of the thermodynamic calculation predicts that the solubility limit of AlN in the fcc structure of VC is higher compared to many other material systems e.g. commercially available TiAlN coating. The high solubility limit means that we might obtain a higher hardness without decreasing the toughness (toughness is related to the fcc structure). In this section, the Al concentration of our coatings and the solubility limit of AlN in fcc-VC are discussed.

Figure 12.2 shows schematically the expected metastable phase as a function the Al to (Al+V) ratio. At low Al concentration, the mixed fcc-(V,Al)(C,N) phase is expected while the mixed hcp-(V,Al)(C,N) phase is expected for higher Al concentration (i.e. above critical concentration $c_{tr,ms}$).

The Al concentration of our coatings as determined from EPMA measurement is in the range of $0.1 < \text{Al}/(\text{Al}+\text{V}) < 0.4$ (indicated by grey area). The critical concentration $c_{tr,ms}$ (see section 2.2) for VC-AlN is not known. However, since all coatings have a mixed fcc (V,Al)(C,N) phase, the $c_{tr,ms}$ of VC-AlN must be larger than 0.4.

Figure 12.2 also indicates $c_{tr,ms} = 0.65$ for TiN-AlN [9]. The interaction energy ϵ of TiN-AlN is larger than the interaction energy of VC-AlN, therefore we expect $c_{tr,ms}$ of VC-AlN > 0.65 (the relation between ϵ and $c_{tr,ms}$ is described in section 2.3).

The Al concentration in our coatings is still smaller than the critical concentration. This means that the properties of the hard coating might still be optimized by increasing the chemical composition of the coating up to $\text{Al}/(\text{Al}+\text{V}) \approx c_{tr,ms}$. Above this critical concentration, the crystalline phase is transformed to hexagonal close packed (hcp).

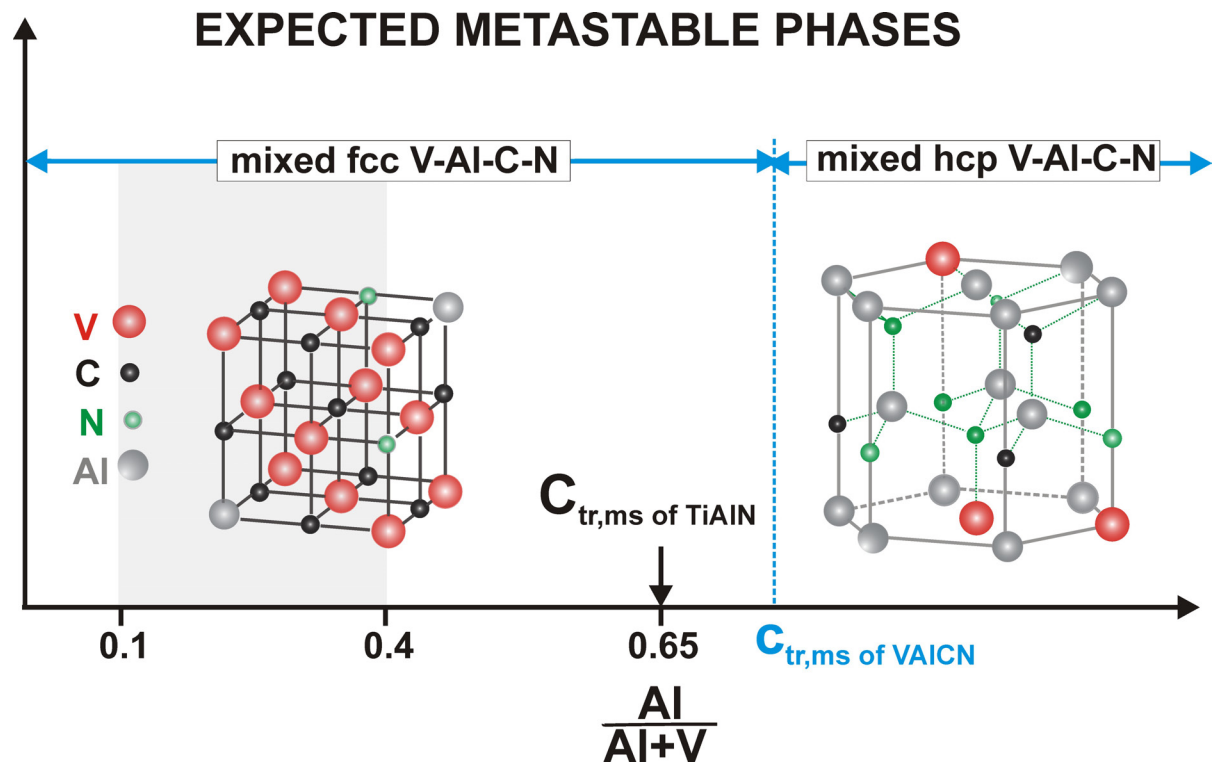


Figure 12.2: The schematic of expected crystalline phases as a function of Al/(Al+V) ratio.

12.2 The Development of the Texture of the V-Al-C-N Coating

The texture analysis is one of the important aspects for the coating application. The result of the texture analysis can also be used for better understanding of the growth mechanism. For hard coating applications, the texture might influence the mechanical properties e.g. hardness and wear resistance. The influences of the texture of V-Al-C-N coatings on the mechanical properties was not yet systematically studied (the V-Al-C-N is new material system). However, the wear resistance of a similar system, TiN, is higher for the (111) texture [15].

There are several x-ray diffraction measurement types to study the texture, e.g. pole figure, strain map and rocking curve. In our case, we measured the (111) and the (200) pole figures as well as the strain map which covers the (111), the (200), and the (220) coating reflections.

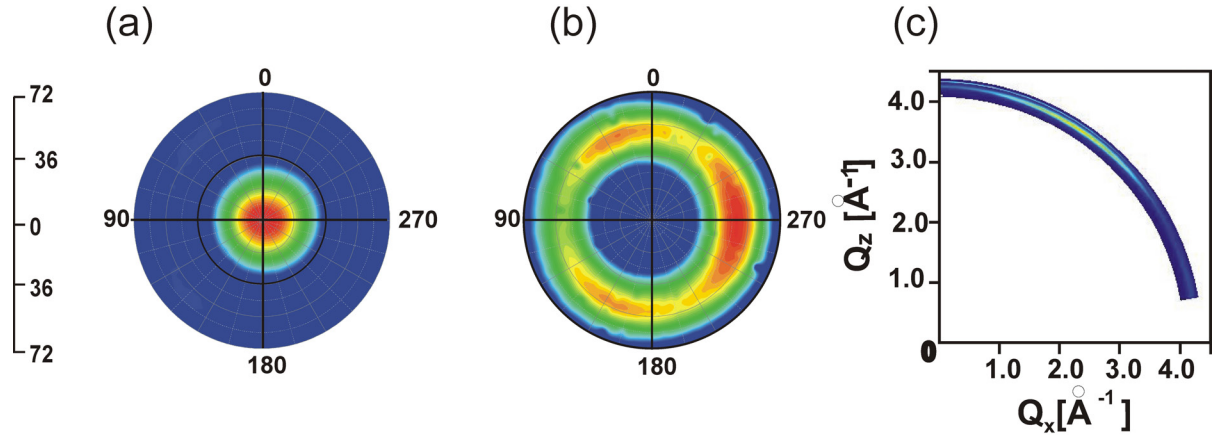


Figure 12.3: The detailed texture analysis requires (a) the (111) pole figure, (b) the enhanced (200) pole figure and (c) the strain map.

For a detailed texture analysis, measuring only one (hkl) pole figure might not be enough to describe comprehensively the crystal orientation of the coating. As an example, (a) the (111) pole figure, (b) the enhanced (200) pole figure as well as (c) the enhanced (220) strain map for coating on cemented carbide at $X = -6$ mm are presented in Fig. 12.3. The (111) texture with in-plane orientation could not be verified by measuring the (111) pole figure only. The anisotropic (111) texture is weak and is strongly superimposed with the isotropic (111) texture. Therefore it is not visible by eye in the (111) pole figure. The (111) texture with in-plane orientation is indicated by the three-fold intensity distribution in the enhanced intensity scale of the (200) pole figure. Additionally for this sample, the weak (220) texture is indicated by the line scan of the (220) strain map.

The line scans of the pole figures and the strain map at the given cut direction were fitted and the average orientation Ψ_{hkl} and the orientation distribution σ_{hkl} of different textures were determined.

The main results of the texture analysis are: (1) the texture superposition is observed for all coatings, (2) the dominant texture is the (111) texture without in-plane orientation, (3) the in-plane orientation is only observed for coatings on cemented carbide, and (4) the intensity attributed to the powder is stronger for coatings on Si than for coatings on cemented carbide.

In this section, we would like to discuss: (1) the growth mechanism for the texture superposition and (2) the development of the monoaxially and biaxially aligned texture.

12.2.1 Development of the Texture Superposition

The crystal growth is influenced by a combination of many factors, e.g. the flux distribution, the energy of the incident flux, the diffusion, the deposition rate and the substrate type. As the growth process is complex and involves many parameters, the detailed mechanism for the preferential growth direction is still not well understood [15, 86].

However, the preferential growth orientation is often attributed to the surface free energy minimization, strain energy minimization or anisotropic growth rate of differently oriented crystals [15, 86]. These fundamental parameters might not be constant as a function of thickness. This means that the parameter which controls the preferential growth might change as a function of thickness.

The reference values (i.e. the surface free energy, the strain energy and the growth rate of differently oriented crystals) are not available for our system. Therefore, in the discussion we compare our observation to a similar material system (i.e. TiN).

For TiN, the (001) texture has a lower surface energy than the (111) texture so that the (001) texture is expected at early growth stage. Depending on the deposition parameters, both (111) and (001) texture might growth at higher thickness. At sufficiently high adatom mobility (related to the ion to atom ratio during deposition), the growth might be controlled by the surface energy minimization so that the (001) texture is developed. At lower adatom mobility, the texture development at higher thickness is controlled by the competitive growth rate, i.e. the crystallite with higher growth rate will overgrow other (hkl) crystallites. In the case of TiN, the (111) crystallites have a higher growth rate than other (hkl) crystallites [15, 35, 88].

Independent of the positions and the substrates, all of our coatings have a dominant (111) texture. For most of the coatings, the (111) texture, the (200) texture, (220) texture as well as powder are superimposed. A deviation from this observation is found for the coating on cemented carbide at $X = 6$ mm where the (111) texture without in-plane orientation and the anisotropic (111) texture are superimposed. In this case, other types of texture might be too weak to be observed.

The superposition of different types of texture might be explained as follows. In the beginning of the growth, the crystals grow randomly. However, due to the anisotropic growth rate of differently oriented crystals, the (hkl) crystal having the fastest growth rate might overgrowth other crystals. From the experimental observation, we assume that in our case, the (111) crystals have the fastest growth rate.

The texture analysis of our coatings indicates that the development of the texture super-

position for V-Al-C-N coating is similar to the growth model for TiN material proposed by other groups [15].

12.2.2 Development of Monoaxially and Biaxially Aligned Texture

For all coatings, we observed the (111) texture without in-plane orientation (monoaxial (111) texture). Depending on the position below the segmented target and the substrate, this texture is superimposed with other textures, e.g. the (200) texture, the (220) texture and randomly oriented crystallites. For coatings on cemented carbide, in-plane oriented (111) textures (biaxially aligned (111) textures) were also observed. This biaxially aligned texture is not found for coatings on Si (see chapter 8 and chapter 9). In the following, the development of the monoaxially and biaxially aligned texture is discussed.

The calculated average flux direction during the deposition of our V-Al-C-N coating is given in section 3.3.1. The calculation was performed assuming the ballistic regime. It is found that the direction and the magnitude of the average flux distribution varies as a function of the sample position below the segmented target. The calculated results also show that the local flux distribution has a two-fold symmetry with mirror axis parallel to the X axis (see Fig. 3.5).

The texture analysis of the coatings shows that the average orientation of the dominant (111) texture is coincident with the calculated average flux direction, except for the coatings placed below the edge of the target. For these positions, the collisions between the sputtered atoms and the plasma species cannot be neglected. The angular distribution is not only influenced by the deposition geometry but also the collisions.

The growth direction of the crystallites can be influenced by several parameters, e.g. the angular distribution of the incident flux, the deposition rate and the diffusion of the atoms on the substrate surface. Because we observe that the average direction of the dominant (111) texture is coincident with the calculated average flux direction, we conclude that in our case: (1) the deposition geometry influences the texture direction, (2) the ballistic regime is a good approximation (except for position below the edge of the target), and (3) the atomic diffusion on the surface is low.

The biaxially aligned texture which we observed for coatings on cemented target might be related to the anisotropy in the flux distribution from both the VC and the AlN target. Other researcher has reported in-plane orientation due to the substrate tilting [88]. They related in-plane orientation to the anisotropic capture length of a crystallite: the crystallites oriented in the 'correct' orientation relative to the incident flux might overgrowth crystallites with less preferable orientation.

If the overgrowth model is valid, then the development of the in-plane texture is related to the thickness. This might explain why in our case the in-plane oriented texture is not observed for thinner samples, i.e. for coatings on Si.

12.3 The Differences between Coatings on Cemented Carbide and Coatings on Si

Two series of coatings were deposited on cemented carbide and on Si(001) substrates with similar deposition condition. At the same X position, the differences between the two series of coatings might be influenced by the thickness and the substrate types. The XRD results show that those factors do not influence the crystalline phase and the main (111) texture of the studied coatings. However, some differences between coatings deposited on cemented carbide and on Si(001) are observed. They are discussed in this section.

In order to exclude the geometry effect, the microstructure differences at the same position are compared. As an example, Figure 12.4 shows the main differences for coatings at X = -6 mm.

One of the differences is the in-plane orientation. The in-plane orientation is only observed for coatings deposited on cemented carbide. This is visible for e.g. from the (200) pole figures presented in Fig. 12.4 (a). The (200) ring of coating on cemented carbide has a three-fold symmetry (indicating the anisotropic (111) texture), while the (200) ring of coatings on Si has a homogeneous intensity distribution (indicating the isotropic (111) texture).

Another difference is the relative fraction of the coexisting textures. This is shown by line scan fitting of both series of coatings as presented in Fig. 12.4 (b). Each color represents a different type of texture as indicated in the figure. For X = -6 mm as an example, the fraction of the (200) texture and the powder-like crystallites are larger for coating deposited on Si than on cemented carbide. As discussed earlier, the in-plane texture as well as the fraction of the texture (and powder-like crystallites) are most likely related to the coating thickness.

The substrate type might influence the coating growth in several ways including epitaxial growth. Depending on the deposition parameter, an epitaxial thin film might be grown on a single crystal substrate. In our case, this is not expected for the coatings deposited

on the Si(001) substrate because the amorphous SiO₂ layer on the Si(001) substrate was not removed prior to deposition so that the crystals did not grow directly on the single crystal substrate. This is consistent with the XRD results which show that all coatings are polycrystalline with texture superposition.

The substrate type might also affect the development of the residual stress of the coating. Figure 12.4 (c) presents d_{hkl} vs. $\sin^2\Psi$ plot, from which the residual stress can be determined. For both series of coatings, d_{hkl} decrease with increasing Ψ , indicating compressive strain. However, the monotonous decrease is only observed for coating deposited on Si.

The residual stress depends on how the crystal grows and on the thermal stress, i.e. $\sigma_{||} = \sigma_{growth} + \sigma_T$. The thermal stresses σ_T is proportional to the deposition temperature and to the difference of the thermal expansion coefficient of the substrate α_s and the coating α_f [55, 56, 91]. Thermal stress is more dominant if the coating is deposited at high temperature. Because all coatings were deposited at low temperature, i.e. $T_s/T_m \leq 0.3$, the α_s difference of cemented carbide and Si substrates most likely does not influence the residual stress (and hence the d_{hkl} vs. $\sin^2\Psi$ plot) of the studied coatings (T_m is the melting temperature. For hard materials, T_m is typically in the range of 2500 to 3000° C [92]). This is consistent with our further texture analysis that the d_{hkl} vs. $\sin^2\Psi$ behavior is related to the texture of the coating (see section 8.3 and 9.4).

As a conclusion for this section, the differences between both series of coatings are most likely due to the coating thickness rather than the different substrate types.

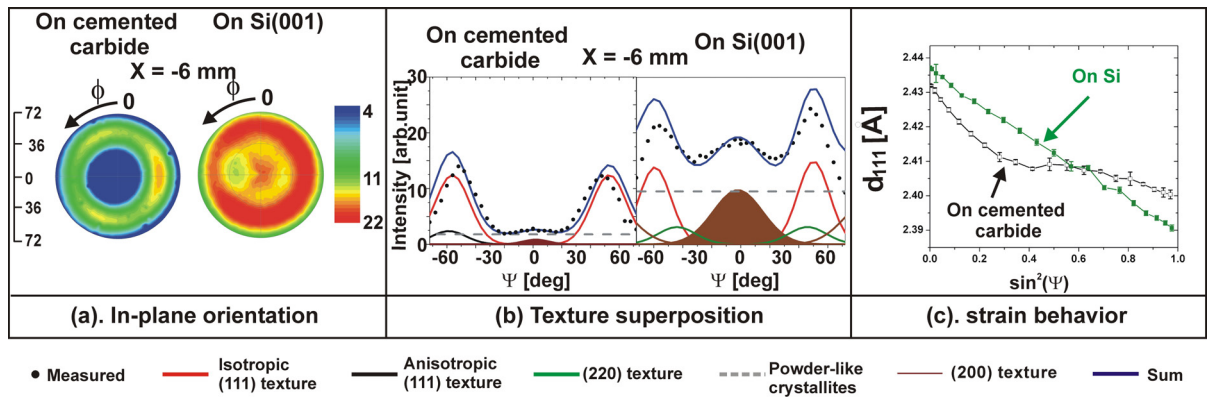


Figure 12.4: The microstructure of the coatings on cemented carbide and on Si is different in the following aspects: (a) in-plane orientation; (b) texture superposition and (c) strain behavior.

12.4 Interplay between Chemical Composition, Microstructure and Hardness

A new material system for hard coating application, i.e. V-Al-C-N, was deposited using sputter deposition from a segmented target. We found from XRD and XAFS analysis that all coatings have the crystal structure which is desired for high hardness and good toughness, i.e. a mixed fcc-(V,Al)(C,N) phase where the covalent hard material (AlN) is dissolved in the fcc lattice of the metallic hard material (VC).

The hardness is influenced by a combination of many factors (see section 2.4): (1) it is expected to increase with increasing concentration of the covalent hard material, i.e. AlN, (2) it is expected to increase with decreasing grain size, (3) it is proportional to the residual stress, (4) it is influenced by the texture superposition and (5) it depends on the crystal orientation. In order to be able to optimize the mechanical properties of V-Al-C-N, first, it is important to understand the influence of the chemical composition and the microstructure on the hardness of our coatings.

The chemical composition, the main features of the microstructure and the measured hardness as a function of X are summarized in Fig. 12.5. The gray background corresponds to the position of maximum hardness.

One of the important factors which influence the hardness is the grain size. The influence of the grain size on the hardness is known as a Hall-Petch relation. Above a critical size (typically considered as 10 nm), the hardness is expected to increase with decreasing grain size.

The grain size is often determined from the FWHM of the coating reflections in the radial direction. Prior to estimating the grain size from the FWHM, a critical peak broadening analysis should be performed e.g. by measuring higher order reflections (see section 4.4.2). If the strain broadening is dominant then the grain size cannot be determined from the FWHM. If the strain broadening is negligible, then the grain size can be estimated from the FWHM using e.g. the Debye Scherrer formula. For powder like crystallites, the strain distribution and the size might be separated by using the Williamson-Hall plot.

In our case only the higher order of the (111) reflections was measured. For all coatings, the $\text{FWHM}_{222}/\text{FWHM}_{111} \sim 2$, except for coatings on cemented carbide in the range of $0 \text{ mm} < X < 24 \text{ mm}$. This indicates that the FWHM is dominated by the strain broadening (see Fig. 12.5 (d)). Therefore, the grain size of our coatings cannot be determined accurately from the peak broadening. However, the minimum grain size can be calculated using Eq. 4.21 assuming: (1) no strain broadening and (2) the (111) crystallites

have a cylindrical shape. For coatings on cemented carbide, the calculated minimum height is in the range of 15 to 30 nm while the calculated minimum diameter is in the range of 6 - 8 nm. Thus even though the actual size cannot be determined, we are able to identify that the height of the (111) crystallites is larger than the critical size ($d \approx 10$ nm) where the size is expected to influence the hardness.

The highest hardness is found for the coating at $X = 6$ mm. If the hardness would only be influenced by the chemical composition, then the coating with highest Al/(Al+V) percentage is expected to exhibit maximum hardness (see $X = 30$ mm in Fig. 12.5 (b)).

The hardness is expected to be proportional to the residual stress. In our case, the maximum hardness is observed for the coating with the minimum residual stress (see Fig. 12.5 (c)). This means that other factors might influence the hardness. However this is an interesting result for the following reason. In industrial application, the machining tool (which is protected by the thin layer of hard coating) is typically operated at elevated temperature (ranging from hundreds to thousands degree Celsius). At this operating temperature, the decreasing hardness is commonly observed. This phenomenon seems to be related to the residual stress relaxation. If the residual stress at room temperature is low, the decrease of the hardness at elevated temperature might be minimized.

Figure 12.5 (e) and (f) show that the highest hardness is found for the coating which has a tilted (111) texture and the smallest distribution σ_{111} of the (111) texture. The crystal orientation and its distribution affect the macroscopic elastic constant which at the end influence the hardness.

In our case, it is difficult to study the influence of individual hardening mechanism on the hardness because as presented in Fig. 12.5, the coating has not only chemical composition and thickness variation as a function of X but also microstructure variations, e.g. the texture superposition, the average orientation of the dominant texture, and the grain size. However, we found that the highest hardness is observed for the coating which: (1) has the lowest residual stress, (2) does not have the highest Al concentration, (3) is at a position where the size broadening cannot be neglected, (4) has a tilted average direction Ψ_{111} of the (111) texture, and (5) has the narrowest orientation distribution of the (111) texture σ_{111} .

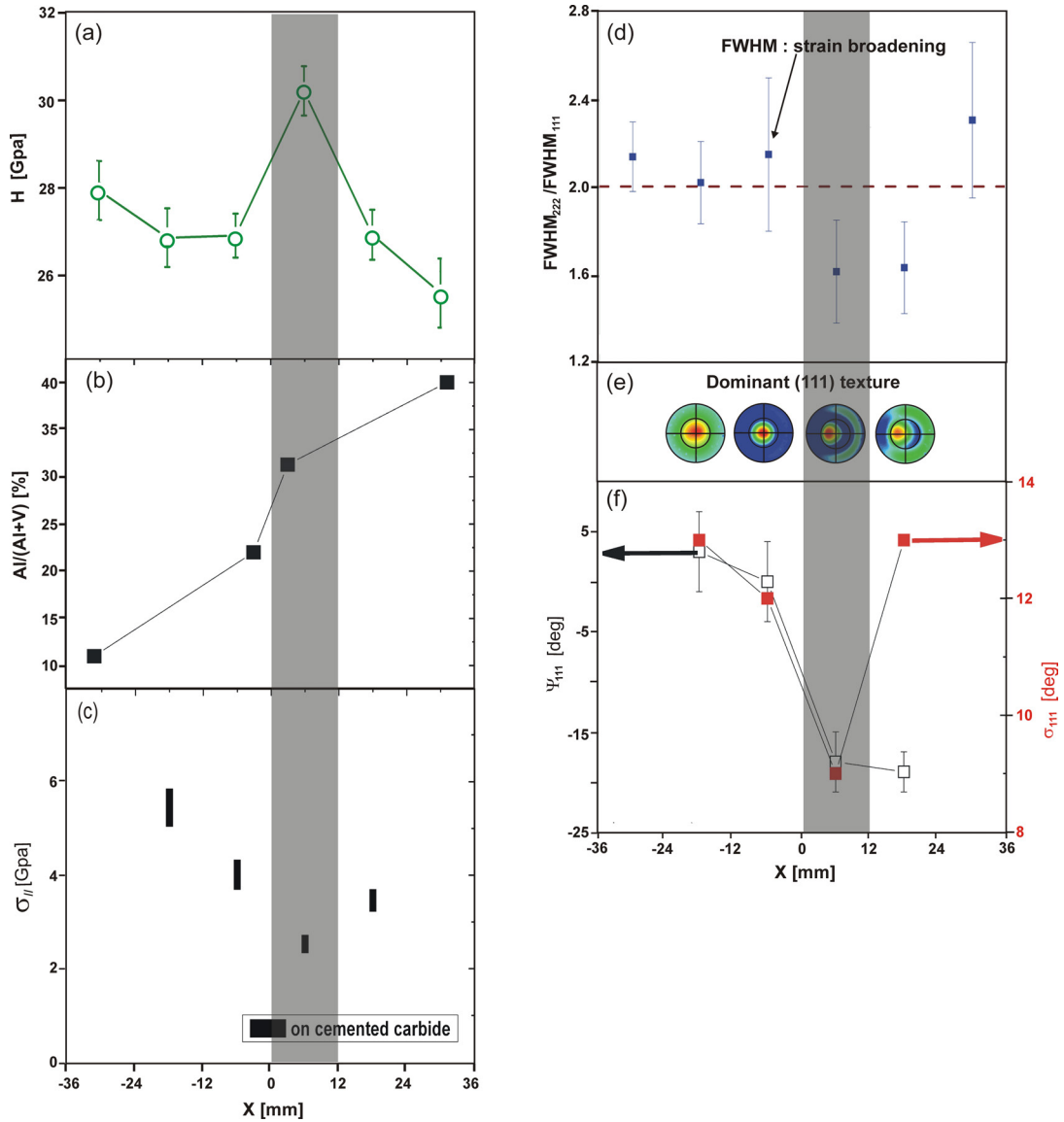


Figure 12.5: (a) Hardness, (b) Al/(Al+V) percentage, (c) residual stress (d) $FWHM_{222}/FWHM_{111}$ ratio, (e) the (111) pole figure and (f) orientation and distribution of (111) texture as a function of position.

It is interesting to compare the hardness of our coating and the hardness of other hard materials, to find out experimentally if the V-Al-C-N has a high hardness as expected from the thermodynamic calculation. Figure 12.6 shows the maximum hardness of V-Al-C-N in comparison to other materials [11, 12, 32, 87, 93, 94, 95]. The number given there should not be taken as an absolute value because the hardness of those material might not be measured under the same conditions. It is known that the measured hardness

is sensitive to how the measurement is performed, i.e. the given load, the indentation depth, the indentation rate, etc. However it is still valid, e.g. that the diamond and c-BN have larger hardness than other materials.

The maximum hardness of our coating is ~ 30 GPa. The value is within the typical range of hard coating material. It is shown in this figure that the hardness of $\text{Ti}_{0.45}\text{Al}_{0.55}\text{N}$ is higher than the hardness of the V-Al-C-N coatings. This might be related to (1) the higher concentration AlN in the TiAlN than in the VAICN or (2) the fact that the microstructure of the VAICN coating is not yet optimized.

One possible way to optimize the hardness of the VAICN coating is by increasing the AlN content of the coating.

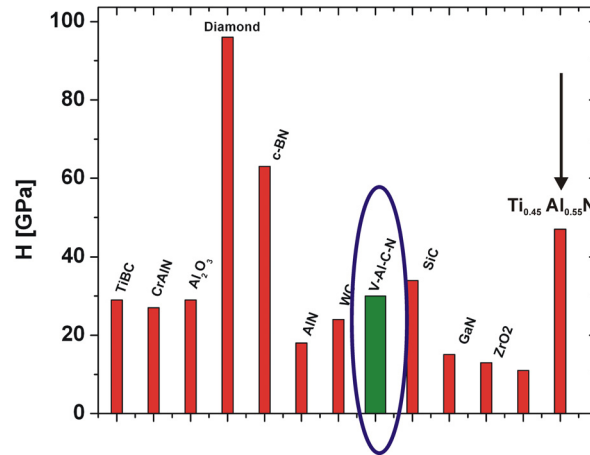


Figure 12.6: Green: hardness of our coatings, in red: hardness of other hard materials [11, 12, 32, 87, 93, 94, 95].

13 Summary, Conclusions and Outlook

The aim of this study is to optimize the mechanical properties of the new V-Al-C-N hard coatings. Thermodynamic calculations show that V-Al-C-N is a promising candidate as a new hard coating material compared to e.g. Ti-Al-C-N because the solubility limit of AlN is expected to be larger in the VC structure than in TiC structure. The hardness is expected to increase with increasing AlN concentration.

Two series of the V-Al-C-N hard coatings on cemented carbide and on Si were deposited by rf magnetron sputter deposition. A segmented target consisting of half a VC target and half an AlN target was used. It was found that the chemical composition and the thickness vary as a function of position below the target. The microstructure of the coatings was analyzed by X-Ray Diffraction and X-Ray Absorption Fine Structure Spectroscopy.

In this chapter, the microstructure of the coatings on both substrates is summarized in section 13.1. The conclusions of the study are given in section 13.2. The propositions for further studies are presented in section 13.3.

13.1 Summary

Figure 13.1 presents the schematic of the substrate-target arrangement, the chemical composition, the thickness variation and the microstructure of the V-Al-C-N coatings as a function of position. Figure 13.1 (a) shows a schematic cross section of the substrate-target arrangement during deposition. The microstructure of the coatings was investigated for samples in the range of $-36 \text{ mm} < X < 36 \text{ mm}$. X is position below the target.

Figure 13.1 (b) shows the chemical composition and thickness variation of the coatings on cemented carbide. The chemical composition and thickness of the coatings on Si were not measured. However, the chemical composition of both series of coating is expected to be similar because the deposition parameters are similar, except for the deposition time. Assuming that the deposition rate is constant with time, the thickness of the coatings on Si is approximately 0.31 times the thickness of the coatings on cemented carbide (deposition time of coatings on Si \approx 0.31 deposition time of coatings on cemented carbide). The chemical composition and the thickness variations as a function of position are ex-

pected because: (1) the sputtering yield of VC and AlN is different and (2) because of the anisotropy of the angular flux distribution. For all positions, the VC concentration is higher than the AlN concentration. This indicates that the sputtering yield Y_{VC} of VC is higher than the sputtering yield Y_{AlN} of AlN. The relative sputtering yield of VC and AlN is determined from the chemical composition at $X = 0$ where the concentration is not influenced by the geometry, i.e. $Y_{VC} \approx 3 Y_{AlN}$.

As presented in Fig. 13.1 (c), independent of the position and substrate type, all coatings have a mixed phase (V,Al)(C,N) in rock salt structure. The hexagonal phase was not observed. This fcc structure is most likely related to the low Al concentration of our coatings, i.e. $0.1 < \text{Al}/(\text{Al}+\text{V}) < 0.4$. The solubility limit of AlN in the fcc-VC is expected to be higher than AlN in TiN [9]. It is reported that for Ti-Al-N coatings, the solubility limit is larger than 0.6 [72, 73].

The texture of the coatings was investigated using pole figures and strain maps. Figure 13.1 (d) shows the (111) pole figures of the coatings which indicate that all coatings have a dominant (111) texture without in-plane orientation. The corresponding (200) pole figures are presented in Fig. 13.1 (f). The (200) rings of coatings on cemented carbide show inhomogeneous intensity distribution which indicates coexisting textures having in-plane orientation. The in-plane orientation was not observed for coatings on Si. This difference might be related to the overgrowth mechanism. Some critical thickness is needed for the preferential orientation to develop. Therefore, the in-plane orientation is not observed for thinner coatings (in our case coatings on Si).

For further identification of the texture superposition, the line scans of the pole figures and strain maps were fitted by calculated peak positions. The average direction Ψ_{hkl} and the distribution σ_{hkl} of all textures are determined from this fitting.

Figure 13.1 (e) shows variation of the average direction Ψ_{111} of the dominant (111) texture without in-plane orientation as a function of X. The negative Ψ indicates the direction towards the VC target. The blue dashed line is the calculated average flux direction as a function of position. For both series of samples: (1) the narrowest distribution of the (111) texture σ_{111} is found for sample in the range of $-12 \text{ mm} < X < 12 \text{ mm}$, (2) in the range of $-24 \text{ mm} < X < 24 \text{ mm}$, the Ψ_{111} of the dominant (111) texture without in-plane orientation follows the calculated average flux distribution (see Fig. 13.1 (e)), and (3) the most tilted (111) texture is observed at $0 \text{ mm} < X < 24 \text{ mm}$. At each position, Ψ_{111} of the anisotrop (111) texture (i.e. exhibit in-plane orientation) is more tilted than Ψ_{111} of (111) texture without in-plane orientation (see Fig. 13.1 (e) and (g)). The variation of Ψ_{111} of both isotropic and anisotropic (111) texture with the position indicates the influence of the deposition geometry on the development of this texture.

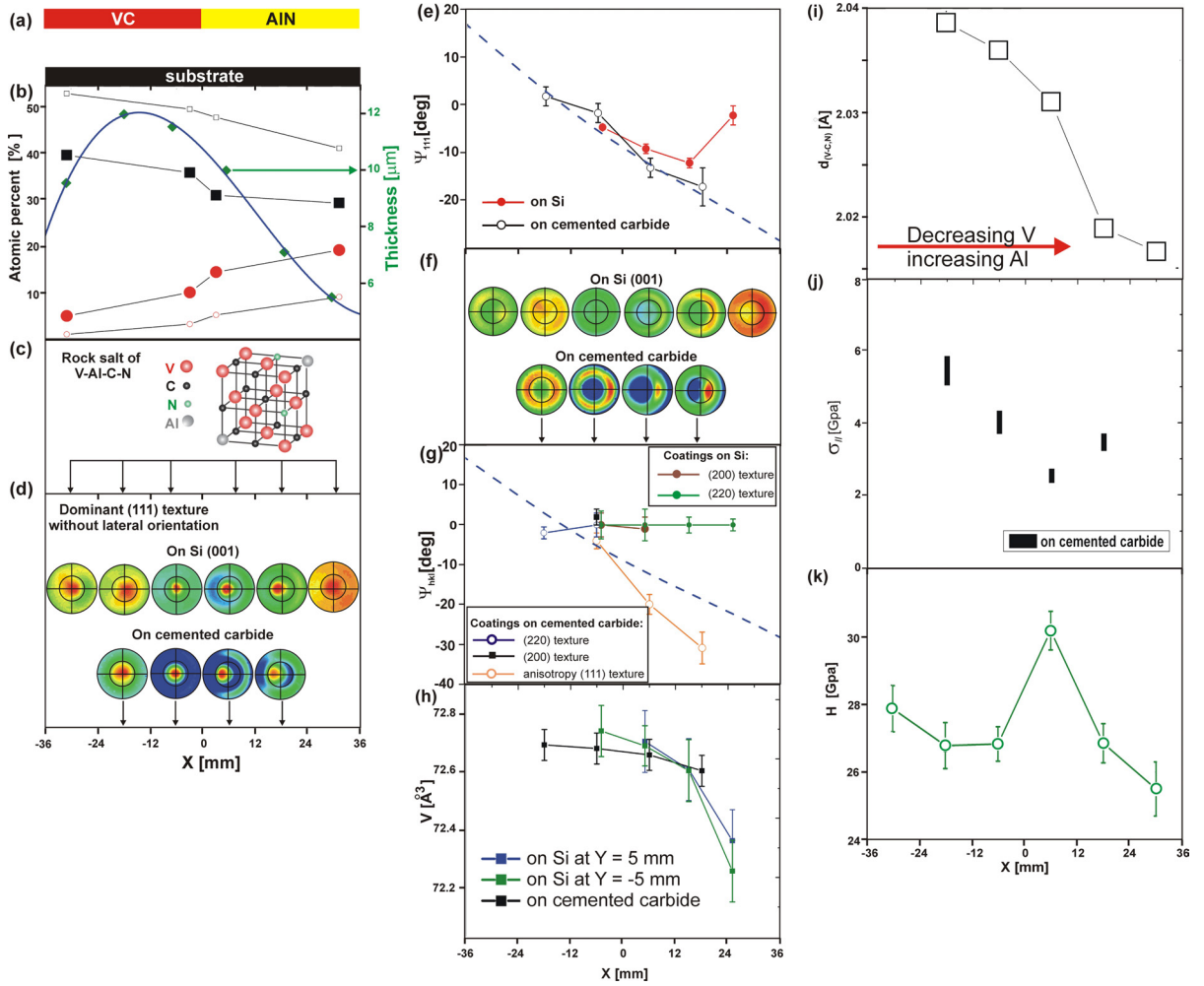


Figure 13.1: (a) Target-substrate geometry, (b) chemical composition and thickness as a function of position. All coatings have (c) a mixed phase rock salt structure and (d) the dominant (111) texture. However, (e) the Ψ_{111} , (f) the (200) pole figures, (g) the Ψ_{hkl} of the coexisting textures, (h) the volume unit cell, (i) the atomic distance, (j) the residual stress and (k) the hardness vary as a function of position.

For all other coexisting textures, Ψ_{hkl} does not vary significantly as a function of position (see Fig. 13.1 (g)). This indicates that the development of these textures is not influenced by the deposition geometry.

The unit cell parameters of the (111) texture crystallites have been calculated from the (111), the (200) and the (220) reflections of the strain map (see section 11). Those reflections were fitted with two models, which are the cubic unit cell and the distorted cubic

unit cell. It is found that the distorted cubic unit cell (i.e. a slightly rhombohedral unit cell) fits better than the cubic unit cell model. Their volume unit cell V as a function of X is presented in Fig. 13.1 (h). For the same X , the V of the coatings on cemented carbide and on Si is the same within the error bar.

The atomic distance of the coatings was determined from the EXAFS spectra and the results are shown in Fig. 13.1 (i). The atomic distance decreases with decreasing V concentration (or increasing Al concentration). The tendency is consistent with the unit cell parameter variation. This is expected because the substituting atom Aluminum is smaller than the Vanadium atom.

The residual stress of the coatings was calculated by inserting the measured reduced Young modulus into Eq. 4.37. The results are presented in Fig. 13.1 (j). The minimum stress is found for the coating at $X = 6$ mm.

The hardness of the coatings on cemented carbide is determined from the nano indentation measurement. The results is presented in Fig. 13.1 (k). The maximum hardness is found for coating at $X = 6$ mm. This position corresponds to the coating which exhibit a tilted (111) texture, has the narrowest distribution of the (111) texture, and has the lowest residual stress. The maximum hardness is not observed at the coating with the highest AlN concentration which was expected. This indicates that for our coating, the microstructure plays an important role for the hardness evolution.

13.2 Conclusions

We found that the deposition geometry does not only influence the chemical composition and the thickness variation, but also the microstructure of the coatings, i.e. texture, lattice parameter, residual stress, and atomic distance.

By combining XRD and XAFS methods, the crystal phase of the coatings can be determined: all coatings have a mixed fcc of (V,Al)(C,N) phase. The Al/(Al+V) ratio in our coatings is in the range of $0.1 < \text{Al}/(\text{Al}+\text{V}) < 0.4$. This range is smaller than the expected solubility limit of AlN in VC (from thermodynamic calculation). Therefore, the intrinsic hardness might still be optimized by increasing the AlN concentration.

Because both the chemical composition and the microstructure vary as a function of position, it is difficult to separate the individual contribution of the chemical composition and the microstructure on the mechanical properties.

13.3 Outlook

The aim of the studies was to optimize the mechanical properties, e.g. the hardness, the toughness and the friction coefficient of the new V-Al-C-N hard coatings. Within this objective, we would like to continue the research project as follows.

In order to optimize the intrinsic hardness, we propose to increase the concentration of the covalent hard material (AlN) by e.g. using a segmented target with a larger fraction of the AlN part. This experiment is important: (1) to determine experimentally the solubility limit of AlN in the VC structure and (2) to have a higher intrinsic hardness.

The elemental composition shows that all coatings have an excess of Carbon. In a similar material system as ours, the excess of Carbon is found as an amorphous phase at the grain boundaries. High Resolution Transmission Electron Microscopy (HRTEM), X-Ray Photoelectron Spectroscopy or Raman Spectroscopy might help to investigate the existence of an amorphous carbon phase in our coating. This investigation is important because the amorphous carbon is expected to decrease the friction coefficient.

An in-situ characterization during coating growth is also proposed in order to verify the mechanism of texture development, e.g. whether the overgrowth mechanism can explain the development of the in-plane orientation or not.

14 APPENDIX A

Unit Cell Scattering Factor of (VC)

For any crystal structure, the unit cell scattering factor depends on the atomic scattering factor f_j and the atomic position \mathbf{r}_j in a unit cell, i.e. $F_{u.c} = \sum_{r_j} f_j(Q) e^{i\vec{Q} \cdot \vec{r}_j}$. The Laue condition for constructive interference occurs if $\mathbf{Q} = \mathbf{G}$ where $\mathbf{G} = 2\pi(h\mathbf{a}_1^* + k\mathbf{a}_2^* + l\mathbf{a}_3^*)$. Inserting \mathbf{G} and the atomic position $\mathbf{r}_j = n_1\mathbf{a}_1 + n_2\mathbf{a}_2 + n_3\mathbf{a}_3$ into $F_{u.c}$ results in:

$$F_{u.c}(Q) = \sum_{r_j} f_j(Q) e^{i2\pi(ha_1^* + ka_2^* + la_3^*)(n_1a_1 + n_2a_2 + n_3a_3)} \quad (14.1)$$

where \mathbf{a}_1^* , \mathbf{a}_2^* and \mathbf{a}_3^* are reciprocal basis vectors and \mathbf{a}_1 , \mathbf{a}_2 and \mathbf{a}_3 are the real space basis vector. n_1 , n_2 and n_3 are the atomic position. The relation between the real and the reciprocal basis vectors are $\mathbf{a}_i^* \cdot \mathbf{a}_j = 1$ for $i = j$, otherwise zero. Thus Eq. 14.1 can be rewritten as:

$$F_{u.c}(Q) = \sum_{r_j} f_j(Q) e^{i2\pi(hn_1 + kn_2 + ln_3)} \quad (14.2)$$

For the rock salt structure, the atomic positions are given in Table 14.1.

Table 14.1: Atomic position of rock salt structure crystal such as VC

V	(0, 0, 0)	($\frac{1}{2}$, $\frac{1}{2}$, 0)	($\frac{1}{2}$, 0, $\frac{1}{2}$)	(0, $\frac{1}{2}$, $\frac{1}{2}$)
C	($\frac{1}{2}$, $\frac{1}{2}$, $\frac{1}{2}$)	(0, 0, $\frac{1}{2}$)	(0, $\frac{1}{2}$, 0)	($\frac{1}{2}$, 0, 0)

Substitution of the atomic positions listed in Table 14.1 into Eq. 14.2 results in:

$$\begin{aligned} F_{VC} &= f_V e^{2\pi i(0)} + f_V e^{2\pi i(h/2+k/2)} + f_V e^{2\pi i(h/2+l/2)} + f_V e^{2\pi i(k/2+l/2)} + \\ &\quad f_C e^{2\pi i(h/2+k/2+l/2)} + f_C e^{2\pi i(h/2)} + f_C e^{2\pi i(k/2)} + f_C e^{2\pi i(l/2)} \\ &= f_V [1 + e^{\pi i(h+k)} + e^{\pi i(h+l)} + e^{\pi i(k+l)}] + \\ &\quad f_C [e^{\pi i(h+k+l)} + e^{\pi i(h)} + e^{\pi i(k)} + e^{\pi i(l)}] \end{aligned} \quad (14.3)$$

Using the identity of the complex exponential function $e^{ix} = \cos x + i\sin x$, equation 14.3 can be solved so that the unit cell scattering factor of VC are summarized:

$$F_{VC} = \left\{ \begin{array}{ll} 0 & , \text{ for mixed indices} \\ 4(f_V + f_C) & , \text{ if all h, k, l are even} \\ 4(f_V - f_C) & , \text{ if all h, k, l are odd} \end{array} \right\} \quad (14.4)$$

Bibliography

- [1] S. Veprek, *The search for novel, superhard materials*, J. Vac. Socl. Technol. A, Vol. 17, 1999, 2401-2420.
- [2] B. Ketterer, H. Vasilchina, S. Ulrich, M. Stueber, H. Leiste, C. Adelhelm, T. Kaiser and Th. Schimmel, *Magnetron sputtered thin film cathode materials for lithium batteries in the system LiCoO*, Springer Science, 2009, 405-409.
- [3] K. F. Chiu, H. C. Lin, K.M. Lin, and C. H. Tsai, *Modification of Sputter-Deposited Nanocrystalline $Li_xMn_{2-y}O_4$ Thin Film Cathodes by In Situ Substrate Bias and Postanneal*, Journal of The Electrochemical Society, Vol. 152(10), 2005, A2058-A2062 .
- [4] S. Kim, J. Jeon, H. W. Kim, J. G. Lee and C. Lee, *Influence of substrate temperature and oxygen/argon flow ratio on the electrical and optical properties of Ga-doped ZnO thin films prepared by rf magnetron sputtering*, Cryst. Res. Technol, Vol. 41, 2006, 1194-1197.
- [5] C. Ziebert, U. Albers, M. Stueber, S. Ulrich, *Constitution and Mechanical Properties of Nanocrystalline Reactive Magnetron Sputtered V-Al-C-N hard Coatings as a Function of the Carbon Content*, Plasma Processes and Polymers, Vol. 6, 2009, S560-S565.
- [6] O. Knotek, F. Loeffler, A. Schrey and B. Bosserhoff, *Physical vapor deposition of complex hard coatings on ceramic*, Surface and Coatings Technology, Vol. 61, 1993, 133-138.
- [7] www.ijs.si/ctp/ktrdeprevleke.A.html-l2/.
- [8] Avi Raveh et al., *Thermal stability of nanostructured superhard coatings: A review*, Surface & Coating Technology, Vol. 201, 2007, 6136-6142.
- [9] J. P. Reithmaier et al. (eds.), *Nanostructured Materials for Advanced Technological Applications*, Springer Science, NATO Science for Peace and Security, 2009, 257-267.
- [10] H. Holleck, *Advanced concepts in PVD hard coatings*, Vacuum, Vol. 41, 1990, 614-624.

Bibliography

- [11] F. Gao, *Theoretical Model of intrinsic hardness*, Physical Review B, Vol. 73, 2006, 132104/1-132104/4.
- [12] F. Gao, *Hardness of Covalent Crystals*, Physical Review Letters, Vol. 91, 2003, 015502/1-015502/4.
- [13] A. Simunek and J. Vackar, *Hardness of Covalent and Ionic Crystals*, Physical Review Letters, Vol. 96, 2006, 085501/1-085501/4.
- [14] J. C. Phillips, *Ionicity of the Chemical Bond in Crystals*, Reviews of Modern Physics, Vol. 42, 1970, 317-356.
- [15] G. Abadias, *Stress and preferred orientation in nitride based PVD coatings*, Surface & Coatings Technology, Vol. 202, 2008, 2223-2235.
- [16] J. Cahn, Y. Mishin and A. Suzuki, *Coupling grain boundary motion to shear deformation*, Acta Materialia, Vol. 54, 2006, 4953-4975.
- [17] P. Anderson www.ecr6.ohio-state.edu/mse/mse205/lectures.
- [18] P. H. Mayrhofer, C. Mitterer, L. Hultman, H. Clemens, *Microstructural design of hard coatings*, Progress in Materials Science, Vol. 51, 2006, 1032-114.
- [19] J. Musil, *Physical and Mechanical Properties of Hard Nanocomposite Films Prepared by Reactive Magnetron Sputtering*, Nanostructure Science and Technology, Springer Link, 2006, 407-463.
- [20] Z. Han, J. Tian, J. Lao and G. Li, *Effects of Thickness and Substrate on the Mechanical Properties of Hard Coatings*, JCT Research, Vol. 1, 2004, 337-341.
- [21] J. Marschall and F. Milstein, *Measurement and theory of the orientation dependence of Knoop microhardness in single-crystal mercuric iodide*, Journal of Materials Science, Vol. 29, 1994, 3295-3308.
- [22] Q. Yang, C. He, L. R. Zhao, J-P. Immarigeon, *Preferred orientation and hardness enhancement of TiN/CrN superlattice coatings deposited by reactive magnetic sputtering*, Scripta Materialia, Vol. 46, 2002, 293-297.
- [23] D. Brasen, *Evaluation of microstructures associated with hardness indentations in InP*, Journal of Materials Science, Vol. 13, 1978, 1776-1780.
- [24] B. P. O'Connor, E. R. Marsh and J. A. Couey, *On the effect of crystallographic orientation on ductile material removal in silicon*, Precision Engineering, Vol. 29, 2005, 124-132.

- [25] H. Wu, L. Wu, Q. He, P. Zhang and S. Du, *Effect of texture dispersion on the effective biaxial modulus of cubic polycrystalline films*, Applied Surface Science, Vol. 254, 2008, 5517-5523.
- [26] T. Irifune, A. Kurio, S. Sakamoto, T. Inoue and H. Sumiya, *Ultrahard polycrystalline diamond from graphite*, Nature, Vol. 421, 2003, 599-600.
- [27] S. Veprek and A. S. Argon, *Mechanical properties of superhard nanocomposites*, Surface and Coatings Technology, 146-147, 2001, 175-182.
- [28] T. H. Courtney, *Mechanical Behaviour of Materials*, McGraww Hill International, 2nded., 1999.
- [29] J. T. Busby et al., *The relationship between hardness and yield stress in irradiated austenitic and ferritic steels*, Journal of Nuclear Materials, Vol. 336, 2005, 267-278.
- [30] A. E. Tekkaya, *Annals of the CIRP*, Vol. 49, 2000, 205-208.
- [31] S. Veprek and M. G. J. Veprek-Heijman, *Concept for the Design of Superhard Nanocomposites with High Thermal Stability: Their Preparation, Properties, and Industrial Applications*, Nanostructure Science and Technology, Springer Link, 2006, 347-406.
- [32] S. Rупpi, A. Larson and A. Flink, *Nanoindentation hardness, texture and microstructure of α -Al₂O₃ and κ -Al₂O₃*, Thin Solid Films, Vol. 516, 2008, 5959-5966.
- [33] R. V. Stuart, Vacuum Technology, *Thin Films and Sputtering*, Academic Press, New York, 1983.
- [34] K. Wasa, M. Kitabatake and H. Adachi, *Thin Film Materials Technology*, William Andres publishing, New York, 2004.
- [35] S. Mahieu, P. Ghekiere, D. Depla and R. De Gryse, *Biaxial alignment in sputter deposited thin films*, Thin Solid Films, Vol. 515, 2006, 1229-1249.
- [36] X. Peng et al., *Plasma-based processes and thin film equipment for nano-scale device fabrication*, J. Mater. Sci., Vol. 46, 2011, 1-37.
- [37] D. Guettler, *An Investigation of Target Poisoning during Reactive Magnetron Sputtering*, a dissertation, Forschungszentrum Dresden-Rossendorf e.V., 2008.
- [38] K. Macak, P. Macak and U. Helmersson, *Monte Carlo simulations of the transport of sputtered particles*, Computer Physics Communications, Vol. 120, 1999, 238-254.
- [39] G. Braeuer, B. Szyszka, M. Vergohl and R. Bandorf, *Magnetron sputtering - Milestones of 30 years*, Vacuum, Vol. 84, 2010, 1354-1359.

- [40] S. Paldey and S. C. Deevi, *Single layer and multilayer wear resistant coatings of (Ti,Al)N: a review*, Material Science and Engineering, Vol. A342, 2003, 58-79.
- [41] Z. H. Barber, *The control of thin film deposition and recent developments in oxide film growth*, J. Mater. Chem, Vol. 16, 2006, 334-344.
- [42] B. Chapman, *Glow Discharge Processes*, John Wiley & Sons Inc, Canada, 1980.
- [43] A. A. Turkin, Y. T. Pei, K. P. Shaha, C. Q. Chen and D. I. Vainshtein, *On the evolution of film roughness during magnetron sputtering deposition*, Journal of Applied Physics, Vol. 108, 2010, 094330/1-094330/9.
- [44] R. Cremer and D. Neuschuetz, *A combinatorial approach to the optimization of metastable multicomponent hard coatings*, Surface and Coatings Technology, Vol. 146-147, 2001, 229-236.
- [45] X. D. Xiang, X. Sun, G. Briceno, Y. Lou, K. Wang, H. Chang, W. G. Wallace-Freedman, S. Chen, P. G. Schultz, *A Combinatorial Approach to Materials Discovery*, Science, Vol. 268, 1995, 1738-1740.
- [46] R. Cremer and D. Neuschuetz, *Optimization of (Ti,Al)N hard coatings by a combinatorial approach*, International Journal of Inorganic Materials, Vol. 3, 2001, 1181-1184.
- [47] www.webelements.com
- [48] T. B. Baumbach et al., *High Resolution X-Ray Scattering*, Springer Verlag, New York, USA, 2nd edition.
- [49] Jens Als-Nielsen and Des McMorrow, *Elements of Modern X-Ray Physics*, John Wiley & Sons Ltd, West Sussex, England, 2001.
- [50] B. E. Warren, *X-Ray Diffraction*, Dover Publications Inc, New York, USA, 1969.
- [51] C. Giacovazzo et al., *Fundamental of Crystallography*, Oxford University Press, England, 2002.
- [52] A. J. C. Wilson and E. Prince, *International Tables for X-Ray Crystallography*, Kluwer Academic Publisher, 1999.
- [53] B. D. Cullity, *Elements of X-Ray Diffraction*, Addison Wesley Publishing Company Inc, Massachusetts, USA, 1978.
- [54] G. Renaud, R. Lazzari and F. Leroy, *Probing surface and interface morphology with Grazing Incidence Small Angle X-Ray Scattering*, Surface Science Reports, Vol. 64, 2009, 250-380.

- [55] M. Birkholz, *Thin Film Analysis by X-ray Scattering*, Wiley-VCH verlag GmbH & Co, Weinheim, Germany, 2006.
- [56] I. C. Noyan, T. C. Huang and B. R. York, *Residual Stress/Strain Analysis in Thin Films by X-ray Diffraction*, Critical Reviews in Solid State and Material Sciences, Vol. 20(2), 1995, 125-177.
- [57] M. Newville, *Fundamental of XAFS*, Consortium for Advanced Radiation Sources, University of Chicago, 2008, Revision 1.8.
- [58] J. Wong, F. W. Lytle, R. P. Messmer and D. H. Maylotte, *K-edge absorption spectra of selected vanadium compounds*, Physical Review B, Vol. 30, 1984, 5596-5610.
- [59] E. D. Crozier, *A review of the current status of XAFS spectroscopy*, Nuclear Instruments and Methods in Physics Research B, Vol. 133, 1997, 134-144.
- [60] J.J. Rehr and R. C. Albers, *Theoretical approaches to x-ray absorption fine structure*, Reviews of Modern Physics, Vol. 72, 2000, 621-654.
- [61] D. C. Koningsberger, B. L. Mojet, G. E. van Dorssen and D. E. Ramaker, *XAFS spectroscopy; fundamental principles and data analysis*, Topics in Catalysis, Vol. 10, 2000, 143-155.
- [62] F. Troeger, D. Arvanitis, K. Baberschke, H. Michaelis, U. Grimm and E. Zschech, *Full correction of the self-absorption in soft-fluorescence extended x-ray absorption fine structure*, Physical Review B, Vol. 46, 1992, 3283-3289.
- [63] S. R. Bare, *XANES measurments and interpretation*, EXAFS Data Collection and Analysis Course, APS, 2005, 1-51.
- [64] V. A. Shuvaeva, K. Yanagi, K. Yagi, K. Sakaue and H. Terauchi, *Polarized XAFS study of the atomic displacements and hase transitions in KNbO₃*, J. Synchrotron Rad., Vol. 6, 1999, 367-369.
- [65] www.cars9.uchicago.edu/ifeffit
- [66] W. Jansen and M. Slaughter, *Elemental mapping of minerals by electron microprobe*, American Mineralogist, Vol. 67, 1982, 521-533.
- [67] A. S. Kurlov and A. I. Gusev, *Tungsten Carbides and WC Phase Diagram*, Inorganic Materials, Vol. 42, 2006, 121-127.
- [68] M. Wojdyr, *Fityk: a general-purpose peak fitting program*, J. Appl. Cryst., Vol. 43, 2010, 1126-1128.

- [69] O. P. Karpenko, J. C. Bilello and S. M. Yalisove, *Combined transmission electron microscopy and x-ray study of the microstructure and texture in sputtered Mo films*, J. Appl. Phys., Vol. 76(8), 1994, 4610-4617.
- [70] K. Chaek, *Research on the Drawing up of the Pole Figure for Orientation Analysis of Directional Si Steel Sheet*, J. Mater. Sci. Technol., Vol. 16, 2000, 159-160.
- [71] W. Kraus and G. Nolze, *POWDER CELL - a program for the representation and manipulation of crystal structures and calculation of the resulting X-ray powder patterns*, J. Appl. Cryst., Vol. 29, 1996, 301-303.
- [72] M. -H. Tuilier, M. -J. Pac, G. Covarel, C. Rousselot, and L. Khouchaf, *Structural investigation of thin films of $Ti_{1-x}Al_xN$ ternary nitrides using Ti K-edge X-ray absorption fine structure*, Surface & Coatings Technology, Vol. 201, 2007, 4536-4541.
- [73] M. -H. Tuilier, M. -J. Pac, M. Gîrleanu, G. Covarel, G. Arnold, P. Louis, C. Rousselot, and A. -M. Flank, *Electronic and atomic structures of $Ti_{1-x}Al_xN$ thin films related to their damage behavior* Journal of Applied Physics, Vol. 103, 2008, 083524/1-083524/1.
- [74] M. V Kartik and M. L. Culpepper, *Design of Hard Coated Hertzian Contacts for Precision Equipment*, submitted to the Precision Engineering.
- [75] M. Stueber, P. B. Barna, M. C. Simmonds, U. Albers, H. Leiste, C. Ziebert, H. Hollet, A. Kova, P. Hovsepian and I. Gee, *Constitution and microstructure of magnetron sputtered nanocomposite coatings in the system TiAlNC*, Thin Solid Films, Vol. 493, 2005, 104-112.
- [76] K.T. Jacob, S. Raj and L. Rannesh, *Vegard law a fundamental relation or an approximation*, International Journal of Material Research, Vol. 98, 2007, 776-779.
- [77] E. I. Isaev, S. I. Simak, I. A. Abridsov, R. Ahuja, Yu. Kh. Vekilov, M. I. Katsnelson, I. A. Lichtenstein and B. Johansson, *Phonon related properties of transition metals, their carbides, and nitrides: A first-principles study*, Journal of Applied Physics, Vol. 101, 2007, 123519/1-123519/18.
- [78] P. Soni, G. Pagare and S. P. Sanyal, *Structural, high pressure and elastic properties of transition metal monocarbides*, Journal of Physics and Chemistry of Solids, Vol. 72, 2011, 810-816.
- [79] J. C. Grossman, A. Mizel, M. Cote, M. L. Cohen and S. G. Louie, *Transition metals and their carbides and nitrides: Trends in electronic and structural properties*, Physical Review B, Vol. 60, 1999, 6343-6347.

- [80] M. Setoyama, M. Tanaka, N. Kitagawa and T. Nomura *Formation of cubic-AlN in TiN/AlN superlattice*, Surface and Coatings Technology, Vol. 86-87, 1996, 225-230.
- [81] N. Kietipaisalsophon, W. Bunjongpru, W. Techitdheera and J. Nukeaw, *Structure properties of cubic-AlN grown by reactive gas-timing rf magnetron sputtering*, Industrial Technology Conference, Vol. 2, 2002, 1365-1367.
- [82] A. Madan, I. W. Kim, S. C. Cheng, P. Yashar, V. P. Dravid and S. A. Barnett, *Stabilization of Cubic AlN in Epitaxial AlN/TiN Superlattices*, Physical Review Letters, Vol. 78, 1997, 1743-1746.
- [83] N. V. Lipatnikov, *Phase equilibria, phases and compounds in the V-C system*, Russian Chemical Reviews, Vol. 78, 2005, 697-723.
- [84] E. Kasper, A. Schuh, G. Bauer, B. Holls and H. Kibbel, *Test of Vegard's law in thin epitaxial SiGe layers*, J. Cryst. Growth, Vol. 157, 1995, 68-72.
- [85] A. R. Denton and N. W. Ashcroft, *Vegard's law*, Physical Review A, Vol. 43, 1991, 3161-3164.
- [86] J. E. Greene, J.-E. Sundgren, L. Hultman, I. Petrov, D. B. Bergstrom, *Development of preferred orientation in polycrystalline TiN layers grown by ultrahigh vacuum reactive magnetron sputtering*, Appl. Phys. Lett., Vol. 67, 1995, 2928-2930.
- [87] S. H. Tsai and J. G. Duh, *Microstructure and mechanical properties of CrAlN/SiNx nanostructure multilayered coatings*, Thin Solid Film, Vol. 518, 2009, 1480-1483.
- [88] S. Mahieu, P. Ghekierea, G. De Wintera, R. De Grysea, D. Deplaa, G. Van Tende-loob and O. I. Lebedevb, *Biaxially aligned titanium nitride thin films deposited by reactive unbalanced magnetron sputtering*, Surface & Coatings Technology, Vol. 200, 2006, 2764-2768.
- [89] www.allaboutcementedcarbide.com
- [90] www.virginiasemi.com/pdf/generalpropertiessi62002.pdf
- [91] M. A. Herman, W. Richter, H. Sitter, *Epitaxy Physical Principles and Technical Implementation*, Springer Verlag, Berlin, 2004, ISSN 0933-033X.
- [92] H. Holleck, *Metastable Coatings, Prediction of Composition and Structure*, Surface & Coatings Technology, Vol. 36, 1988, 151-159.
- [93] M. D. Abad, D. Cáceres, Y. S. Pogozhev, D. V. Shtansky, J. C. Sánchez-López1, *Bonding Structure and Mechanical Properties of Ti-B-C Coatings*, Plasma Process. Polym., Vol. 6, 2009, S107-S112.

Bibliography

- [94] H. C. Barshilia, B. Deepthi and K. S. Rajam, *Deposition and characterization of TiAlN/Si₃N₄ superhard nanocomposite coatings prepared by reactive direct current unbalanced magnetron sputtering*, Vacuum, Vol. 81, 2006, 479-488.
- [95] J. Musil and H. Hruby, *Superhard nanocomposite Ti_{1-x}Al_xN films prepared by magnetron sputtering*, Thin Solid Films, Vol. 365, 2000, 104-109.

List of Symbols

a, b, c	lattice parameters
a_{hkl}	lattice parameter calculated from d_{hkl}
$\langle a \rangle$	average lattice parameter
a_0	relaxed lattice parameter
a_{ij}^{MS}	matrix transformation of the measured direction and substrate coordinate system
(a_1, a_2, a_3)	basis vector in real space
(a_1^*, a_2^*, a_3^*)	reciprocal basis vector
A	atomic mass
A_{VC}, A_{AlN}	area of VC and AlN target
$(1-c)$	concentration of the covalent material
$\cos(\beta)$	projection of the flux on the substrate
C	the ratio of R_{AlN} and R_{VC}
d	grain size
d_{hkl}	lattice spacing
$(d_{hkl} + \delta d_{hkl})$	strained lattice spacing
E	Young's Modulus
E_B	binding energy of core level electron
E_{hkl}	Young's Modulus in $[hkl]$ direction
f, f'	dispersion correction
f_j	corrected atomic scattering factor
f_j^0	atomic scattering factor without correction
f, if''	real and imaginary part of dispersion correction
$F(P_S, P_T)$	the incident flux onto a given position at substrate from a point source
$F(P_S)$	the total incident flux onto a given substrate position P_S
$F_{crystal}$	structure factor of a crystal
FWHM	full width at half maximum
(h,k,l)	Miller indices
$G(P_T)$	Gaussian function of the target erosion area
I_f	fluorescence intensity
I_0	incident intensity
k	wave number

List of Symbols

k_B	Boltzmann constant
k_y	strengthening constant
m_{hkl}	multiplicity of the (hkl) reflection
N_j	number of neighbor atoms j
P_S	position at substrate
P_T	position at target
P	pressure
q	difference between Q and Q_{hkl}
Q	momentum transfer
Q_{hkl}	momentum transfer at the Bragg's reflection
r	distance between P_S and P_T
r_1, r_2	radius of the colliding particles
R_{VC}, R_{AlN}	deposition rate of VC and AlN
R	ideal gas constant
R_j	inter-atomic distance between the absorbing atom and neighbor atom j
$R_{V-(V,Al)}$	average atomic distance of V-V and V-Al
$R_{V-(C,N)}$	average atomic distance of V-C and V-N
t	thickness
T	temperature
V	volume unit cell
Y_{VC}	sputtering yield of VC
Y_{AlN}	sputtering yield of AlN
Z	atomic number
α, β, γ	angles between main crystal axis of a unit cell
$\chi(k)$	simplified EXAFS equation
δ_{ij}	Kronecker delta
δ_j	phase shift
$\Delta\mu$	background correction in XAFS spectra
ΔG	the lowest total Gibbs free energy
ΔG_i	Gibbs free energy of phase i
ϵ	interaction energy
ϵ_{ij}^M	component of the strain tensor in the measured direction
$\epsilon_{\phi, \Psi}$	strain at ϕ, Ψ direction
\hbar	reduced Planck constant
λ	wavelength
λ_{mfp}	mean free path
$\lambda(k)$	mean free path of the photoelectron
μ	absorption coefficient
ϕ	azimuth angle in a polar coordinate

List of Symbols

Ψ	tilting angle in a polar coordinate
Ψ_{hkl}	average orientation of (hkl) texture
ρ	sample density
σ_{hkl}	distribution of (hkl) texture
$\sigma_{ }$	lateral residual stress
σ_{ij}	components of the stress tensor
σ_j	a measure for atomic distance distribution
σ_y	yield stress
σ_0	required stress for an individual dislocation motion
θ	angle between the incident beam and the scattering plane
2θ	angle between the incident beam and the diffracted beam
ν	Poisson ratio

Acknowledgment

I learn that taking a chance is the first step to improve my self. The person I should give a credit for giving me a possibility to do PhD in the field that I (almost) did not know anything about is Prof. T. Baumbach.

The second person I thankful for is Dr. Baerbel Krause for her patient, scientific advice and for always challenging me to find answers of difficult questions. I would like to thank also to Dr. Stüber, Dr. Ulrich, Dr. C. Ziebert at Institut für Angewandte Materialien - Angewandte Werkstoffphysik (IAM-AWP) at Karlsruhe Institut für Technologie (KIT), Germany. Thanks for the samples as well for the scientific discussion.

I thank as well to the beamline scientists at ANKA: Dr. S. Mangold, Dr. S. Doyle and Dr. Buth for all support during the experiments. Additional thanks is given to Dr. S. Mangold for analyzing the XAFS data. To all colleagues which help during experiments: Dr. Riotte, Dr. Fohtung, B. Miljevic. M. Kaufholz, S. Kotapati, etc, I appreciate all helps that you guys gave.

I would like also to thank to Dr. Peter Zaumseil. at Leibniz Institut für Innovative Micro Electron, Frankfurt Oder, both for the scientific discussion and help with the laboratory source as well as for being a warm host during my stay there.

For all members of Prof. Powell's group at Institute for Inorganic Chemistry, I would like to thanks for the fruitful seminar time we had.

Curriculum Vitae

Mariyam S. D. Darma

Born in Bandung, 4th August 1977

Indonesian nationality

Phone: +49(0)17625867083

Email: msdd040877@yahoo.com

Education

- **2007 - 2012** : Doctoral promotion at Karlsruhe Institute of Technology (KIT), Karlsruhe, Germany.
Organization : Institute for Synchrotron Radiation, Karlsruhe - Germany
Thesis title : Microstructure analysis of V-Al-C-N hard coating by X-Ray Diffraction (XRD) and X-Ray Absorption Fine Structure (XAFS) Spectroscopy.
PhD defense : April 19, 2012, *Summa Cum Laude*
- **2005 - 2007** : Master Program: Materials for Energy Storage and Conversions.
University : Université Paul Sabatier, Toulouse - France.
Master thesis : Preparation and Characterization of Ga doped ZnO polycrystalline thin films by rf sputtering process.
- **1996 - 2001** : Bachelor Degree in Chemistry University : Bandung Institute of Technology - Indonesia Bachelor thesis: Biodegradation of oxidized polyethylene by activated sludge

List of Publication

- Baerbel Krause, Susan Darma, Marthe Kaufholz, Hans-Hellmuth Graefe, Sven Ulrich, Miguel Mantilla, Ralf Weigell, Steffen Rembold, and Tilo Baumbach, *Modular deposition chamber for in situ X-ray experiments during RF and DC magnetron sputtering*, J. Synchrotron Rad, Vol. 19, 2012, 216-222.

- B. Krause, S. Darma, M. Kaufholz, S. Mangold, S. Doyle, S. Ulrich, H. Leiste, M. Stüber, and T. Baumbach, *Composition-dependent structure of polycrystalline magnetron-sputtered V-Al-C-N hard coatings studied by XRD, XPS, XANES, and EXAFS*, submitted to Journal of Applied Physics, December 2012.

Participation in Conference and Meetings

- **Oral Presentation** at European Materials Research Society Spring Meeting, May 28 2012, Strassbourg, Title: *Combined XRD and XAFS study of the crystalline structure of V-C-Al-N*. **S. Darma** , B. Krause , S. Mangold, S. Doyle, S. Ulrich , M. Stüber, T. Baumbach.
- **Poster Presentation** at DPG-Frühjahrstagung der Sektion Kondensierte Materie (SKM), Berlin, 25-30 March 2012. Title : *Influence of the deposition geometry on the microstructure of sputter-deposited V-Al-C-N coatings*. **S. Darma**, B. Krause, S. Doyle, S. Mangold, S. Ulrich, M. Stueber, T. Baumbach.
- **Oral presentation** at Size and Strain Conference, October 17 - 20, 2011, Pres[^]qu'ile de Giens, France. Title : *In situ-X-Ray study of Vanadium Carbide*. B.Krause, **S. Darma**, T.Baumbach, M. Stueber, S. Ulrich.
- **Poster presentation** at Size and Strain Conference, October 17 - 20, 2011, Pres[^]qu'ile de Giens, France. Title : *Microstructure of Thin (V,Al)(C,N) Hard Coating*. **S. Darma**, B.Krause, S.Doyle, M.Stueber, S.Ulrich, T.Baumbach.
- **Poster presentation** at the 12th European Powder Diffraction Conference, August 27 - 30, 2010. Title : *Microstructure of Thin (V,Al)(C,N) Hard Coating*. **S. Darma**, B. Krause, S. Doyle, M. Stueber, S. Ulrich, T. Baumbach.
- **Poster presentation** at 2nd International Symposium on Transparent Conducting Oxides, Heraklion, Crete, Greece, 22 - 26 October 2008. Title : *Growth and characterization of Ga-doped ZnO thin films using non reactive rf magnetron sputtering*. A. Barnabé, M.S.Dewi - Darma, M.Lalanne, I. Pasquet, L. Presmanes, and Ph. Tailhades.
- **Oral presentation and Proceeding** at First International Workshop on Nanotechnology and Applications IWNA 2007, 15-17 November 2007, Vung Tau City, Vietnam. Title : *Influence of the rf-sputtering deposition condition on the structural and physical properties of p and n-type TCO thin films*. A. Barnabé, **M. S. D. Darma**, E. Mugnier, I. Pasquet, L. Presmanes, C. Bonningue and Ph. Tailhades.

Last updated: December 10, 2012